Technische Universität München
Fakultät für Chemie

Iridium Oxide as Catalyst in Water Electrolysis: Identification of Novel Surface Structures via Machine Learning

JAKOB CHRISTIAN TIMMERMANN

DISSERTATION

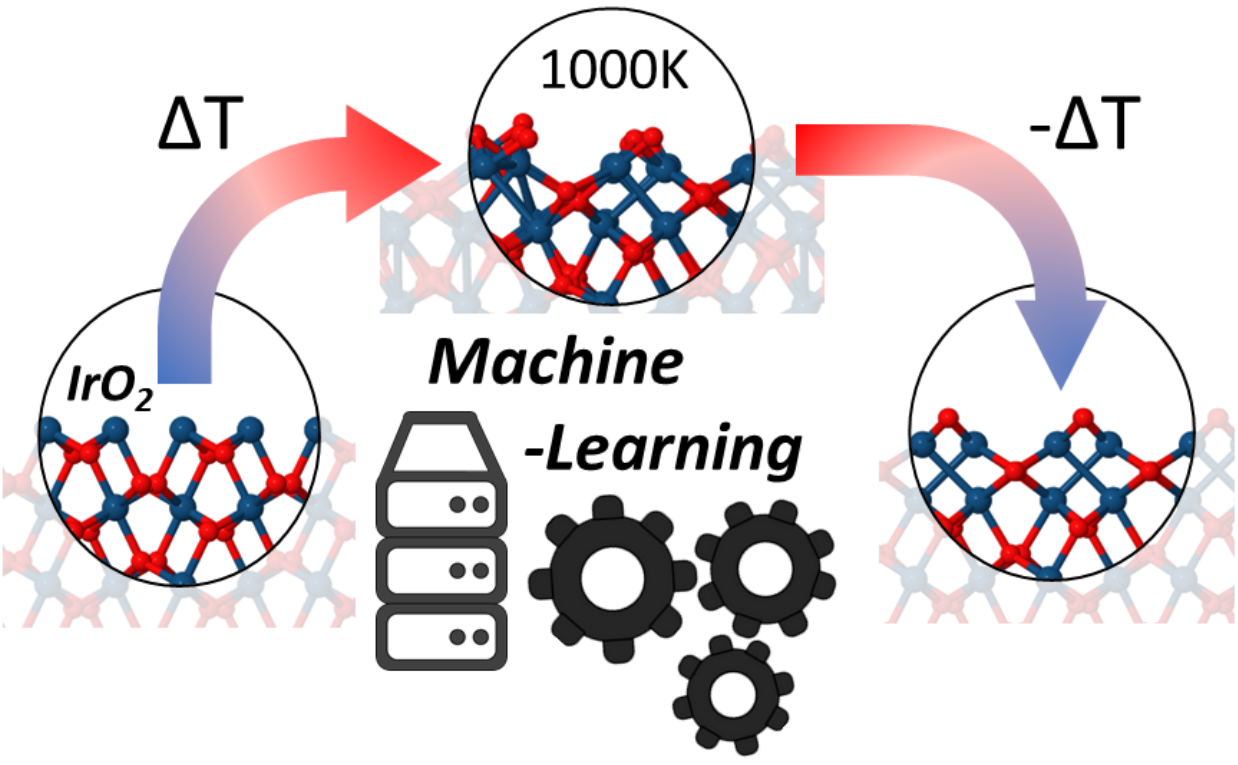

Technische Universität München
Fakultät für Chemie

Iridium Oxide as Catalyst in Water Electrolysis: Identification of Novel Surface Structures via Machine Learning

Jakob Christian Timmermann

Vollständiger Abdruck der von der Fakultät für Chemie der Technischen Universität München zur Erlangung des akademischen Grades eines

Doktors der Naturwissenschaften (Dr. rer. nat.)

genehmigten Dissertation.

Vorsitzender: Prof. Dr. Hubert A. Gasteiger

Prüfer der Dissertation:

1. Prof. Dr. Karsten Reuter
2. Prof. Dr. Harald Oberhofer

Die Dissertation wurde am 6.12.2021 bei der Technischen Universität München eingereicht und durch die Fakultät für Chemie am 24.02.2022 angenommen.

Mein tiefer Dank gilt auch diesmal

den tollsten Schwestern,

den besten Eltern,

allen meinen Freunden,

der einmaligen Jadekatze und

stets dem Retrogott.

"Keine Atempause, Geschichte wird gemacht,
es geht voran."

Preface

This dissertation is publication-based, thus its scientific content is published in two related, but independent articles, [1] and [2], which both have undergone the scientific peer-review process in international scientific journals and are appended to this work. The first four chapters mainly serve as an introduction to the thematic motivation, relevant literature, and the applied Machine Learning Method. Summaries of both article are then provided in chapter 5. The main part of the presented work has been carried out at the Chair of Theoretical Chemistry of the Technical University of Munich (TUM) between April 2017 and September 2020 and has been completed between October 2020 and November 2021 at the Fritz Haber Institute of the Max Planck Society in Berlin, both times under the supervision of Prof. Dr. Karsten Reuter. Major parts of my PhD was founded by the Deutsche Bundestiftung Umwelt.

München, November, 2021

Abstract

Green hydrogen is an integral part of the future, renewable energy landscape as clean fuel and bulk chemical of important chemical processes. Hydrogen production in flexible electrolysis cells is, furthermore, perfectly suited to buffer the fluctuating electricity supply of wind and solar parks. Proton Exchange Membrane (PEM) and Alkaline Electrolysis (AEL) are to date the most promising options to challenge the currently cheaper and thus predominant hydrogen production via steam reforming of fossil gas. Although the PEM cell offers some essential advantages compared to the Alkaline Electrolyzer, the roll-out at industrial scale is a long time coming. This is primarily due to the harsh operating conditions and the hence very limited number of potential catalysts. In the acidic and corrosive operating environment iridium oxide (IrO_2) (and to smaller extend ruthenium oxide (RuO_2)) are the only promising catalysts for the oxygen evolution reaction (OER) at the anode. The low iridium abundance, however, demands a significant reduction of the metal loading in order to make the PEM technology sustainable and profitable. Although efforts to optimize IrO_2/RuO_2 catalysts have led to a variety of studies the catalyst performance has only improved gradual. A more stringent and systematic optimization requires a more precise understanding of the catalyst surface and related atomic processes. While computer simulations based on Density Functional Theory (DFT) or classical force fields have enabled investigations at the atomic level for decades, both methods are limited for complementary reasons: DFT methods provide a highly accurate and complete description, are, however, limited to small(er) systems due to their enormous computational costs. The much faster force fields can cope with large systems, yet, only provide an incomplete description as they are restricted to a fixed atomic connectivity. Here emerging Machine Learning (ML) methods might close the gap, as they enable a fast, accurate, and complete description of larger systems including catalytic surfaces.

The identification of the (still unknown) IrO_2/RuO_2 surface morphologies via a specifically developed global optimization method is the central topic of this thesis. This method applies a combination of ML and DFT to determine the global energy minimum structure of various IrO_2/RuO_2 surfaces via an iterative simulated annealing (SA) protocol. Already the first, still manually executed version of this iterative training protocol revealed multiple hitherto unknown surface morphologies (so-called complexions), that are characterized by a reordering of the terminating atom layers. The energetically lowest and thus decisive complexion was then experimentally validated in cooperation with the chair of Prof. Ulrike Diebold at the University of Vienna. Motivated by this success the training protocol has been optimized and quantified to obtain a fully automated ML enhanced global optimization method that provides a gateway to structural optimization of crystal surfaces.

Zusammenfassung

Grüner Wasserstoff stellt einen integralen Bestandteil der Energiewende dar und kann als Treibstoff sowie Grundchemikalie wichtiger chemischer Prozesse verwendet werden. Die Herstellung in flexibel einsetzbaren Wasserelektrolysezellen kann außerdem die fluktuierende Stromerzeugung von Wind und Solarparks optimal puffern. Proton Exchange Membrane (PEM) und Alkalische Elektrolyse (AEL) sind dabei die derzeit vielversprechendsten Optionen, um die momentan vorherrschende da billigere Wasserstoffherstellung via Dampfreformierung aus Erdgas abzulösen. Obwohl die PEM- gegenüber der AEL-Zelle einige wesentliche Vorteile aufweist, lässt eine industrielle Umsetzung noch auf sich warten. Dieses ist primär auf die extremen Bedingungen innerhalb der PEM-Zelle und der daher sehr begrenzten Auswahl an stabilen Katalysatormaterialien zurückzuführen. So kommt im sauren und korrosiven Milieu der Anodenseite nur Iridiumoxid (IrO_2) (und mit deutlichen Abstrichen Rutheniumoxid (RuO_2)) als Katalysator für die dort stattfindende Sauerstoffentwicklungsreaktion (engl.: Oxygen Evolution Reaction, daher OER) in Frage. Aufgrund des geringen Iridiumvorkommens muss jedoch die Metallbeladung stark reduziert werden, um die PEM Technologie nachhaltig und kommerziell rentabel zu machen. Zwar haben Bestrebungen zur Optimierung von IrO_2 Katalysatoren in den letzten Jahren zu einer Vielzahl an Studien geführt, was jedoch nur mit graduellen Fortschritten hinsichtlich der Katalysatorleistung verbunden ist. Ein stringenteres und systematischeres Vorgehen setzt ein genaueres Verständnis der Katalysatoroberfläche und der sich darauf abspielenden atomaren Prozesse voraus. Computersimulationen - basierend auf Dichtefunktionaltheorie (DFT) oder klassischen Kraftfeldern - ermöglichen zwar schon seit Jahrzehnten Untersuchungen auf atomarer Ebene, sind jedoch aus komplementären Gründen limitiert: DFT Methoden bieten eine sehr genaue und komplette Beschreibung, sind allerdings aufgrund der enormen Rechenkosten auf kleine(re) Systeme beschränkt. Größere Systeme stellen für die mit deutlich weniger Rechenkosten verbunden Kraftfelder zwar kein Problem dar, werden von diesen aber nur unvollständig beschreiben, da Kraftfelder eine fixe atomare Konnektivität erfordern. Diese Lücke könnte von den neu aufkommenden Methoden des maschinellen Lernens (ML) geschlossen werden, da diese eine schnelle, akkurate und vollständige Beschreibung größerer Systeme, wie etwa Katalysatoroberflächen, zulassen.

Die Identifizierung der (noch unbekannten) IrO_2/RuO_2 Oberflächenmorphologien mit Hilfe einer eigens entwickelten globalen Optimierungsmethode ist das zentrale Thema meiner Dissertation. In dieser Methode kommt eine Kombination aus ML und DFT zur Anwendung, um so das globale Energieminimum diverser IrO_2/RuO_2 Oberflächen über ein iteratives Simulated Annealing (SA) Protokoll zu bestimmen. Schon mit der ersten noch manuell ausgeführten Version dieses iterativen Trainingsprotokolls konnten mehrere bis dato unbekannte Oberflächenmorphologien identifiziert werden, nämlich sogenannte complexions, die durch Umordnung der terminierenden Atomschichten erhalten werden. Die energetisch niedrigste und damit ausschlaggebende complexion konnte in Kooperation mit dem Lehrstuhl von Prof. Ulrike Diebold an der Universität Wien experimentell validiert werden. Motiviert durch diesen Erfolg wurde das Trainingsprotokoll im Folgenden optimiert und quantifiziert, um so eine vollautomatische ML-basierte Methode zur globalen Optimierung zu erhalten, die auf beliebige Kristalloberflächen angewendet werden kann.

List of Abbreviations

AEL	Alkaline Electrolysis
AEM	Anion Exchange Membrane
DFT	Density Functional Theory
FF	force fields
GAP	Gaussian Approximation Potential
GO	global optimization
GPR	Gaussian Process Regression
HER	hydrogen evolution reaction
MEA	Membrane Electrode Assembly
ML	Machine Learning
OER	oxygen evolution reaction
PEM	Proton Exchange Membrane
PES	potential energy surface
RIs	reaction intermediates
SA	simulated annealing
SFE	Gibbs surface free energy
SOAP	Smooth Overlap of Atomic Positions

Contents

1 Introduction

One of the major challenges of the present decade, if not of the century is the decarbonization of the energy production, i.e. substituting oil- and coal-fired power station by hydropower plants, wind and solar parks. With broad implementation of environmental friendly energy sources anticipated worldwide, new challenges are arising from an inevitably changing energy mix (exemplary data from the Federal Statistical Office of Germany[3]). One of the main challenges is the highly fluctuating electricity supply of renewable energy sources due to weather conditions compared to the steady operation of classic power plants.[4–6] Especially the fluctuations of wind and solar parks are in large parts opposite to the actual energy demand as energy produced during the day/summer has to be stored and made available during the night/winter. Accordingly the deployment of alternative energy sources crucially depends on the efficient conversion and/or storage of surplus electricity. [4, 7, 8]

A combination of numerous technologies will be necessary to achieve complete and efficient energy storage, ranging from short-term storage in regular or redox-flow batteries, medium-term storage/consumption via conversion to warm water or hydrogen fuel and long-term pumped hydroelectric energy storage.[8, 9] The conversion of surplus electricity to hydrogen fuel via the electrochemical decomposition of liquid water comes with the advantage, that H_2 constitutes an energy carrier *and* a commodity chemical that is highly demanded in many chemical processes including the Haber–Bosch process and methanol synthesis.[10]

There are currently two different water electrolysis technologies that are industrial relevant: Alkaline Electrolysis (AEL) and Proton Exchange Membrane (PEM) cells.[4–6, 11–13] The major advantages of PEM over AEL cells are the higher current density, allowing to fully respond to sudden spikes in the intermittent power supply and higher operating pressure which results in an overall higher power efficiency. In order to meet all requirements for an application on an industrial scale though, additional performance improvements and cost reduction of the PEM cell are mandatory.

In an electrolyzer the water decomposition is spatially divided into the hydrogen evolution reaction (HER) at the cathode and the oxygen evolution reaction (OER) at the anode. The OER is generally considered the performance bottleneck in both, PEM and alkaline electrolyzers, due to the substantial anodic overpotential and the resulting efficiency drop.[14–16] In the acidic and corrosive operating environment of PEM cells iridium oxide (IrO_2) and to smaller extend ruthenium oxide (RuO_2) are currently the only promising catalysts balancing stability and activity. [17–23] Although only a minor contributor to the overall stack costs, the low abundance of iridium[24] makes a reduction of the metal loading inevitable in order to achieve commercial viability.[6, 25–27] It is thus not surprising that in recent years the effort in optimizing IrO_2/RuO_2 based catalysts led to a variety of studies including experimental[28–38], theoretical[39–44] as well as combined studies[45] ranging from basic research to compound simulations.

Even though there is gradual progress in catalyst performance due to intensive screening of preparation and operating conditions, detailed information about the atomic structure is still scarce as experimental in-operando characterization of catalysts is challenging and limited in

resolution.[23, 46] Computational methods, like Density Functional Theory (DFT) provide insight on an atomic scale and might help to develop a better understanding of the catalyst surface morphology and to eventually determine possible reaction pathways.

The identification of the (still unknown) IrO_2/RuO_2 surface morphologies via computational investigations is the main topic of this thesis. The sheer number of calculations necessary to determine a meaningful surface structure though, calls for simulation techniques multiple orders of magnitudes faster than regular DFT calculations.

For decades only parameterized methods have fit this speed criterion, such as classical interatomic potentials/force fields (FFs). The drawback is the onerous parameterization process and generally unclear transferability of such classical potentials or force fields. Thus unsurprisingly, there exists a force field for IrO_2[47] combining the variable QEq charge model[48] and an interatomic Morse potential[49]. The intrinsically fixed atomic connectivity though, prevents any bond breaking and forming and thus renders identification of unknown surface morphologies via classic interatomic potentials impossible.

Fortunately, in recent years a completely new class of reactive, interatomic potentials emerged, applying Machine Learning (ML) techniques i.a. Neural Networks[50, 51] or Gaussian Approximation Potential (GAP)[52–54] that enable simulation with almost DFT-accuracy at drastically reduced computational costs. Opposed to FFs where the total energy of an unknown system is calculated via a predefined functional form, ML potentials approximate the total energy based on the structural similarity to available training data. Accordingly ML potentials do not apply a fixed atomic connectivity and are hence suitable to identify novel structures accessible only via structural changes. With plenty of (recently published) success stories[55–66] it has to be kept in mind that these techniques are still in their infancy and plenty of dedication, iterating and testing is yet necessary to unleash the full range and power of ML applications. In this respect, my thesis might be considered a small contribution to the steady optimization and exploration of ML methods.

The centerpiece of this thesis is a combined ML/DFT global optimization method based on the GAP approach, in which novel, low-energy IrO_2/RuO_2 surface structures are identified via an iterative simulated annealing (SA) protocol. A first fully supervised prototype of this method was successfully applied to investigate numerous IrO_2 surfaces, determining multiple new surface morphologies, so called complexions, that are obtained via reordering of the terminating atom layers.[1] Subsequent DFT calculations confirm that these complexions significantly lower the surface free energy of a given termination and change the relative energetics at low oxygen chemical potential. In cooperation with the Institute of Applied Physics at the Technical University Vienna the one dominant, most stable IrO_2 complexion has been experimentally characterized and confirmed.

Motivated by this success the initial, supervised training protocol has been rigorously optimized, quantified and automatized, up to the point where we present a fully automated ML enhanced global optimization method that provides a gateway to structural optimization of any kind of (multicomponent) crystal surfaces.[2] Together with my fellow colleague Yonghyuk Lee the final protocol was applied to IrO_2 as well as RuO_2, identifying more unknown complexions. As the preparation conditions typically have a large influence at least on the initial catalyst surface structure and morphology, these findings are of utmost importance for OER catalysts manufactured at low oxygen potentials and might pave the way for a more precise understanding of and instructions for future catalyst design.

In both cases the results have been published as peer-reviewed articles. This publication-based

dissertation accordingly serves as an introduction of the underlying concepts necessary for an in detail understanding of this research and hopefully provides guidance for further improvements and application. In chapter 2 we will introduce the general concept and the major industrial implementations of the water electrolysis and further discuss the current challenges in OER catalyst optimization on a macro- and microscopic scale. In the following chapter 3 we illustrate the most common (and simplest) atomic models for rutile IrO_2/RuO_2 crystals, derive how to classify surface structures via the surface free energy and discuss the computational challenges of local and global structure optimization, necessary to identify novel low-energy surface morphologies. A detailed discussion of the Gaussian Approximation Potential framework can then be found in chapter 4, including a tutorial of the underlying theory, available atomic representations and our approach towards the hyperparameter selection.

2 Industrial water electrolysis for hydrogen production

In electrolysis an electric direct current is applied at two electrodes in a conductive liquid (the electrolyte) to drive a chemical reaction that is otherwise energetically and/or kinetically prohibited. The voltage source generates an electron-deficit at the anode and an electron-surplus at the cathode and induces two partial reactions. The full reaction itself is hence formally and spatially separated into a pair of reduction and oxidation half reactions that consume respectively produce electrons. In case of the water electrolysis the full reaction is separated into the hydrogen evolution reaction (HER) at the cathode and the oxygen evolution reaction (OER) at the anode.

$$2\ H_2O_{(l)} \xrightarrow{I} 2\ H_{2(g)} + O_{2(g)} \qquad \text{(Water-Electrolysis)} \tag{2.1}$$

$$2\ H_3O^+_{(l)} \xrightarrow{+2e^-} H_{2(g)} + 2\ H_2O_{(l)} \qquad \text{(Reduction Cathode HER)} \tag{2.2}$$

$$4\ OH^-_{(l)} \xrightarrow{-4e^-} 2\ H_2O_{(l)} + O_{2(g)} \qquad \text{(Oxidation Anode OER)} \tag{2.3}$$

As apparent from eq. (2.1) both products are gaseous, and thus leave the reaction equilibrium and shift the reaction towards the right. However, since water is by far the more stable state for both species, the overall reaction is not favored with a Standard Gibbs energies of formation of $\Delta_f G^\circ_{H_2O} = 228.71$ kJ/mol which is equivalent to a standard potential of $E^\circ_{H_2O} = -1.23$ V.[67] At potentials more negative than $E^\circ_{H_2O}$ the water splitting reaction is solely kinetically controlled.

The first and fundamental criterion to meet in any electrolysis cell is to guarantee a closed electric current between the two electrodes, such that the reaction educts (in this case the hydronium and/or hydroxyl ions) are pulled toward the respective oppositely charged electrode. To this end the electrolyte connecting the two electrodes has to provide a sufficient concentration of charge carriers, i.e. positively and/or negatively charged ions. Pure water at pH=7, however, is characterized by a very small ion concentration as a result of its marginal self-ionization and hence in all industrial water electrolysis cells the conductivity of the electrolyte is improved drastically by in-/decreasing the pH value and adding additional charge carriers. Still, in practice voltages significantly larger than $E^0_{H_2O}$ have to be applied due to a variety of factors including activation energy, ionic and molecular diffusion barriers and cell component resistances as well as formation of O_2/H_2 gas bubbles at the electrode surface, temporarily preventing further electron transfers. This surplus voltage necessary to actually initiate water splitting is referred to as overpotential η. Accordingly η is a cell-specific conglomeration of very different phenomena that all together determine the performance and efficiency of an electrolyzer. Performance improvement regarding the water electrolysis thus implies either a reduction of the overpotential (reducing the operational costs) or a reduction of catalyst loading (reducing the investment costs) without a significant drop in production.

Considering the distinctive character of the individual contributions to the overpotential a team effort of multiple scientific disciplines is required to achieve holistic improvements. The ohmic

loss due to resistance and gas bubbles is an intrinsically mechanical challenge and thus has to be left for fellow cell design experts to overcome.[68][1]

Consequently, we refer the interested reader to the manifold of work within technical electrochemistry and materials science that addresses diffusion processes and cell conductivity, testing and updating available diaphragms, membranes and electrolyte composition.[4, 6, 16]

The largest part of the overpotential is usually assigned to the activation overpotential which again is ambiguous, as it is a combination of two different types of activation barriers, the energy required to transfer an electron to/from the electrode from/to the reactant (electron transfer overpotential) and the energy required to generate adequate precursors prior to the actual electron transfer (reaction overpotential).

Nonetheless the general way to lower any kind of reaction barriers remains the same, viz the addition of an appropriate catalyst; it is thus in no way surprising that from the earliest implementation of electrolysis cells catalysts for both, reduction and oxidation have been thoroughly investigated and optimized constantly.

These (heterogeneous) catalysts should follow the Sabatier principle, i.e. stabilize reaction intermediates (RIs) without hindering the consecutive reaction(s) to and desorption of the product and the catalytic performance can then be approximated based on (selected) adsorption energies in so-called volcano plots (see below).[69–71] While volcano plots provide a good estimate regarding thermodynamic metrics, kinetic aspects are neglected although they might become crucial for highly active catalysts and/or under working conditions (i.e. above the onset potential $> E^0_{H_2O} + \eta$) and thus have to be accounted for.[72, 73] Alongside that, further requirements for electrocatalysts are a fairly good conductivity, enabling the electrons transfer to the reactants, and a sufficiently high stability in the (generally harsh) environment of a water electrolysis cell.

Alkaline Electrolysis (AEL) and the Proton Exchange Membrane (PEM) electrolyzer are at present the only two technologies that can claim industrial application. While the former is considered more mature with application in the MW range[4] the latter does provide interesting advantages though to date application is limited to small units within the KW range.[25] A detailed illustration of the schematic composition of a Proton Exchange Membrane electrolyzer together with a hypothetical reaction mechanism of the OER can be found in Fig. 2.1. As discussed in more detail below, materials in both electrolysis cells are not only exposed to a high applied potential but also to highly acidic respectively alkaline conditions, which especially for the PEM cell raises the bare for material requirements w.r.t. corrosion.

In PEM cells the standard catalyst for the HER (see eq. 2.2) at the cathode are platinum nanoparticles dispersed on carbon black (Pt/C) with a typical platinum loading between 0.035[26] and 0.1 mg cm^{-2}[4] while in AEL cells cheaper materials like Raney Nickel are the successfully used catalysts for decades now.[74, 75] At industrial applied operational current densities (>0.5 A cm^{-2}) the two-electron HER process is characterized by reasonably fast kinetics[15] and the overpotential of the water electrolysis is typically dominated by the overpotential of the four-electron OER (see eq. 2.3). Therefore and since the Pt loading can be potentially reduced to 0.05 mg cm^{-2} without significant performance losses, the HER itself and its catalysts are currently not in the spotlight of scientific attention and huge progress, e.g. regarding the replacement of Pt/C catalysts are neither considered a burning issue nor likely to happen in the near future.[6] Thus the specifics of the HER shall not be discussed in full detail in this introductory chapter. The

[1] Obviously the surface morphology of the catalyst has implications on the gas diffusion and - as will be seen - also on catalytic activity etc. but guaranteeing sufficient diffusion is still mainly a mechanical challenge.

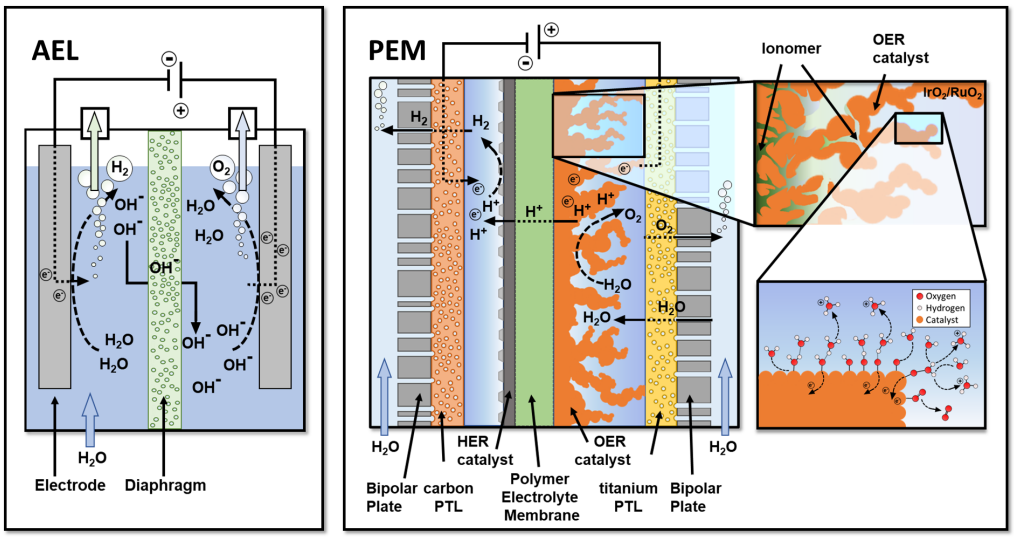

Fig. 2.1: *(Left): Schematic setup of a alkaline electrolysis cell. Cathode and anode are separated by a porous diaphragm that allows hydroxyl diffusion and the electrolyte, a KOH solution. (Right): Schematic composition of a Proton Exchange Membrane (PEM) electrolysis cell. The cathodic side and anodic side both consist of a bipolar plate, a Porous Transport Layer (PTL) which also functions as current collector and the respective HER/OER catalysts in a zero gap setup, separated via a Polymer Electrolyte Membrane permeable only for protons. In industrial electrolyzers a Nafion™ membrane and platinum nanoparticles on carbon black (Pt/C) as HER catalyst are used while several Ir and/or Ru materials have been applied and tested as OER catalysts (see section 2.4). A polymer solution (ionomer) is added to promote the proton transport through the catalytic layer towards the membrane while the electron is transferred to the current collector at intersections of catalyst and PTL (top right inlet). In the bottom right inlet of the PEM panel, the peroxo reaction pathway (cf. eq. (2.8)-(2.11)), as one potential mechanism of the four electron oxidation of the OER at the catalytic surface is depicted.*

interested reader is instead referred to the pertinent literature.[17, 76–78]

Similar to the cathodic chamber the conditions at the anode in PEM and AEL cells are obviously different and thus dictate completely distinct catalytic materials. However, both types of anodes have in common, that they are usually designed as porous as possible in the respective environment, to maximize the reactive surface and enable fast circulation of solvent, reactants, and gaseous products. In addition, high cell current densities, high temperatures and high operation pressures are usually considered desirable to increase the cell efficiency for both, PEM and AEL. Reasonably high current densities are required to assure the necessary power throughput while high temperature commonly drives the endothermic reaction towards its products. Finally, high operation pressure reduces the need for additional posterior H_2 gas compression (required for efficient storages as well as direct consumption, e.g. mobile sector) even though a post-production compression might be more cost effective than high pressure operation at reduced catalytic efficiency[79].

The common features and differences together with the resulting advantages and challenges of AEL and PEM setups along Fig. 2.1 are discussed in the following two sections. Recent developments considering OER catalyst improvements and proposed reaction pathways for relevant catalysts are recapped in the final section of this chapter. An even more detailed and technical discussion considering the overall competitiveness of alkaline and PEM systems taking into account more technical details like durability and cell lifetime, investment and annual maintenance costs as well as stack size and capacity can be found in recent reviews and studies.[4, 11]

2.1 Alkaline electrolyzer

In AEL cells hydroxyl ions are the charge carriers and industrial electrolyzers are usually operated with a cheap 20-30 % KOH solution[12] that is easily replaceable and chemically stable w.r.t. to impurities and chemical decomposition while ensuring a high hydroxyl/charge carrier concentration (pH ~12).

As illustrated in the left panel of Fig. 2.1 cathode and anode are spatially divided by a thin solution film and a porous diaphragm that allows hydroxyl diffusion, i.e. free circulation of charge carriers. The alternative zero-gap setup where the respective catalyst is directly dispersed on the diaphragm is found less often.[11, 80] Since the alkaline solution is much less corrosive than the acidic environment of a PEM electrolyzer, a wider range of materials beyond expensive platinum-group metal(-oxides) can be used as HER/OER catalysts such as the much more abundant Ni, Co and Fe metals.[4, 81, 82]

Historically AEL cells have been operated at low current densities of 200-400 mA cm^{-2}[4], as the overpotential necessary to maintain higher current densities (>400 mA cm^{-1}) results in uneconomical cell voltage (e.g. 1.98 V at 1000 mA cm^{-2}[83]).

This narrative is questioned though as selected studies applying advanced catalysts and/or setups report reasonable voltages at high currents for novel cell setups (e.g. 1.85 V[84] at 1000 mA cm^{-2}) within reach to regular PEM cells.

The lower maximum current density can be partially ascribed to the liquid electrolyte and a corresponding bulky cell design as the ohmic loss due to hydroxyl diffusion (linearly) increases with the electrode distance, in the first approximation. On the same note, the liquid electrolyte is also the limiting factor regarding operating pressure and temperature. While in general operation at high pressure and high temperature is possible, the former increases O_2 and H_2 diffusion

through the aqueous electrolyte and diaphragm. Gas impurities especially at the anode can exceed the technical safety limits of 2 vol.%. For example, increasing the operation pressure from 1 to 10 bar results in an increase of the anodic H_2 concentration from 0.3 to 2.0 vol.%.[85]

The intrinsically fluctuating nature of wind and solar energy supply poses another specific challenge for regular alkaline electrolyzers: even though the widely used Ni-based catalysts are very stable at a cell potential $>E^{\circ}_{H_2O}$ they show notable dissolution below this potential prohibiting an operation at reduced power densities, a major disadvantage in the application as an energy buffer for renewable sources.[13] Furthermore and probably even more critical, an increased gas diffusion and thus impurity at part-load conditions has been observed.[85]

While short periods without electrode polarizations can be tolerated when gas impurity is still low, longer periods with low to no power density, i.e. also loss of polarization will eventually lead to a hazardous increase of H_2 concentration at the anode. This imminent risk can be tremendously decreased by a spatial separation of the electrolyte cycles of anode and cathode. This however requires occasional mixing as the separation leads to an in-/decrease of hydroxyl ions at the cathode respectively anode. To completely avoid any complications an external energy storage device can be implemented upstream to balance out any excessive fluctuation of the supply. In both cases additional components have to be implemented into the setup which consequently increases complexity and investment costs.

Nonetheless, the conceptually less complex and to date more economical setup seems to give (regular) alkaline cells a competitive edge above PEM cells for now and makes them the main commercial application especially for steady state conditions.

2.2 Proton Exchange Membrane electrolyzer

The PEM electrolyzer is in many aspects complementary to the alkaline cell, obviously starting with the highly acidic environment (pH ~2) with substantial implications for the overall stack composition and applied materials.[4] Alongside this eponymous pH contrast, the stack concept differs from the AEL as we usually find a zero-gap setup with coated catalyst membrane where the electrocatalyst is dispersed on the separating polymer electrolyte membrane. The combination of membrane and electrode is referred to as Membrane Electrode Assembly (MEA).[2]

As illustrated in the top right inlet of the PEM panel in Fig. 2.1 the electrocatalyst in this setup is connected to the membrane to reduce any ohmic loss due to diffusion processes of protons towards the membrane. In PEM cells the much smaller and mobile protons (in comparison to the hydroxyl anions) serve as charge carriers and in turn enable the application of a solid polymer membrane as electrolyte, permeable only for protons.

A variety of membrane materials has been tested in recent years where perfluorosulfonic acid polymers such as Nafion™ or Selemion™ are currently the preferred choice. Overall this cell component benefits from a considerable knowledge transfer from PEM fuel cells considering standard Nafion™ membranes, even though additional optimization to account for electrolyzer specifics (e.g. higher pressure compared to fuel cells) is necessary.[6] Furthermore, there are still ongoing efforts to substitute these perfluoro materials by hydrocarbon-based polymers as these are in general cheaper and more stable at higher operating temperatures (above > 100 °C).[86]

An ionomer (i.e. polymer solution) is added during the catalyst synthesis (usually ~10%) which mixes with the catalytic material to increase the proton transfer ability through the catalytic layer

[2] This is the origin for the second equally applied extension of the acronym PEM: **P**olymer **E**lectrolyte **M**embrane.

towards the membrane as well as the dimensional stability of this layer.[87, 88]

To enable electron transfer towards the respective electrodes the catalyst is attached to the Porous Transport Layer (PTL) which serves as a current collector and regulates solvent and gas diffusion. Finally, surrounding separator plates (aka bipolar plates), separating multiple PEM cells within each stack, are required. In a PEM cell several independent transport and diffusion processes have to be considered and balanced to maximize the overall performance. The overall reaction flow can be sketched as follows:

Water molecules fed at the anode side first flow through the bipolar plate via relatively broad channels and diffuse through the PTL to reach the MEA and eventually the catalytic layer, where they are decomposed into (solvated) protons, electrons and molecular oxygen via the OER. The protons leave the electrocatalyst and diffuse through the ionomer towards and across the membrane to the cathode side on the other side of the MEA chamber while the electrons travel through the conductive catalytic layer to the PTL and via the circuit to the cathode where they combine with the protons at the Pt/C surface to form molecular hydrogen in the HER. The oxygen and hydrogen gas have to exit the respective catalyst layers, diffuse back through the PTL and the separator plate and leave the cell together with the process water.[4]

The implementation of a solid electrolyte as spatial separator of cathode and anode in a zero gap setup comes with three major advantages over the alkaline cell:

Solid electrolyte membranes are generally characterized by much lower gas crossover rates compared to an aqueous solution. Consequently, PEM electrolyzers can operate at considerably higher pressure thus making a post-production hydrogen compression obsolete. While obviously H_2 and O_2 diffusion are still to be avoided, this can be regulated by the membrane thickness yielding high purity hydrogen without additional effort like gas-recombiners. Trinke *et al.* estimate that at atmospheric pressure a Nafion™ membrane with a thickness exceeding 100 µm would be sufficient to guarantee an anionic H_2 concentration smaller than 2.0 vol.%.[85]

Furthermore, no severe stability issues are reported for PEM catalysts for low (non-zero) power densities. Accordingly, PEM cells can cover (almost) the full power density range and thus little to no additional effort has to be made to account for intermittent energy supply. Higher cell pressure and slim electrolyte membranes are moreover allowing for a more compact stack stack design reducing the operational costs.

Yet the probably most compelling advantage over the alkaline electrolyzer are the higher current densities at which a PEM cell can be operated. In general, the maximum current densities of an electrolyzer are limited by the ohmic loss, which in turn depends in first approximation on electrode distance and ion conductivity. In addition to the smaller electrode distance (50-250 µm, respectively 400-550 µm for zero-gap PEM and AEL)[11, 85, 89, 90], the molar ionic conductivity at 25°C and infinite dilution of hydronium ions (350 S $cm^2 mol^{-1}$) is significantly larger than that of hydoxide ions (198 S cm^2 mol^{-1}).[91] As a result higher, maximum current densities are accessible for PEM cells, achieving values above 2 A cm^{-2}.[4, 6]

With all the advantages outlined above the combination of high applied voltage and acidic solution comes with one main drawback: only a restricted number of materials is actually stable in this environment, in particularly at the anode where these materials additionally have to be inert to corrosion given an increased O_2 concentration. This does not only affect the selection of possible OER and HER catalysts but extends to membrane, bipolar plate and porous transport layer as well.

Since extraordinarily expensive Ir-coated Ti materials have to be used as PTL and separator plate, these make up for $40 - 50$ % of the stack costs[4, 92]. Despite the high potential regarding

cost reduction, e.g. via substitution[92, 93], research and development considering PTL and bipolar plate optimization are still just at the beginning.[6]

Considering the OER catalyst candidates, several studies confirm rutile structured oxides as best material choice. Here, Ru-based catalysts are more reactive yet prone to dissolution while Ir-based materials are less reactive however much more stable and ergo the preferred choice in state-of-the-art PEM electrolyzers.[19–21, 28] Commercial OER catalysts are currently characterized by an iridium loading between 1 and 3 mg_{Ir} cm^{-2}.[6, 16]

In general, PEM cells are characterized by a slightly shorter life time in comparison to AEL cells which is at least partly related to the aforementioned OER catalyst degregation.[4, 94] Nonetheless, reduced performance can also be attributed to a couple of additional factors, including an ongoing replacement of protons within the membrane by competing cations which results in a decreased conductivity[95], or ohmic losses by the oxidation of surfacial Ti present in the PTL and separator plates resulting in a non-conductive TiO_2 coating.[96] Particularly challenging in the scientific analysis of test stacks is the extrapolation of short-term durability and stability experiments (hours to days) towards the long-term operation of industrial PEM cells (years to decades) and hence conclusive insights are rare at this end.[23, 94, 97]

In summary, the PEM setup provides some important advantages over AEL cells yet the high costs due to the compulsorily application of noble metals and high loadings at both electrodes to date prevent an industrial-scale implementation. On the other side it is sure to say that alkaline cells can be considered a mature and well established technology with some major drawbacks regarding its adaptability in renewable energy power plants.

2.3 Anion Exchange Membrane electrolyzer

A third alternative approach that receives more and more attention in recent years is aiming to combine the approaches of PEM and alkaline cell concepts by applying an Anion Exchange Membrane (AEM), permeable for OH^- instead of H^+ (potentially) combining the advantages of both techniques. As a highlight and similar to the alkaline cell AEM catalysts are in general not limited to the expensive platinum group metals. In addition, AEM cells still achieve the same hydrogen purity and compact stack size[98–100] as well as high current densities (e.g. 2 A cm^{-1} at 1.82 V)[101] in short-term experiments as the PEM electrolyzer. However, with this technology still in its infancy, the main obstacle is the low durability of the alkaline membrane and to the best of my knowledge no industrial long-term operation has been reported yet.[102] In the present thesis only this brief outline can be provided and the interested reader is referred to the relevant literature.[6, 102, 103]

2.4 The Oxygen Evolution Reaction in Acidic Solution

In the very first PEM electrolyzers, reported in the early 70s at General Electrics pure metallic iridium (and/or ruthenium) was used as OER catalyst (see, e.g. [104]).However, considering that already in the late 60s Trasetti *et al.* concluded that pre-generated (thermal) Ru/Ir oxides are substantially more stable[105] than metallic Ru/Ir, most recent studies agree on IrO_2 (respectively doped/mixed IrO_2 material) as the preferred OER catalyst.[19, 23, 39]

Since then decades of research and knowledge transfer from PEM fuel cells have borne fruits and PEM electrolyzers are competitive compared to AEL in small installations (kilowatt range). In

modern PEM cells HER and OER catalysts account for (only) ~15% of the overall costs (including stack and supporting components).[4, 106] Yet, due to the scarcity of iridium, the reduction of the Ir loading in PEM electrolyzers by (at least) an order of magnitude (from 1-3 mg_{Ir} cm^{-2} to ~0.4 mg_{Ir} cm^{-2}) is an absolute constraint for a large-scale industrial application.[6, 25–27]

Even though there is unabated interest and good reason to try to completely substitute Ir by more abundant and less precious elements such as cobalt based materials[107–110], no competitive catalyst has been reported so far.[111]

At present, Ir (and to smaller extent Ru) materials remain frontrunners and the only material class seriously considered for industrial applications. For an overview and comparison of activity and stability at standardized conditions of commercially available Ir-based catalyst see [112].

It thus comes as no surprise that a broad variety of studies on how to increase current density performance and long-term stability and/or decrease Ir loading has been published, similar to the optimization of HER and HRR (hydrogen reduction reaction) catalysts. In contrast to the HER (in acidic environment)[3], where only one reaction intermediate is formed, the OER as a four-electron process comprises at least three RIs (compare right inlet of Fig. 2.1).

Accordingly HER catalysts can be optimized by considering the adsorption energy of the sole intermediate which makes it a one-dimensional problem (in first approximation). On the contrary, within the OER catalyst optimization adsorption energies of multiple RIs have to be balanced as discussed in more detail below. On top of that, potential degradation processes have to be identified and mitigated to increase the catalyst durability.

While the scientific community unanimously agrees on the demand for optimization, the general concepts on how to achieve this vary significantly. From my (rather theoretically biased) point of view these efforts can be divided into two different approaches which might be labeled instant vs. long-term, practical vs. fundamental or even optimization vs. understanding.

The first approach focuses on directly increasing the catalyst (and overall cell) performance here and now, i.e. on instant, practical optimization based on macroscopic properties of industry-relevant cells and empirical experience.

The second ansatz emphasizes insights to and conclusions from microscopic structure and processes (be it via experimental observations or computational simulations), i.e. the fundamental understanding of the OER which in the long-term facilitates catalysts optimization.

Obviously, the present thesis leans more towards the latter and a detailed discussion and perspective are presented in section 2.4.2. Yet in the next section, the first, practical approach shall be addressed by a small compilation of recent studies providing some insight into the meticulous experimental effort to improve the OER catalyst and thus PEM electrolyzer performance.

2.4.1 Catalyst performance optimization

If we assume the catalytic surface structure to be homogeneous and independent of size and shape of the catalyst, one apparent way to improve the activity of any catalyst is to increase the ratio of surface area to catalyst loading. Even though a homogeneous and independent catalytic surface is a harsh approximation, controlling the shape and size for IrO_2 (nano-)structures is a natural route of optimization. Accordingly, synthesis routes for multiple 1-D, 2-D, and 3-D nanomaterials including small "regular" nanoparticles,[28, 29] ultra-thin nanoneedles,[114] laminar superstructures,[115] mesoporous thin films,[116] and nanotube arrays[117, 118] can be found in recent literature.

[3] Note here that in alkaline solution the HER becomes a two-step reaction process, as the protons have to be abstracted from water molecules and HER catalyst optimization gets less straightforward than for acidic HER[6, 113]

However, long-term durability tests of these materials are either missing or are referenced to in-house benchmark catalysts, limiting their transferability and informative value.

An alternative strategy is the addition of less expensive materials in order to dilute the Ir loading[4] while maintaining the overall activity and dimensional stability. Obviously this extends the creative leeway yet also the synthesis and system complexity.

One commonly used catalytic material is the Umicore catalyst (a mixed IrO_2-TiO_2) with a reduced iridium loading of 66%.[30] Another IrO_2-TiO_2 catalyst was reported by Oakton *et al.* with an even further reduced Ir loading of 60% that shows slightly lower overpotential in comparison to the Umicore reference.[31]

Besides titanium oxide as additional material, improved activity and decreased Ir-loading has been, e.g. reported for different IrM alloys with M = Ni, Co, Fe,[32] lanthanides, and iridium double perovskites Ba_2MIrO_6 with M = Y, La, Ce, Pr, Nd or Tb.[34] It has to be noted that in short-term stability experiments (up to 11 h) only selected lanthanides and perovskite candidates showed similar durability as common IrO_2 nanoparticle.

Another concept that relies on secondary materials, too, are core-shell catalysts where a catalytically active layer is dispersed on a (cheaper) core material.[35] In an early study on IrNi@IrO_x Nong *et al.* were aiming - rather unusually - for activity improvement instead of load reduction.[36] A 50% load reduction (at constant activity and slightly improved stability) was then reported by Trackett *et al.* for IrO_2@FeN/Co core-shell particles.[37] Following a different approach Kim *et al.* presented a new method to increasing the activity by dealloying thin Ir_xOs_y films and nanoparticles generating an IrO_2 shell on a metallic Ir core.[119]

In a "hybrid" kind-of approach Tariq *et al.* disperse whole IrO_2 nanoparticles on even larger MoO_3 particles (generating macroscopic core-shell particles) and conclude a synergistic effect of core and shell material due to enhanced electrochemical performance and stability.[120] In a recent study, Pham *et al.* introduced an enhanced core-shell catalyst with a TiO_2 core and a thin, crystalline IrO_2 shell. In a full-cell test mimicking an industrial stack the candidate yields superior performance over a Umicore benchmark catalyst with catalytic loadings as low as 0.4 $mg_{Ir}cm^{-2}$.[38]

Last but not least, continuous efforts are made to combine the outstanding activity of ruthenium (oxide) with the increased stability of iridium (oxide) based materials,[121, 122] as *in situ* XPS investigation suggests a positive effect of mixing the precious metals on the overall stability. The enhanced stability is assigned to a suppressed formation of (unstable) hydrous ruthenium oxide $Ru(OH)_4$ by vicinal Ir atoms.[123] Exemplary, Xu *et al.* recently showed that small $Ir_xRu_yO_z$ nanoparticles supported on a CoNC metal organic framework exhibit high activity as well as improved stability and assign the increased stability to a higher degree of catalyst immobilization at the MOF surfaces, preventing catalyst agglomeration and, consequently, loss of active surface.[121]

This compilation should be sufficient to illustrate the variety of optimization approaches and the associated challenge of keeping track of all new findings let alone drawing universal conclusions from them. Moreover, it is apparent, that stability and activity of these Ir-based catalysts are not solely defined by their chemical composition. Rather and opposite to the approximation outlined at the beginning of this section we **do** observe a substantial dependence of activity and stability w.r.t. growing condition, particle size and shape - ergo on the surface morphology.

[4] It shall be noted here that load reduction reported here is referenced to "pure" IrO_2 catalyst, as given in the respective publications. This however does not indicate a strictly and well defined reference system as a detailed review of the different growing methods of these reference catalysts is way beyond the scope of this thesis, making consistent, cross-publication comparison difficult.

Most studies conclude that OER activity and stability are strongly correlated, i.e. implying that catalytically active materials/sites are also more prone to dissolution as both processes, reaction and dissolution might share common RIs.[20, 21, 30] However, recent investigations of several single-crystalline RuO_2 surfaces by Roy *et al.* suggest that these two phenomena might be decoupled for certain surface morphologies.[124] While breaking the activity-stability relation would actually be good news, it also reveals that unclear surface morphologies make interpretation and comparison of experimental findings exceptionally difficult.

As a matter of fact, it seems like implementing a standardized experimental setup for activity and stability measurements is very difficult which in turn renders a stringent catalyst classification and identification of correlations complicated to impossible.[23, 125, 126] The catalyst stability, for example, is characterized via chronopotentiometry or -amperometry, i.e. monitoring the potential at a constant current (and vice versa) for a given time period in almost all of the above studies. Yet these experiments substantially vary in duration (1-300 h), applied constant current (1-2000 $mA\,cm^{-2}$) respectively constant potential (1.0-2.0 V), and overall setup.

Evidently a guideline to compare, classify and optimize OER catalysts would be highly beneficial. While macroscopic descriptors like the S-Number (number of produced oxygen molecules per number of dissolved iridium atoms)[127] or the Ir^{3+} and OH concentration at the catalytic surface[128] might provide some guidance considering catalyst performance/stability, no straightforward conclusion on why this or that descriptor varies for different systems can be drawn.

In order to provide more conclusive observations a clear idea of the microscopic surfaces properties and (reaction) processes is required.[23, 39, 128, 129] Unsurprisingly, there always have been attempts to account for microscopic properties as an increasing number of studies incorporate insights from computational methods to support proposed hypotheses.

Regarding the overview of studies above, Trackett *et al.* as well as Xu *et al.*, for example, underpin their findings via estimating the OER activity based on *ab initio* binding energies of proposed reaction intermediates on simplified models, simulating Ni_4N/Fe_4N support respectively mixed $IrRuO_4$ surfaces. However, it is questionable whether the extremely complex material presented in these studies can be satisfactorily described by simple surface models.

In the next section we will discuss the systematic approaches to gain access to the atomic structure and provide a relation between the OER activity and microscopic properties.

2.4.2 Mechanism and catalyst structure on an atomic scale

Although catalyst improvements purely based on macroscopic properties are possible, identification of microscopic processes and morphology could be pivotal for a faster and more sustainable optimization regarding the OER activity. Microscopic insights, however, demand resolution at an atomic scale, be it via experimental or computational investigations. That said, there is an undeniable discrepancy in length and time-scale experimental and computational resolution - yet the challenge to close this gap has been and is incessantly addressed by both communities.

From an experimental point of view, improving experimental techniques continuously extend our knowledge of the atomic structure and processes of actual catalytic materials.[46]

From a theoretical point of view, the increase in computation power and advances regarding theoretical methods have not spared electrocatalysis, enabling larger and more realistic surface simulations.[23, 39]

Since the adsorption energies and consequently the OER activity are crucially depending on the proposed reactions intermediates **and** the surface morphology meaningful conclusions

should only be drawn if experimentally investigated surface and the atomistic slab model are akin. As computational methods are still limited to small, periodic slab cells arguably only a strict elimination of material complexity in experiment provides a stringent relation between macroscopic and microscopic properties. In simple periodic slab models the surface morphology is determined by its crystal orientation given by the Miller index (hkl) with $h, k, l \in [0, 1, 2, ...]$ and the surface termination σ, specifying the terminating atomic layer. For a detailed discussion in particular of surface morphologies of RuO_2 and IrO_2 see chapter 3.1.

One promising approach is the experimental investigation of so-called single-crystalline model systems that are characterized by a uniform and homogeneous surface structure and can hence be directly compared to the respective periodic slab model. Needless to say, single-crystalline model electrodes are complicated to synthesize and, due to the high metal loading (small surface/bulk ratio), certainly not the final industrial choice.

One of the earliest and still most common experimental approaches towards the OER mechanism is the Tafel analysis, an approximation to the Butler-Volmer equation in case of negligible backwards reaction ($\eta > 0.2$) that has been applied as early as 1956 by Bockris *et al.*.[130] In a Tafel plot the (over-)potential measured for a catalytic surface is then displayed as a function of the logarithm of the current density. A kink in the Tafel slope indicates either a change of the rate determining step (rds) of the respective reaction or a change of the terminating atom layer of the active surface. The latter is a sometimes overlooked yet not uncommon phenomenon.[40, 42, 45, 131] Since the adsorption energies and consequently the overpotential are crucially depending on the morphology of the active surface, conclusions from a Tafel analysis should only be drawn if the experimentally investigated catalyst is characterized by a single-crystalline surface.

In their pioneering study Bockris *et al.* suggested multiple reaction mechanisms, including a predecessor of the electrochemical oxide path discussed next, without committing to one in particular.[130]

Thirty years later Castelli *et al.* in their study of a single-crystalline RuO_2 (110) surface revisited the electrochemical oxide path proposing four elementary steps *R*.[132]

$$M + H_2O \longrightarrow M{-}OH^* + H^+ + e^- \tag{2.4}$$

$$M{-}OH^* \longrightarrow M{-}OH \tag{2.5}$$

$$M{-}OH \longrightarrow M{-}O + H^+ + e^- \tag{2.6}$$

$$2M{-}O \longrightarrow M + O_2 \tag{2.7}$$

Note here, that we follow the original notation of Castelli *et al.* where M represents a metal site and $M{-}OH^*$ indicates an intermediate surface species that then undergoes a chemical rearrangement (eq. 2.5) before further oxidation. From the observed kink they conclude that this chemical rearrangement is the rds for potentials below 1.52 V while the initial water adsorption (eq. 2.4) is the rds above 1.52 V. Today, however, the electrochemical oxide path, especially the final recombination (eq. 2.7) is considered unlikely.

A purely computational approach towards the OER mechanism, based on *ab initio* thermodynamics was introduced by Rossmeisl *et al.*.[14, 15] Here the overpotential of an (in advance proposed) reaction mechanism at a specific surface is approximated via the (potential-dependent) Gibbs free energy difference of the OER $\Delta G_{\mathrm{OER}}(U)$, which in turn is given by the Gibbs free energy difference of the cascading reactions $\Delta G_{\mathrm{OER}}(U) = \sum_R \Delta G_R(U)$ After calculating the required energies based on appropriate computational surface models, the overpotential can be extracted

from the elementary reaction with maximum $\Delta_R G(\mathrm{U})$ (see reference [14] for the detailed method). Since in this ansatz only reaction steps depending on the cell voltage, i.e. including an electron transfer are considered, any other elementary steps (e.g. chemical rearrangement) are neglected.

In their original work Rossmeisl *et al.* propose an alternative peroxo path for (110) surfaces of RuO_2, IrO_2 and TiO_2.

$$^* + H_2O \longrightarrow HO^* + H^+ + e^- \tag{2.8}$$

$$HO^* \longrightarrow O^* + H^+ + e^- \tag{2.9}$$

$$O^* + H_2O \longrightarrow HOO^* + H^+ + e^- \tag{2.10}$$

$$HOO^* \longrightarrow ^* + O_2 + H^+ + e^- \tag{2.11}$$

In this updated notation * represents an catalytically active surface site. This reaction mechanism is illustrated in the bottom right inlet of the PEM panel of Fig. (2.1). It is important to note that since the overall reaction depends on several different adsorption/binding energies (viz. M–OH, M–O and M–OOH) so does the overpotential.

In addition, Rossmeisl *et al.* conclude that the catalytically active site is a coordinately unsaturated (CUS) metal site located at the surface. Since then CUS metal atoms have been confirmed to be the active sites for OER at RuO_2 surfaces by several studies.[124, 133–135] However, CUS atoms of different morphologies are usually characterized by very different electronic structure and coordination environment which renders direct classification based solely on density of CUS atoms misleading.[135]

Despite obvious approximations (see below) this purely thermodynamic approach culminated in considerably accurate relations between activity and selected adsorption energies displayed in so-called volcano plots and has received widespread recognition.[15, 136, 137] In case of OER catalysts, the volcano plot is typically relating the OER activity to the difference of oxygen and hydroxy binding energies $\Delta G_{\mathrm{O}} - \Delta G_{\mathrm{OH}}$.

All in all, Tafel analysis and *ab initio* thermodynamics have been undoubtedly and exceedingly successful in many regards. However, both methods have an identical and potentially crucial drawback: they are heavily biased w.r.t. the hypothesized mechanism and active surface.[23, 138] Already Bockris realized that two different mechanisms might result in similar or even identical Tafel slopes. Moreover, any reaction pathway that is based solely on *ab initio* adsorption energies of (arbitrarily) selected reaction intermediates at (arbitrary) surfaces is in limbo and might lead to false conclusions without supplementary experimental validation.

In addition to that, both have their own specific shortcomings as the Tafel analysis does not provide microscopic insights nor the actual thermodynamics of the RIs, while within the *ab initio* thermodynamics picture any kinetic contribution is ignored.[39, 42, 44] Furthermore, it is painfully difficult to include explicit solvation effects in atomic-scale computational simulations due to the large statistics that are entailed.

While in principle the latter can be partially bypassed by implicit solvation models, the local character of solvation effects on the OER reaction/catalyst, e.g. hydrogen bonding pose seemingly insurmountable obstacles regarding a detailed description.[139] Only a handful of studies including explicit aqueous solvation, usually in form of static water layers, can be found in literature[36, 41, 131] indicating the potential influence of explicit solvation on surface morphology and adsorption energy.[23] Even harder to account for are ionic effects at the electrode-electrolyte interface, the so-called electric double layer.[140, 141]

Kinetic barriers have been investigated in an *ab initio* study of Ping *et al.* comparing multiple reaction pathways on the IrO_2 (110) surface in implicit solvation revealing that the thermodynamically favored pathway might be characterized by high-energy transition states, i.e. unfavored kinetics.[42]

One way to incorporate kinetics *and* thermodynamics into a full reaction path has been introduced by Exner *et al.*. In a set of studies they combine Tafel measurements of single-crystalline electrodes and *ab initio* calculations to determine the free energy diagram, i.e. reaction pathway of the chlorine evolution reaction (CER) over RuO_2 (100), the HER over Pt (111) as well as the OER over RuO_2 (110) and IrO_2.[45, 138, 142] Slope and kinks of the Tafel plot are used to extract the energy of transition states while the binding energies of RIs are extracted from electronic structure calculations. During their studies they observe several changes of the active surface, implying a distinct potential dependence of the surface morphology.

Kuo *et al.* also observe different active surfaces for varying potentials in their study combining cyclic voltammetry (CV) and electronic structure calculations of single-crystalline IrO_2 (110) and RuO_2 surfaces.[72, 140] [5]

Regarding the starting surface for electronic structure calculations, the general conception was and still is to consider primarily IrO_2 (110) or RuO_2 slab models as these are reckoned to exhibit the lowest surface energy.[23, 41, 42, 45, 131, 132, 138, 143] Yet how misleading an exclusive focus on (110) surfaces might be has been stressed in recent years by several studies indicating a pronounced dependence of mechanism, activity (and stability) on the surface orientation.[23, 39, 43]

Roy *et al.*, for example, report surface-specific activity and stability for (110), (001), (101) and RuO_2 (111) surfaces and rationalize this with varying density and coordination environment of the Ru CUS sites.[124] On the same note, Stoerzinger *et al.* emphasize the influence of the distinct electronic structure of the CUS sites on the OER activity of (100), (101), (110) and RuO_2 (111) and IrO_2 surfaces and find (100) and (101) notably more active than (110) for both materials.[40, 134] And just recently Rao *et al.* report an orientation-specific change of the rds observed at the RuO_2 (101) surface opposed to (100) and (110) surfaces.[133, 135] This change is rationalized by a descending binding energy for M−OO, with (101) < (100) < (110), caused by deviations in the electronic structure of the respective RuCUS sites. Finally, in a comprehensive study on a set of more than 70 IrO_2 surfaces of varying orientation and termination Opalka *et al.* concluded that the (somewhat neglected) (111) orientation is most stable at OER operating conditions.[43]

This excerpt illustrates the ongoing, vivid exchange and discussion on the mechanism, activity and stability of specific IrO_2 and RuO_2 catalysts.[6]

[5] They further observe a pH-dependency of the OER activity which they attribute to the interfacial water arrangement at different pH values. This change in activity is rationalized by a change in OER mechanism, in particular the acid-base transition of M−OOH formation, where in acidic environment (eq. 2.10) is favored, while at pH>10 the competing alkaline pathway $M{-}O + OH^- \longrightarrow M{-}OOH + e^-$ is favored (implying a reaction rate that is first-order in OH^-).

[6] In addition to the discussion outlined above, one of the most heated debates shall not be ignored here, which ensued around whether or not lattice oxygen is involved in the OER.[39, 125, 134] While there is consensus that lattice oxygen is contributing to the oxygen production in alkaline cells if (Ir-based) perovskites are used as catalysts,[125, 144] isotope labeling experiments of rutile IrO_2/RuO_2 catalysts in acidic environment paint an ambiguous picture. Stoerzinger *et al.*, for example, conclude that for crystalline, mono-oriented RuO_2 surfaces the lattice oxygen evolution reaction (LOER) is negligible,[134] which is in stark contrast to previous findings for IrO_2[145] and RuO_2[146] electrodes of not further specified morphology. This debate seems to proceed to the next stage as a recent study by Schweinar *et al.* report an exchange of oxygen atoms between water and oxide lattice on a surface

Only recently this discussion has been extended to surface morphologies revealing a dormant optimization potential. A thorough understanding of the relation between surface morphology and activity (as well as stability) is a premise towards the selective synthesis of catalytic nanomaterials. In this regard, appropriate atomistic slab models reflecting the actual surface morphologies are of utmost importance. These surface morphologies, however, might differ significantly from any slab model derived from simple bulk-truncation as metal oxide surfaces are known to undergo reorganization during the synthesis and operation.[148–150] To this end, advanced techniques including global structure optimization are required to determine the true active surface structure even for simple single-crystalline surfaces.

Not by chance have surface reconstructions been put forth as explanation for activity increase[124] and decrease[134] in above examples when simpler atomistic models failed.[7]

In the next chapter we will first introduce the most common slab models of IrO_2 and RuO_2 that can be obtained by simple bulk-truncation as they usually provide an adequate initial structure. We then discuss how to classify different slab models based on their surface free energy and finally discuss how to find novel low-energy surface morphologies via global structure optimization of bulk-truncated slab models.

"with a preferential (110) crystal orientation".[147] It will be interesting to see, whether this ambivalence can be attributed to single-crystalline (no LOER) opposed to more polycrystalline (enhanced LOER) materials.

[7] How many of the "rough" and "amorphous" surfaces on closer inspection might actually be reconstructions shall remain undecided at this point.

3 Low-index rutile surfaces: structure, energetics and simulation

3.1 Surface structure

Rutile is the only stable bulk phase of pure IrO_2 and RuO_2 while the anatase phase has only been stabilized for mixed $TiIrO_4$ materials.[151] Accordingly, experimental and theoretical studies exclusively focus on rutile IrO_2/RuO_2 surfaces and so does this thesis.

Rutile crystals are characterized by a tetragonal unit cell that is fully specified by three parameters: the two lattice parameters a and c, and by the projection $x = \langle \mathbf{r}_{\mathrm{IrO}} | \mathbf{a} \rangle$ determining the internal position of the oxygen atoms as illustrated in the left panel of Fig (3.1). The rutile bulk is then obtained by (infinite) repetition of this unit cell.

Each truncating plane in a periodic bulk system represents a surface or facet and in general an arbitrary number of unique surfaces can be generated. A set of parallel lattice planes is fully specified by three integers (hkl) (the Miller indices) which determine the respective surface normal $\mathbf{m}$, orthogonal to all parallel planes. This surface normal is given by $\boldsymbol{m} = (h \cdot \boldsymbol{\alpha}, k \cdot \boldsymbol{\beta}, l \cdot \boldsymbol{\gamma})^\top$ where $\boldsymbol{\alpha}$,$\boldsymbol{\beta}$ and $\boldsymbol{\gamma}$ are the basis of the reciprocal lattice vectors $\mathbf{a}$, $\mathbf{b}$ and $\mathbf{c}$ (for the rutile symmetry we find $\mathbf{a} = (a, 0, 0)$, $\mathbf{b} = (0, a, 0)$ and $\mathbf{c} = (0, 0, c)$). Each unique surface is characterized by a distinct Gibbs surface free energy (SFE) that indicates the energy necessary to create this surface from the infinite bulk system (see next section 3.2). Euhedral, i.e. regular and periodic crystal structures with flat facets, such as pure IrO_2 and RuO_2, try to maximize the surface orientation characterized by the lowest SFE while minimizing energetically higher facets, and are thus preferably growing in one specific direction.[1] The obtained surface mixture usually reflects the relative ordering of the SFEs associated to all possible Miller indices. Since the SFE is depending on external conditions i.a. temperature, (oxygen) pressure and/or solvation, different surfaces orientations can be obtained by varying the growing conditions. Moreover, the growth of one specific orientation can further be enforced by a support crystal (e.g. growing a IrO_2 (110) surface on a TiO_2 (110) support).

Surface orientations with low Miller indices, i.e. only containing 0 and 1 values: $(hkl) = (001)$, (110), (111) etc. are usually characterized by close(r) packed surface structures compared to higher index orientations, with a few exceptions.[153] Following the broken bonds model a higher surface atom density in turn results in lower Gibbs surface free energies.[154, 155] This is especially apparent for single-compound materials like metals where high-index surfaces eventually result in a combination of terraces, edges and kinks of low-index facets due to the discrete crystal lattice. Even though binary crystals are structurally more complex, to our knowledge no high-index single-crystal IrO_2 or RuO_2 surface has been synthesized so far and computational studies accordingly focus mainly on low-index surfaces. The tetragonal symmetry of rutile gives rise to five unique low-index lattice planes: (001), $(010) = (100)$, $(011) = (101)$, (110) and (111), illustrated in the

[1] For nanoparticles this directly leads to Wulff's theorem[152] according to which a nanocrystal adopts a polyhedron structure of minimal surface free energy with a facet ratio that reflect the relative SFEs of all possible crystal surfaces.

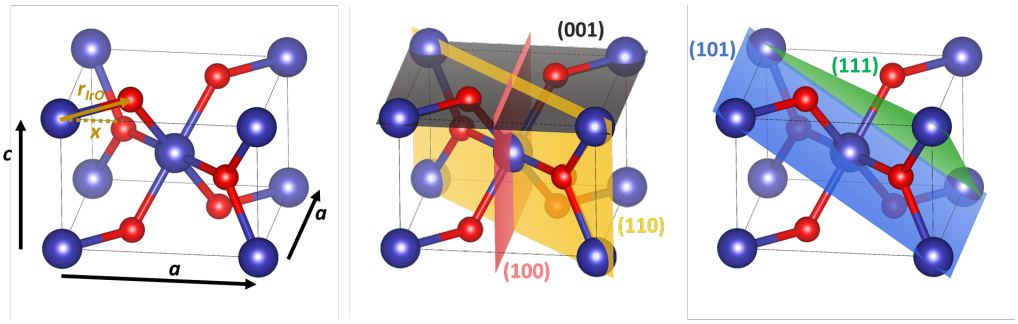

Fig. 3.1: *(Left) Tetragonal unit cell of rutile metal oxides with trigonally coordinated oxygen atoms (red sphere) and octahedrally coordinated metal atoms (blue sphere). The symmetry is fully specified by two lattice parameters a and c and internal projection x. (Middle) Truncating planes arising from* (001) *(black),* (100) *(red) and* (110) *(yellow) Miller indices. (Right) Truncating planes arising from* (101) *(blue) and* (111) *(green) Miller indices.*

two right panels of Fig. 3.1.

For single-compound materials like metals the surface morphology is fully characterized by the orientation and thus the respective Miller index alone. However, for multiple-compound systems each lattice plane may create several different surface morphologies, one for each symmetry-invariant atomic layer of the crystal along the respective surface normal. Depending on the terminating atom layer σ, reflecting the overall stoichiometry at the surface, the respective bulk-truncated slab models of binary metal oxides are denoted either metal-rich, stoichiometric or oxygen-rich. For IrO_2/RuO_2 we find three symmetry-invariant atomic layers for (010), (101) and (110) resulting in one metal-rich, one stoichiometric and one oxygen-rich termination each. Further, for (111) four atomic layers (one metal-rich, two stoichiometric and one oxygen-rich) can be found while for (001) only one bulk-truncation is directly available, which is obviously stoichiometric. Additional terminations can be generated by removing selected atoms of the terminating layer though, as done for the (001) orientation to obtain a metal-rich and an oxygen-rich surface.

The resulting bulk-truncated surface structures are illustrated in Fig. 3.1. Obviously many more terminations might be obtained via adsorption (layers) and/or defects, yet the corresponding investigations must be left for others to do.

In the next section we will show how to approximate the surface free energy of a given morphology in order to compare a set of atomic slab models and determine the most stable surface.

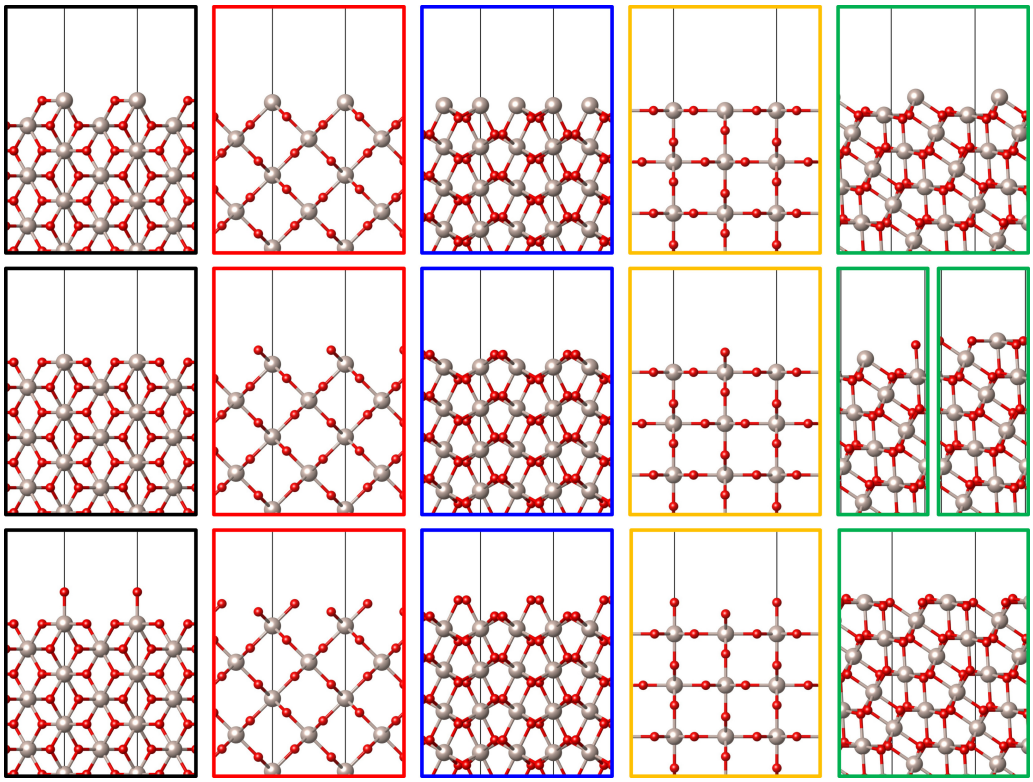

Fig. 3.2: *All bulk-truncated surface structures obtained for low Miller-index orientations of rutile metal oxides. Metal and oxygen atoms are depicted as gray and red spheres, respectively. From left to right,* (001) *(black),* (010) *(red),* (101) *(blue),* (110) *(yellow), and* (111) *(green) surfaces, and from top to bottom, metal-rich, stoichiometric and oxygen-rich. As apparent there are two stoichiometric surfaces for the* (111) *orientation. Furthermore, metal-rich and oxygen rich* (001) *structures have to be artificially generated by removal respectively addition of an oxygen layer.*

3.2 Surface Free Energy

Generally speaking, the Gibbs surface free energy quantifies the energy required to break specific chemical bonds and truncate the bulk system at a certain lattice plane forming the respective surface structure. As long as all accessible facets are characterized by positive SFEs the respective euhedral crystals is stable, indicating that the bulk phase is energetically preferred and that energy is required to form a surface. On the other hand this implies that in case one or more surface morphologies of a material are characterized by a negative SFE, the crystal dissolves as the formation of surfaces is energetically favored.

Even though there exist a couple of ways to experimentally approximate the SFE of solid materials this is restricted to pure metals[156, 157] and polymers[158, 159]. No experimental SFE of IrO_2 has been reported so far. Experimental observation of the growing behavior of IrO_2 at strictly controlled conditions, however, can verify SFEs obtained via first principle methods.

In this thesis the Gibbs surface free energy $\gamma_{\text{surf}}^{(hkl),\sigma}$ of a periodic slab model with Miller index (hkl) and termination σ is calculated via *ab initio* thermodynamics following an approach of Reuter *et al.*[160, 161] which shall be outlined in the following.

In general $\gamma_{\text{surf}}^{(hkl),\sigma}$ of a binary metal oxide system MO_2 is defined as

$$\gamma_{\text{surf}}^{(hkl),\sigma} = \frac{1}{A^{(hkl)}}\left[G_{\text{surf}}^{(hkl),\sigma} - n_{\text{M}}^{(hkl),\sigma}\mu_{\text{M}} - n_{\text{O}}^{(hkl),\sigma}\mu_{\text{O}}\right] \quad , \tag{3.1}$$

where $A^{(hkl)}$ is the surface area and $G_{\text{surf}}^{(hkl),\sigma}$ the Gibbs free energy of the slab model, while the latter two terms include the total number of atoms $n_{\text{X}}^{(hkl),\sigma}$ and the chemical potential μ_{X} of the respective metal M and oxygen O. Note here that the surface area $A^{(hkl)}$ is identical for all terminations σ of a particular orientation (hkl).

Reflecting actual physics, we assume the surface system to be in thermodynamic equilibrium with the respective bulk instead of the atomic species. The Gibbs energy G_{bulk} of a MO_2 bulk unit cell is given as

$$G_{\text{bulk}} = \mu_{\text{M}} + 2\mu_{\text{O}} \quad . \tag{3.2}$$

Now, for any slab model that maintains a stoichiometric composition (e.g. $n_{\text{O}} = 2 \cdot n_{\text{M}}$ for MO_2) we obtain a simple equation for $\gamma_{\text{surf}}^{(hkl),\text{stoich.}}$,

$$\gamma_{\text{surf}}^{(hkl),\text{stoich.}} = \frac{1}{A^{(hkl)}}\left[G_{\text{surf}}^{(hkl),\sigma} - n_{\text{MO}_2}^{(hkl),\sigma}G_{\text{bulk}}\right] \quad , \tag{3.3}$$

where obviously $n_{\text{MO}_2} = n_{\text{M}} = 0.5 \cdot n_{\text{O}}$.
For non-stoichiometric MO_2 slab models this equation gets slightly more complicated as we have to account for deficit/surplus oxygen atoms in metal-rich/oxygen-rich terminations which leads to

$$\gamma_{\text{surf}}^{(hkl),\sigma} = \frac{1}{A^{(hkl)}}\left[G_{\text{surf}}^{(hkl),\sigma} - n_{\text{MO}_2}^{(hkl),\sigma}G_{\text{bulk}} - \Delta n_{\text{O}}^{(hkl),\sigma}\mu_{O}\right] \quad . \tag{3.4}$$

where the oxygen deficit/surplus is given by $\Delta n_{\text{O}}^{(hkl),\sigma} = n_{\text{O}}^{(hkl),\sigma} - 2n_{\text{MO}_2}^{(hkl),\sigma}$.

As apparent for stoichiometric slab models we find $n_O = 2n_{MO_2}$ and hence recover eq. (3.3).

Eq. (3.4) formally covers all binary systems, yet two challenges remain: neither the Gibbs energies ($G_{surf}^{(hkl),\sigma}$ and G_{bulk}) nor the chemical potential of atomic oxygen μ_O is easily accessible on DFT level.

Fortunately, Reuter *et al.* showed that for metal oxides the difference of the two Gibbs energies in eq. (3.4) can be approximated with sufficient accuracy by the difference of the DFT-computed total energies

$$G_{surf}^{(hkl),\sigma} - n_{MO_2}^{(hkl),\sigma} G_{bulk} \approx E_{surf}^{(hkl),\sigma} - n_{MO_2}^{(hkl),\sigma} E_{bulk} \quad . \tag{3.5}$$

In order to access μ_O we again assume equilibrium, this time with the surrounding O_2 gas phase. Based on this assumption μ_O is connected to the total energy of molecular oxygen E_{O_2} in vacuum via $\mu_O = 0.5 \cdot E_{O_2} + \Delta\mu_O$ where $\Delta\mu_O$ is the relative chemical potential. Note here that E_{O_2} includes the experimental zero point energy of oxygen (0.0488 eV[162]) - contrary to E_{bulk} and $E_{surf}^{(hkl),\sigma}$ where it can be neglected.

The SFE is then given as a linear function of the relative chemical potential $\Delta\mu_O$,

$$\gamma_{surf}^{(hkl),\sigma}(\Delta\mu_O) = \frac{1}{A^{(hkl)}} \left[\Delta E^{(hkl),\sigma} + \Delta n_O^{(hkl),\sigma} \Delta\mu_O \right] \quad , \tag{3.6}$$

where the (constant) energy difference $\Delta E^{(hkl),\sigma}$ is calculated based on the total energies of surface, bulk and molecular oxygen,

$$\Delta E^{(hkl),\sigma} = E_{surf}^{(hkl),\sigma} - n_{MO_2}^{(hkl),\sigma} E_{bulk} - 0.5 \Delta n_O^{(hkl),\sigma} E_{O_2} \quad . \tag{3.7}$$

In order to obtain the SFE of a particular facet for the full potential range two calculations are required. In practice we determine the SFE at the chemical oxygen potential of pure O_2, i.e. with $\Delta\mu_O = 0$ and at the chemical oxygen potential within the IrO_2 bulk system,

$$\Delta\mu_O = 0.5(E_{O_2} - (E_{IrO_2} - E_{Ir_{fcc}})) \quad . \tag{3.8}$$

Here $E_{Ir_{fcc}}$ donates the total energy of a metallic iridium atom in its most stable face centered cubic (fcc) phase.[163, 164]

The dependence of the SFE on $\Delta\mu_O$ can be converted into a temperature/pressure dependency for better comparison to actual synthesis conditions, i.e. specific temperatures and oxygen (partial) pressure. In the limit of an ideal-gas-like O_2 atmosphere μ_O is a function of temperature and pressure

$$\mu_O(T, p) = \mu_O(T, p^0) + 0.5 kT \ln\left(\frac{p}{p^0}\right) \tag{3.9}$$

where k is the Boltzmann factor and $\mu_O(T, p^0)$ denotes the temperature dependency of μ_O at a fixed pressure.

Explicit knowledge of the pressure dependency is however not necessary as we are only interested in the chemical potential difference $\Delta\mu_O$ at constant pressure and thus the latter term vanishes. The remaining temperature dependency at fixed oxygen partial pressure (e.g. 0.2 bar for regular air) can be extracted from tabulated experimental data.[165]

In our publications [1] and [2] the results are reported in a Gibbs surface free energy phase diagram illustrating the SFE of all low-index morphologies as a function of $\Delta\mu_O$ (respectively temperature at a fixed O_2 pressure of 0.2 bar). In SFE phase diagrams stoichiometric slabs are independent of $\Delta\mu_O$ since $\Delta n_O^{\text{stoich.}} = 0$ while oxygen-rich and metal-rich surfaces are characterized by a negative respectively positive slope due to $\Delta n_O^{\text{O-rich}} > 0$ and $\Delta n_O^{\text{Ir-rich}} < 0$.

This thermodynamic framework allows an adequate classification of a set of surface morphologies and identification of the most stable structure therein. However, one crucial point has been untouched so far: For a specific surface the bulk-truncated slab model *never* represents the lowest energy structure. Instead relaxation (and potential reorganization) processes might result in a completely new, unexpected structure.

Depending on the degree of structural changes during relaxation/reorganization small to drastically decreased SFEs are observed and just as well affect the relative stability. Any classification based on SFEs should hence always be carried out based on fully relaxed slab models reflecting the actual surface morphology.

In the next section we will discuss how to determine low-energy surface structures via local/global optimization together with the statistical and computational challenges that are encountered especially considering global optimization.

3.3 Simulations and sampling

Low-energy configurations of a given system represent minima of the respective potential energy surface (PES). Since the identification of these minima is a frequent problem in computational chemistry various minimization/optimization techniques have been developed over the years. Most common is a simple structure relaxation via a local optimization starting from an appropriate initial guess, which in present case is the respective bulk-truncated geometry. This approach is comparatively undemanding as a geometry relaxation of (1×1) slab models with appropriate convergence criteria is usually converged within a hundred force/energy evaluations. Surface relaxation of slab models thus can be considered a standard procedure and even prerequisite in todays DFT surface science studies.[15, 37, 42, 43]

However, any local optimization method enforces a downhill progression on the PES and thus only provide access to the structural minimum that can be reached without crossing any energy barrier as illustrated in Fig. 3.3.

Accordingly, the relaxation and thus the minimum are crucially depending on the initial guess. For (small) molecules the most important structural features like bond orders, bond lengths and (dihedral) angles can be estimated beforehand providing a decently good initial guess and consequently a local optimization usually results in a low-energy structure that can be considered the global minimum. On the other hand, the PES of larger molecules like proteins or clusters is often characterized by a multitude of local minima of similar energy which renders the identification of the global minimum difficult.[166]

Crystalline surface structures can be considered somewhere in between, since the bulk-truncated slab model is usually a solid initial guess for a local optimization. However, numerous surface morphologies with reorganized top layers characterized by an atomic connectivity that differs from any bulk-like structure have been observed, including pure metals, such as Au[167, 168] and Si[169], binary materials, e.g. GaAs[170], Cu_2O[171], Fe_xO_y[172, 173] and TiO_2[174, 175] and ternary materials like perovskites[176]. Reorganizations are usually further divided into

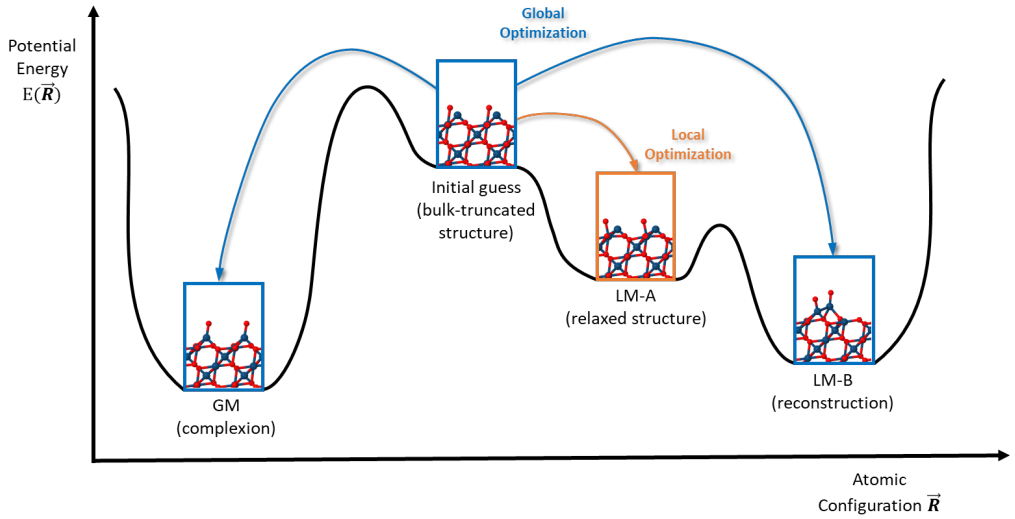

Fig. 3.3: *Illustrative potential energy surface (PES) of a selected surface termination with the potential energy* E *as a function of the atomic configuration* $\vec{R}$*. Local optimization (orange) of the bulk-truncated structure as initial guess will merely lead to a local minimum; the relaxed bulk-truncation (LM-A). A global optimization (blue) is required to identify the second local minimum; the* (2×1) *reconstruction (LM-B) and the global minimum (GM) of this exemplifying PES; a complexion with* (1×1) *periodicity.*

reconstructions and complexions. While a reconstruction changes the size and shape of the surface unit-cell, leading to, e.g. the (4×1) TiO_2 reconstruction[175], the latter preserve a (1×1) periodicity at the surface (compare LM-B and GM of Fig. (3.3), respectively).

Reorganizations are typically not accessible via a local optimization starting from the bulk-truncated slab model as illustrated in Fig. (3.3), instead they are a more distant local or the global minimum for the respective stoichiometry and would require an advanced initial guess that already reflects the final structure in order to be found directly. Yet, selecting an appropriate initial guess to find a still unknown reorganization via local optimization resembles the chicken or the egg dilemma.

Fortunately we can resort to a variety of global optimization (GO) techniques that are (more) independent of the initial structure as they allow to escape local minima, thus drastically improve the PES sampling and the chance to identify an unknown global minimum. It still has to be kept in mind, that there is no valid criterion to ensure that the global minimum is found and hence any global minimum has to be considered tentative.

Modern GO techniques include individual-based methods such as Simulated Annealing[177], Basin Hopping[178]or Monte-Carlo optimization as well as population-based approaches like Differential Evolution[179] or Particle Swarm method[180, 181]. While the former explore the PES based on a single initial structure the latter manipulate a set of structures, i.e. a whole population at once applying different reproduction algorithms. Since a detailed description of any/all of these methods is beyond the scope of this work, the reader is referred to the literature cited above and [166, 182, 183].

All of these techniques share a selection criterion that casually accepts configurations characterized by a higher energy than the initial/previous structure and thus enable to cross energy barriers. Obviously, the number of energy evaluations required to identify the global minimum

grows exponentially with the number of atoms/degrees of freedom and thus a GO based on *ab initio* evaluations is computationally painfully expensive (compared to a local minimization) and still restricted to smaller systems and/or a very limited number of different compositions. A high throughput screening of dozens of structures, e.g. of all low-index, bulk-truncated surface morphologies would to-date require a disproportionate amount of computational resources. In fact, this limitation is even more pronounced if we want to extend our atomistic simulations beyond periodic, single-crystalline model electrodes towards more industrially relevant catalysts, e.g. nanoparticles. For large systems with fixed atomic connectivity, e.g. proteins[184] these costs can be bypassed via classical force fields (FF). FFs approximate the computationally highly demanding electronic structure by parameterized interatomic potentials which makes them multiple orders of magnitude faster than first-principle methods.

It is not surprising at all that also for IrO_2 systems a FF has been parameterized: Sen *et al.* combined a Morse Potential[49] and QEq variable charge model[185] and successfully predict the charge distribution of nanoparticles as well as the oxygen adsorption energies at various surface sites.[47] That said, there is one critical drawback of FFs that ultimately prevented any application in this thesis viz. the general lack of reactivity. Neither bond breaking nor forming can be simulated in (regular) FFs, as fixed atomic connectivities have to be specified together with the input structure. Metal oxide surfaces though are prone to structural changes[148–150], hence the identification of novel surface morphologies demands reactivity. Moreover, the paramount goal is to investigate the OER in aqueous solution, thus simulation methods involved should allow bond breaking/forming. Any attempt to restore reactivity as done for example in the ReaxFF framework[186] inevitably entails an immense number of fitting parameters.

Consequently, we developed a new methodology that adapts a different approach to approximate the atomic interaction without relying on a fixed connectivity: a fully flexible Machine Learning (ML) interatomic potential trained with *ab initio* data. This combined ML/DFT method itself is described and discussed in full detail in my second publication[2], which in turn is briefly summarized in chapter A.2.

That said, the underlying ML theory will be discussed in the next chapter for optimal understanding. This includes a tutorial style example, an introduction of the common descriptor required to represent atomic structures and a discussion on how to select the necessary hyperparameter regulating the ML potential.

4 Gaussian Approximation Potentials in computational chemistry

There exist several Machine Learning (ML) methods, first and foremost based on Neural Networks or the Gaussian Process Regression (GPR) approach that provide fully flexible ML potentials and have been already successfully applied to computational chemistry.[55–66] Inherent to all ML methods in computational chemistry is that they predict properties of an unknown system/structure based on its similarity to configurations within a set of training structures via interpolation. And further that, in order to determine these similarities, atomic structures are transformed into some mathematical representation called descriptors. Accordingly, there are three key factors that define the quality of a ML potential: the available training data, the applied representation/descriptor(s) and, finally, the ML method itself.

Central to my thesis is the Gaussian Approximation Potential (GAP) framework, a chemistry-specific application of the GPR designed to provide straight-forward access to scalable ML potentials for atomic structures.

An in-detail description of the complete mathematical formalism is way beyond the scope of this thesis and instead I highly encourage reading the recent, elaborated review of Deringer *et al.*[54] This review does not only cover the full GPR formalism but also provides a comprehensive discussion on all further GAP-specifics, available representations for chemical structures, heuristics for the hyperparameter selection and a variety of application examples.

Nonetheless, at least the fundamental concepts together with crucial aspects of the GAP model shall be introduced and discussed in this chapter.

Accordingly, the first section 4.1 of this chapter constitutes an introduction of the basic mathematical formalism of the underlying GPR approach including a simple tutorial-style example.

In the second section 4.2 common descriptors/representations of chemical structures together with the concrete form of the similarity measures, the so-called kernels, applied within the GAP model are introduced.

In the final section 4.3 we take a deep dive on the hyperparameters that are required for the GAP model applied in both publications[1, 2] and present a multi-step selection process on how to identify an optimal set of hyperparameters.

4.1 Gaussian Process Regression

In general terms, the GPR model is a non-linear, non-parametric regression tool to approximate a (multi-dimensional) function, e.g. the PES of a chemical system, via interpolation of available data points

As an easy example of the GPR model we examine a smooth, regular, one-dimensional function $y : \mathbb{R} \rightarrow \mathbb{R}$ of unknown form that takes a scalar (e.g. an atomic distance r_{ij}) as input and returns a scalar value (e.g. a binding energy ϵ) shown in Fig. 4.1.

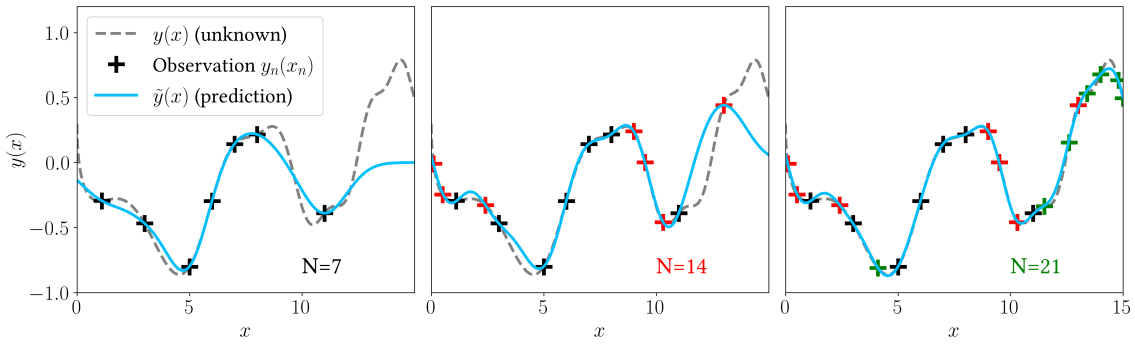

Fig. 4.1: *GPR prediction (solid blue line) of an unknown one-dimensional function (dashed black line) based on an increasing number N of observations $y_n(x_n)$. The regulating hyperparameters are kept unchanged.*

Since the exact form of $y(x)$ is unknown we collect a total of N observations $y_n \equiv y_n(x_n)$ of independent input values x_n. These N input-return pairs are collected as training data in a so-called training set $D_{\text{1-d}} = \{x_n : y_n\}_{n=1}^{N}$. Obviously the prediction is improving with an increasing number of observations (for an otherwise identical GPR model). In Fig. 4.1 the increasing agreement of prediction $\tilde{y}(x)$ and true function $y(x)$ with an increasing number of data points is illustrated.

Integral to the GPR model is its formalism to approximate the true (yet unknown) function value $y(x)$ for an arbitrary input x as a linear combination of M basis function,

$$y(x) \approx \tilde{y}(x) = \sum_{m=1}^{M} c_n k(x, x_m) \quad , \tag{4.1}$$

with the similarity measure $k : \mathbb{R} \times \mathbb{R} \rightarrow \mathbb{R}$, commonly referred to as kernel (functions) within the GPR/GAP framework and a set of coefficients $\mathbf{c} = (c_1, ..., c_M)$ that are normalized, i.e. $|\mathbf{c}| = 1$ and yet to be determined.

For sake of simplicity, we will discuss the *full* GPR in the following with $M = N$ and $\{x_m\} \equiv \{x_n\}$, i.e. where each basis function represents precisely one observation. An overview on the implications arising from a *sparse* GPR can be found in the appendix C.

Coming back to our example: to determine the similarity between an arbitrary input x and a training data point x_m a Gaussian kernel is applied, which in the one-dimensional case is simply given by

$$k(x, x_m) = \exp\Big[- \frac{|x - x_m|^2}{2\theta^2} \Big] \quad , \tag{4.2}$$

where the Gaussian width θ is the first example of a hyperparameter which in this specific case regulates the smoothness of the similarity measure.

The coefficients are now determined based on the available training data $D_{\text{1-d}}$ via the loss function,

$$l = \sum_{n=1}^{N} \frac{[y_n - \tilde{y}_n]^2}{\sigma_n^2} + R(c_n) \quad , \tag{4.3}$$

with individual weights σ_n reflecting the uncertainty (and/or importance) of an observation y_n and

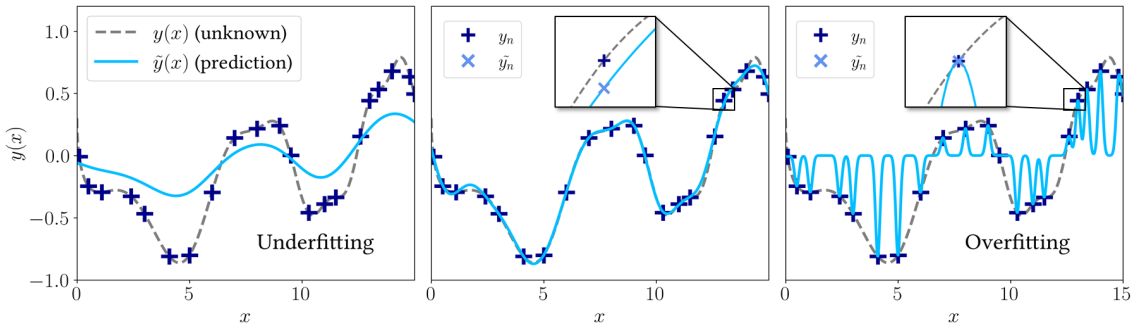

Fig. 4.2: *Effect of regularization σ_u and kernel width θ on the GPR prediction (solid blue line). For a strong regularization (large σ_u) the prediction function $\tilde{y}(x)$ is increasingly centered around the average of the observations ($\overline{y_n}$), which is referred to as overfitting (left panel). For a small regularization σ_u and/or kernel width θ a close agreement of observation y_n and prediction $\tilde{y}_n$ is achieved at the cost of high uncertainty for any unknown input values $x \neq x_n$, which is referred to as overfitting (right panel). Balancing smoothness and accuracy with appropriate regularization and kernel width will provide an optimal prediction (mid panel).*

a regularization function $R(c_n)$[1]. Note here that $\tilde{y}_n \equiv y(x_n)$ and thus also the first term depends on the coefficients due to eq. (4.1).

Assuming that we observe or expect similar uncertainties for all observations y_n, a uniform weight σ_u can be applied and eq. (4.3) simplifies to

$$l = \sum_{n=1}^{N} [y_n - \tilde{y}_n]^2 + \sigma_\mathrm{u}^2 R(c_n) \quad . \tag{4.4}$$

The missing coefficients can then be determined via minimization of this loss function (see appendix B).

Both terms of eq. (4.4) are required to provide a well-rounded prediction as they are balancing two contrary aspects of the interpolation: accuracy and smoothness. The first term is highly flexible and ensures an accurate description of the actual training data while the regularization prevents coefficient from getting too large and thus (together with the kernel width θ) guarantees a smooth interpolation in between training points. An appropriate combination of these two terms makes the prediction of unknown input possible in the first place.

With decreasing regularization and/or kernel width ($\sigma_\mathrm{u}, \theta \to 0$) we obtain an increasingly close agreement of training data and prediction, $y_n \to \tilde{y}_n$, until eq. (4.4) is eventually reduced to a least-square fit (for $\sigma_\mathrm{u} = 0$). However, as illustrated in the right panel of Fig. 4.2 this precision is achieved at the expense of rapidly increasing uncertainty for any unknown input values. An insufficient regularization in combination with a small kernel width is usually referred to as overfitting. Too much regularization, on the other hand, will lead to so-called underfitting illustrated in the left panel of Fig. 4.2 since for $\sigma_\mathrm{u} \to \infty$ the prediction will yield the average of all the training data, $\tilde{y}(x) = \overline{y_n}$. Vividly spoken, the regularization enforces a non-perfect description of the training data with $\tilde{y}_n \neq y_n$, (compare inlets of Fig. 4.2) but ensures that the interpolation is meaningful/non-zero in between two observations.

In this simple GPR example we only have to select two hyperparameters, the uniform regu-

[1]Within the GAP model the Tikhonov regularization[187] is used.

larization strength σ_u and the kernel width θ. We will, however, see in the following that more hyperparameters are required to regulate an actual GAP.

Obviously, there are several aspects in which the more complex GAP model differs from this very simple, one-dimensional example above. First and foremost the GAP model constitutes a *sparse* GPR, with $M \ll N$ in order to achieve better scalability and transferability (see appendix C). Furthermore, the GAP training data usually contains derivatives of the observation as well, namely the atomic forces with the implications and the mathematical formalism covered in Ref. [54]. To account for the generally larger deviation (uncertainty) of atomic forces two different weights σ_ε and σ_f distinguishing between these two types of intrinsically different training data are applied. And finally, in the GAP framework the observations, i.e. the total energies E_{tot} are separated into local energy contributions ε_i that are then predicted based on local representations/descriptors. In the next section we thus will introduce suitable representations/descriptors for atomic structures together with the respective similarity measures/kernels.

4.2 Representing atomic structures

The most intuitive and well known representation of an atomic structure is a list of Cartesian coordinates. However, a Cartesian representation is not well-suited to determine similarities between two configurations as it depends on the concrete ordering and the external coordinate system. Translation or rotation will leave the configuration and thus all chemical properties unchanged, yet the effect on the corresponding Cartesian representation is arbitrarily large. In addition, multiple different representations can be generated by simply swapping atoms of the same element, again without changing total energy nor configuration. A ML model with a similarity measure based on Cartesian representations would thus require an enormous amount of redundant training data to account for structural identical configurations. Evidently, we are looking for a representation that is invariant to translation, rotation and permutation.

In addition, the discrete, non-regular nature of the Cartesian representation makes a similarity measure anything but an easy task. If, for instance, all atomic positions are subject to an infinitesimal displacement, the resulting configuration while in fact of almost unchanged total energy is unknown and it remains unclear how to relate structural and energetic changes. Furthermore, but on a similar note, a differentiable, regular energy expression is mandatory to extract atomic forces and conduct any kind of MD simulations.

Consequently, as a second premise we demand a smooth, differentiable interpolation which in turn requires either a smooth, differentiable representation or kernel function.

In the following we discuss three representations and their kernel functions that are commonly used within the GAP model as they - by design - meet these requirements: two-body, three-body and Smooth Overlap of Atomic Positions (SOAP) descriptor.

4.2.1 Two-body and three-body descriptor

One simple way to guarantee rotational, translational and permutational invariance is to represent a structure via a set of atomic distances $\{r_{ij}\}$ accounting for all (eligible) atom pairs i and j. However, in order to compare a set of distances (representing an unknown test structure) to the available training data we have to apply a smooth and regular kernel function since the distances themself constitute a discrete representation. In contrast to a Cartesian representation this is a straight-forward task as the scalar two-body descriptor resembles the basic, one-dimensional

example discussed in section 4.1, where regularity was clandestine introduced via the applied kernel function. Consequently and analogous to eq. (4.2), the two-body kernel $k_{2b} : \mathbb{R} \times \mathbb{R} \to \mathbb{R}$ providing a similarity measure of two distances r_{ij} and r_m is defined as

$$k_{2b}(r_{ij}, r_m) = \exp\Big[- \frac{|r_{ij} - r_m|^2}{2\theta_{2b}^2} \Big] \quad , \tag{4.5}$$

where the hyperparameter θ_{2b} (two-body kernel width) regulates the smoothness of the kernel.

The total energy of the test structure is then approximated based on the sum over all distances r_{ij}, each one compared to the distances r_m in the training set via the two-body kernel

$$E_{2b}(\mathbf{r}) = \sum_{ij} \varepsilon_{2b,ij} = \sum_{ij} \sum_{m}^{M_{2b}} c_{2b} k_{2b}(r_{ij}, r_m) \quad , \tag{4.6}$$

where $\mathbf{r} = \{r_{ij}\}$ contains all distances up to a system- and kernel-specific cutoff radius $r_{\text{cut,2b}}$. As already indicated above, rather than evaluating the kernel at each of the N_{2b} atomic distances included in the training set, it is evaluated at a much smaller number of M_{2b} sparse points.

The most evident shortcoming of this pair-wise decomposition is the lack of angular information, i.e. the neglection of energy contributions arising from the relative position of three (or more) atoms. An obvious way to account for angular information is the addition of the corresponding three-body terms. The total energy is then given by

$$E_{2b/3b} = \sum_{ij} \sum_{m} c_{2b} k_{2b}(r_{ij}, r_m) + \sum_{ijk} c_{3b} k_{3b}(r_{ij}, r_{ik}, r_{kj}) \quad , \tag{4.7}$$

where the three-body kernel $k_{3b} : \mathbb{R}^3 \times \mathbb{R}^3 \to \mathbb{R}$ sums over all atom triplets in the training data and has to be differentiable.

In principle, the energy approximation can be refined as required by including higher orders, e.g. four-body terms. Unlike the two-body term though, higher order terms are not per se invariant to permutation and the exponential increasing number of contributions makes it more and more difficult to ensure permutational invariance.

4.2.2 Smooth Overlap of Atomic Positions descriptor

Instead of approximating the total energy via a set of two-body (and/or higher order) contributions, the total energy can also be separated into local contributions ε_i of atomic environments via

$$E_{MB} = \sum_{i} \varepsilon_i = \sum_{i} \sum_{m}^{M_{MB}} c_{MB} k_{MB}(\boldsymbol{\xi}_i, \boldsymbol{\xi}_m) \quad , \tag{4.8}$$

which in turn are approximated based on a many-body kernel $k_{MB} : \mathbb{R}^d \times \mathbb{R}^d \to \mathbb{R}$ at M_{MB} sparse points and multi-dimensional descriptor $\boldsymbol{\xi}_i$ representing the respective local atomic environments.

One many-body representation that fulfills permutational and translational invariance is the radial distribution function or the neighbor density. To convert the neighbor density into a smooth, differentiable description, the atomic positions are represented by Gaussian functions instead of Dirac delta functions. Since we further want to differentiate between different atomic species α, a

set of element-specific neighbor densities $\{\rho^{i,\alpha}\}$ for each central atom i is extracted. The smooth neighbor density of atom i representing its atomic environment w.r.t. to the element α is then given by

$$\rho^{i,\alpha}(\mathbf{r}) = \sum_j \delta_{\alpha,\alpha_j} \exp\Big[\frac{-|\mathbf{r}-\mathbf{r}_{ij}|}{2\theta^2_{\mathrm{MB},\alpha}}\Big] f_{\mathrm{cut}}(r_{ij}) \quad , \tag{4.9}$$

where $\theta_{\mathrm{MB},\alpha}$ is an element-specific descriptor width[2], the delta function δ_{α,α_j} assures that the sum is only including neighbor atoms j of species α and the cutoff function, $f_{\mathrm{cut}}(r)$ smoothly approaches zero at a given $r_{\mathrm{MB,cut}}$. In the present thesis we apply a uniform descriptor width θ_{MB} throughout.

While $\rho^{i,\alpha}(\mathbf{r})$ is invariant to permutation and translation, the rotational invariance has yet to be introduced. To this end we expand the neighbor density in the basis of orthogonal radial functions $R_n(r)$ and spherical harmonics $Y_l^m(\mathbf{r})$,

$$\rho^{i,\alpha}(\mathbf{r}) = \sum_{nlm} c^{i,\alpha}_{nlm} R_n(r) Y_l^m(\mathbf{r}) \quad . \tag{4.10}$$

To truncate this infinite basis we have to choose $n_{\max}$ and $l_{\max}$ (with $m \in [-l_{\max}, l_{\max}]$), similar to the representation of atomic orbitals in a radial basis.

The expansion coefficients $c^{i,\alpha}_{nlm}$ are then obtained via integration

$$c^{i,\alpha}_{nlm} = \int d\mathbf{r} R_n(r)^* Y_l^m(\mathbf{r}) \rho^{i,\alpha}(\mathbf{r}) \quad . \tag{4.11}$$

We now sum over m and obtain a rotationally invariant, symmetrized combination of the expansion coefficients referred to as power spectrum $\mathbf{p}_i = \{p^{i,\alpha\alpha'}_{nn'l}\}$. The individual vector elements are calculated via

$$p^{i,\alpha\alpha'}_{nn'l} = \frac{1}{\sqrt{2l+1}} \sum_m (c^{i,\alpha}_{nlm}) * c^{i,\alpha'}_{n'lm} \quad . \tag{4.12}$$

Finally the SOAP representation of atom i is obtained by normalizing the power spectrum

$$\boldsymbol{\xi}_i = \frac{\mathbf{p}_i}{|\mathbf{p}_i|} \quad . \tag{4.13}$$

As opposed to the two-body representation, the SOAP descriptor itself is already differentiable and thus the respective kernel is readily available

$$k_{\mathrm{MB}}(\boldsymbol{\xi}_i, \boldsymbol{\xi}_j) = (\boldsymbol{\xi}_i \cdot \boldsymbol{\xi}_j)^\zeta \quad , \tag{4.14}$$

where the order of the polynomial is determined by the hyperparameter ζ. Note that, ζ is directly related to the body order of interaction as, e.g. $\zeta = 2$ corresponds to a 5-body term (for an elaborated discussion on the body order see page 14 Ref. [54]).

[2]Note here that while $\theta_{2\mathrm{b}}$ and θ_{MB} both constitute a Gaussian width, the former is part of the two-body kernel (thus kernel width) and the latter is incorporated directly in the SOAP descriptor (hence descriptor width).

4.2.3 Combined two-body and SOAP representation

In general the representation of an atomic structure is not limited to one single descriptor. Just on the contrary, most ML applications apply a combination of different descriptors. While a pure SOAP description is possible, the explicit addition of two-body descriptors has been shown to guarantee a significantly more stable potential for atomic structures. Hence in the present work we applied a combination of two-body and SOAP representation. The intention with this combined representation is to reproduce the main features of the PES by the two-body potential while the additional SOAP contribution then accounts for the subtlety of the PES.

Combining eq. (4.6) and (4.8) the total energy of the system is approximated via

$$E_{\text{2b+SOAP}} = \sum_{ij} \delta_{\text{2b}} \sum_{m}^{M_{\text{2b}}} c_{\text{2b}} k_{\text{2b}}(r_{ij}, r_m) f_{\text{cut}}(r_{ij}) + \sum_{i} \delta_{\text{MB}} \sum_{m}^{M_{\text{MB}}} c_{\text{MB}} k_{\text{MB}}(\xi_i, \xi_m) \quad , \tag{4.15}$$

Two additional hyperparameters δ_{2b} and δ_{SOAP} are scaling (the respective basis functions of) the two contributions. Note here, that these two hyperparameters are not enforcing a strict ratio but rather provide a corridor for each contribution as the coefficients c_{2b} and c_{MB} can counteract the δ-ratio to a certain extent.

As apparent, the application of a combination of more sophisticated representation requires significantly more hyperparameters than the simple tutorial example of section 4.1. Accordingly, the hyperparameter selection method applied in this thesis will be discussed in the final section.

4.3 Hyperparameter selection

Especially when dealing with a training set that is extended iteratively, as it is the case in this thesis, selecting appropriate hyperparameter is a delicate task[54], We further have to account for the fact that, no high-temperature structures were considered as training data in order to maintain a cost-efficient training protocol. Yet a sufficiently accurate description of the high-temperature regime is necessary to obtain meaningful results via Simulated Annealing. A strict optimization of the hyperparameters w.r.t the initial training data is hence ill-advised as it would inevitably lead to a poor description of both, high-temperature and unknown minimum structures compromising the whole global optimization.[3]

The applied hyperparameters should thus provide a flexible but smooth PES enabling enough room for exploration without sacrificing a sufficiently accurate description of the already identified PES minima. While an exact realization is easier said than done the application of various hyperparameter sets throughout this thesis revealed that, in praxis, the precise identification of the *best* hyperparameters is not necessary, as exemplary discussed for two hyperparameter sets in section 4.3.5. Instead it was found that either a range of similarly well-performing parameters exists (σ's) or well-founded heuristics (θ's) or even independent metrics (r_{cut}) can be applied.

While far from constituting an universal method for the quantitative determination of a perfect set of hyperparameters for any given system, the semi-systematic selection process applied within this thesis shall be outlined and discussed in the following. May this multi-step selection and/or its flaws provide guidance (and confidence) for future work.

[3] Obviously this does not apply to those hyperparameters that regulate truncation, in particular the number of sparse points $M_{\text{2b}}/M_{\text{MB}}$ and $n_{\text{max}}/l_{\text{max}}$. Here a larger value will always provide a more precise description, at the expense of (exploding) computational costs - a challenge very familiar from *ab initio* calculations.

In total we have to select 13 hyperparameters to train a GAP applying a combination of two-body and SOAP descriptors which include

- three two-body specific hyperparameters: the cutoff $r_{\text{cut,2b}}$, the kernel width θ_{2b} and the number of basis function, i.e. sparse points M_{2b}
- six SOAP specific hyperparameters: the cutoff $r_{\text{cut,MB}}$, the descriptor width θ_{MB}, the power spectrum truncation parameters n_{max} and l_{max}, the number of sparse points M_{MB} and the body order ζ
- four hyperparameters to regulate the GAP itself: the two two scaling factors δ_{2b} and δ_{2b} as well as two regularization factors/weights σ_ε and σ_{f} accounting for the intrinsically different uncertainty (deviation) of total energies and atomic forces.

In the present work the number of hyperparameters is reduced as a fixed body order ($\zeta = 2$) and a global cutoff $r_{\text{cut}} = r_{\text{cut,MB}} = r_{\text{cut,2b}}$ has been applied.

Preceding to the hyperparameter selection itself we first introduce the concept of cross-validation in section 4.3.1 since it has been applied multiple times within the selection process. In section 4.3.2 we then introduce the so-called locality test, a data- and method-independent way to determine an appropriate cutoff r_{cut}. In a second step optimal hyperparameters of a pure two-body potential are identified, as outlined in section 4.3.3 . Finally, in a nested cross-validation process the remaining SOAP parameters are extracted, as discussed in section 4.3.4.

4.3.1 Cross-validation

One way to select optimal hyperparameters solely based on the available training data is cross-validation. The general concept of a four-fold cross-validation as applied in our hyperparameter selection process is illustrated in Fig. 4.3. At first all structures, that are considered mandatory for a GAP training are collected separately (in present case these are the O_2 dimers and the IrO_2/RuO_2 unit cell) while the remaining training structures are randomly divided into four subsets.

To evaluate a specific set of hyperparameters four GAPs are trained based on combinations of mandatory structures and three subsets. The mean absolute error (MAE) of total energies and atomic forces w.r.t. the *ab initio* reference are extracted based on the remaining subset to avoid/reduce overfitting. To quantify the performance the resulting average MAEs of energies (MAE_ε) and forces (MAE_{f}) are scaled and combined: $MAE = MAE_\varepsilon + 0.1 \cdot MAE_{\text{f}}$ reflecting the generally larger deviation of the atomic forces.

4.3.2 Locality test

By applying a cutoff r_{cut} and dividing the total energy into local contributions the GAP model effectively neglects any long-range interactions arising from, e.g. electrostatics or dispersion. There is - so far - no applicable work around to implicitly or explicitly incorporate long-range effects without sacrificing reactivity. These interactions are thus adding to the uncertainty or noise we observe in a GAP model as two central atoms characterized by identical atomic configuration inside r_{cut} (i.e. identical atomic environments) might still be characterized by different forces due to structural differences outside r_{cut}.

The success of GAPs with finite cutoffs for a multitude of diverse systems can generally be accounted to screening effects, which introduces full or at least sufficient locality in, e.g. insulators,

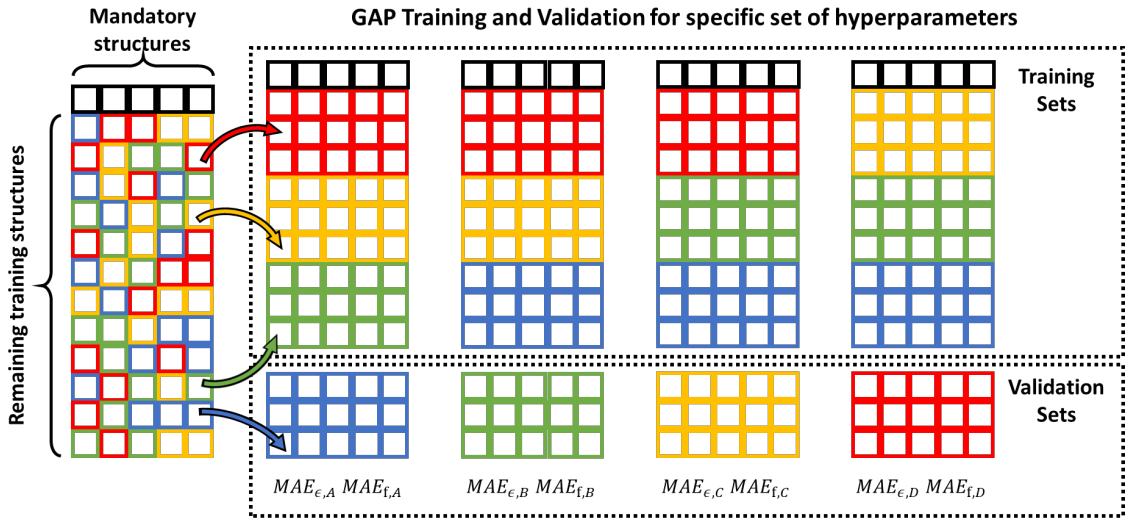

Fig. 4.3: *In a four-fold cross-validation the available data is divided into mandatory structures (black) and four randomly composed subsets (red, yellow, green and blue). Four GAPs are trained on combinations of mandatory structures and three subsets. The mean absolute errors of total energies $MAE_{\epsilon,X}$ and atomic forces $MAE_{f,X}$ are extracted based on the remaining subset. The average MAEs are scaled and combined to quantify the performance of the set of hyperparameters.*

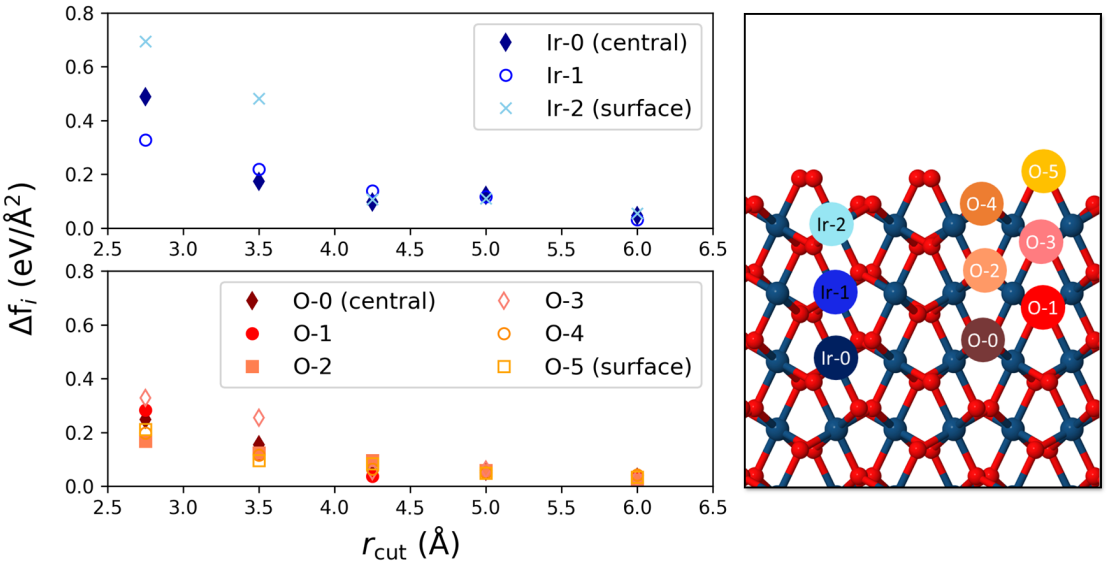

Fig. 4.4: *Locality test of the oxygen-rich (101) IrO_2 surface. Induced force on a given central atom upon displacement of atoms outside a radius r_{cut}. To provide some statistics, three different central atoms are considered for each of the nine outermost atomic layers in the slab as illustrated in the panel on the right. Reproduced from reference [2], with the permission of AIP Publishing.*

metals/metallic systems and a variety of liquids. In general, there exists a material-specific upper limit of force accuracy for a given cutoff radius that depends only on the degree of locality of this material. In other words, this minimum uncertainty is completely independent of the applied ML model, descriptors or amount of training data. Whether a localized ML model is applicable and - if so - which cutoff radius r_{cut} provides reasonable small force errors thus can and should be estimated via DFT calculations beforehand in a so-called locality test:

Starting from a regular configuration $\mathbf{R}$ we generate a set of *rattled* configurations $\{\mathbf{R}'\}$ characterized by small displacements of atoms outside an increasing cutoff radius r_{cut} around a central atom i. The induced force at atom i, i.e. the force difference of regular and *rattled* configuration $\Delta \text{f}_i = |\mathbf{f}_i^{\mathbf{R}'} - \mathbf{f}_i^{\mathbf{R}}|$ as a function of the cutoff as obtained from *ab initio* single-point calculations is a measure for the local character of the system.

Obviously this metric strongly depends on the magnitude of displacement which has to be chosen with care and w.r.t. the underlying physics of the system. In the present thesis small, random perturbations taken from a uniform distribution of standard deviation 0.05 Å are applied as we are actually interested in the convergence of Δf_i only. If instead a specific minimum accuracy (i.e. maximum Δf_i) is required, the rattled structures $\{\mathbf{R}'\}$ would have to be taken from a MD simulation (at the requested temperature) to guarantee meaningful, more physical atomic displacements.

In Fig. 4.4 the results of a locality test of the oxygen-rich (101) IrO_2 surface structure is illustrated. To provide some statistics, the average induced force of three different atoms for each of the three respectively six unique iridium and oxygen layers of this slab model has been calculated. As apparent Δf_i decays rapidly with increasing r_{cut} and initial differences between surface and bulk layers vanish for $r_{\text{cut}} > 4.25$ Å.

4.3.3 Pure two-body potential

Next a pure two-body potential is trained that is intended to cover large parts of the total energy and interatomic interactions. Besides r_{cut} there are five hyperparameters that have to be selected in order to obtain a two-body potential, viz. $M_{2\text{b}}$, $\theta_{2\text{b}}$, $\delta_{2\text{b}}$, σ_ε and σ_f. Note here that the regularization parameters σ_ε and σ_f are preliminary and will be updated for the combined two-body and SOAP representation.

Besides the MAEs of total energies and forces the atomic pair potential serves as an independent validation since a two-body potential should be able to describe this pure two-body interaction appropriately.

In general the regularization parameters $\sigma_\varepsilon/\sigma_\text{f}$ and $\delta_{2\text{b}}$ are strongly correlated (compare eq. (4.4) and eq. (4.15)) and it can be assumed that several similarly well-performing parameter sets exist. A *perfect* selection of $\delta_{2\text{b}}$ (or $\sigma_\varepsilon/\sigma_\text{f}$) upfront is thus not imperative - on the contrary, seeking for *perfection* is probably not the most on-point description of what is requested here. Instead we first provide a reasonable scaling factor based on an easy heuristic in full awareness that we still can account for possible imperfections afterwards via adapting the regularization hyperparameters accordingly.

In a pure two-body potential $\delta_{2\text{b}}$ scales the individual pair contributions to the total energy and should hence reflect the respective binding energies which can be approximated via the atomic cohesive energy E_i^{coh} within the initial training. In the present thesis $\delta_{2\text{b}}$ is then extracted based

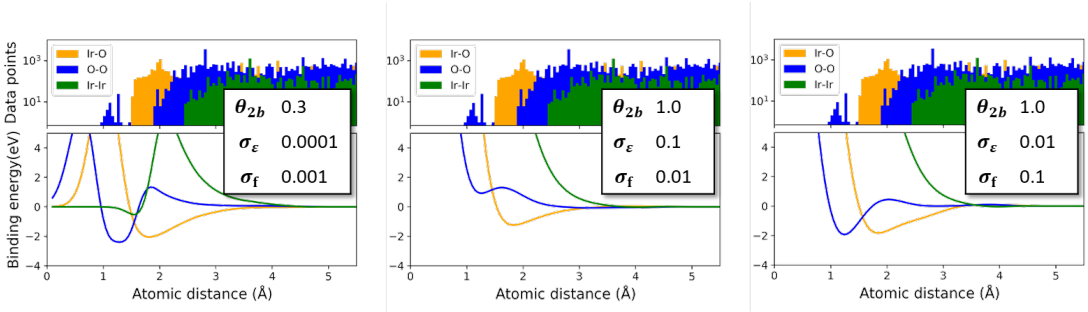

Fig. 4.5: *Atomic pair potential for three different sets of hyperparameters based on the initial IrO_2 training set. In the lower and upper part of each panel the GAP predicted binding energy respectively the number of corresponding two-body distances in the training set as a function of distance between two Ir atoms, two O atoms and an Ir-O atom pair is shown. A small kernel width θ_{2b} (left panel) or poorly selected regularization (mid panel) results in partially overfitted and/or non-physical pair potentials. As discussed in the text a more pronounced force regulation ($\sigma_f > \sigma_\varepsilon$) consistently provides better results (right panel).*

on the standard deviation of E_i^{coh},

$$\delta_{2b} = \frac{1}{b_{2b}} \sum_{i=0}^{N} \frac{\left(E_i^{coh} - \overline{E}_i^{coh}\right)^2}{N-1} \quad , \tag{4.16}$$

that is weighted by a bond order term b_{2b} to account for multiple two-body descriptors per atom and thus per atomic cohesive energy. According to the bulk dominant training set we simply apply the IrO_2 bulk bond order $b_{2b}^{IrO_2} = 4$ here, even though a slightly decreased bond order reflecting the non-negligible share of surface atoms within the training set might be selected as well.

It has to further be noted that eq. (4.16) assumes a distribution of the binding energies around zero which, to be honest is far-stretched. It would probably be more accurate to extract the scaling factor based on an average of E_i^{coh} divided by the average number of **all** pair contributions r_{ij} within the cutoff instead. However, as rationalized above, even with a potentially poorly chosen scaling factor, the resulting GAP provides reasonable results (see section 4.3.5).

The initial intention was to determine the remaining four hyperparameters via a four-fold cross-validation as described in section 4.3.1. However, the obtained parameters ($M_{2b} = 25$, $\theta_{2b} = 0.3$, $\sigma_\varepsilon = 0.001$ and $\sigma_f = 0.0001$) yield an overfitted atomic pair potential as illustrated in the left panel of Fig. 4.5. While the number of sparse points $M_{2b} = 25$ seemed reasonable and of only minor influence on the pair potential, it turned out that a larger kernel width $\theta_{2b} > 0.5$ is required to obtain a more physical pair potential. Yet even for an appropriate kernel width the pair potential still depends crucially on the regularization parameters and might lead to non-physical pair interaction as illustrated in the middle panel. The generally larger uncertainty of the atomic forces in comparison to the total energies should also be reflected in a more pronounced regulation, i.e. $\sigma_f > \sigma_\varepsilon$ and we consistently obtain better results when implementing this insight as exemplified in the right panel of Fig. 4.5.

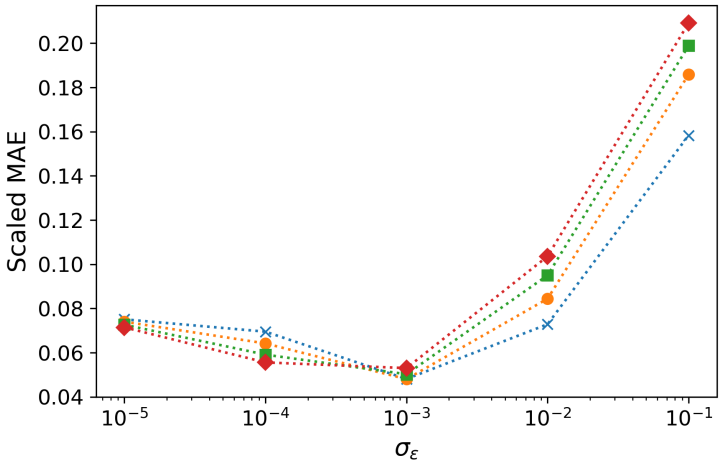

Fig. 4.6: *Scaled MAE of energy and forces for different regularization parameters (σ_ε,σ_f) obtained via a four-fold cross-validation The pair of energy and force regularization parameters is determined based on pre-selected σ_ε:σ_f ratios with $\sigma_\varepsilon < \sigma_\mathrm{f}$ including 5 (blue cross), 10 (orange circle), 15 (green square), 20 (red diamond). The minimum is identified for $\sigma_\varepsilon = 10^{-3}$ and $\sigma_\mathrm{f} = 10^{-2}$. Reproduced from reference [2], with the permission of AIP Publishing.*

4.3.4 Adding the SOAP description

To complete our combined representation we have to select the four remaining SOAP descriptor hyperparameters viz. θ_MB, n_max, l_max and M_MB, the scaling factor δ_MB and the final regularization parameters σ_f and σ_ε.

As already stated above the SOAP contribution is intended to reproduce the nuances of the PES not captured by the two-body potential. Accordingly, the scaling factor δ_MB is related to the difference of the atomic cohesive energies $\Delta E_i^\mathrm{coh} = |E_i^\mathrm{DFT,coh} - E_i^\mathrm{2b,coh}|$ of pure two-body description and the DFT reference within the initial training set via

$$\delta_\mathrm{MB} = \sum_{i=0}^{N} \frac{\left(\Delta E_i^\mathrm{coh} - \overline{\Delta E}_i^\mathrm{coh}\right)^2}{N-1} \quad , \tag{4.17}$$

where in comparison to eq. (4.16) no weight is required since we have exactly one descriptor per atom and thus per atomic cohesive energy. Further note here that the SOAP contributions are presumably centered around zero which makes eq. (4.17) a decent choice.

Instead of optimizing the missing six hyperparameters in a single grid search, which would require an excessive amount of evaluations, we conduct a three-stage grid search, consecutively optimizing matching hyperparameter pairs via a four-fold cross-validation.

In the first step only the regularization is investigated while the remaining parameters are kept fix. Here the unknown convergence parameters are simply selected such that they ensure a highly accurate (yet expensive) description with $n_\mathrm{max} = 15$, $l_\mathrm{max} = 10$ and the maximum possible number of sparse points $M_\mathrm{MB,max}$ (see appendix C). The missing descriptor width is actually more tricky since it is no convergence parameter. From previous work though $\theta_\mathrm{MB} = 0.5$ seemed appropriate, accounting for the fact, that the SOAP potential should be more precise, i.e. less smooth than the

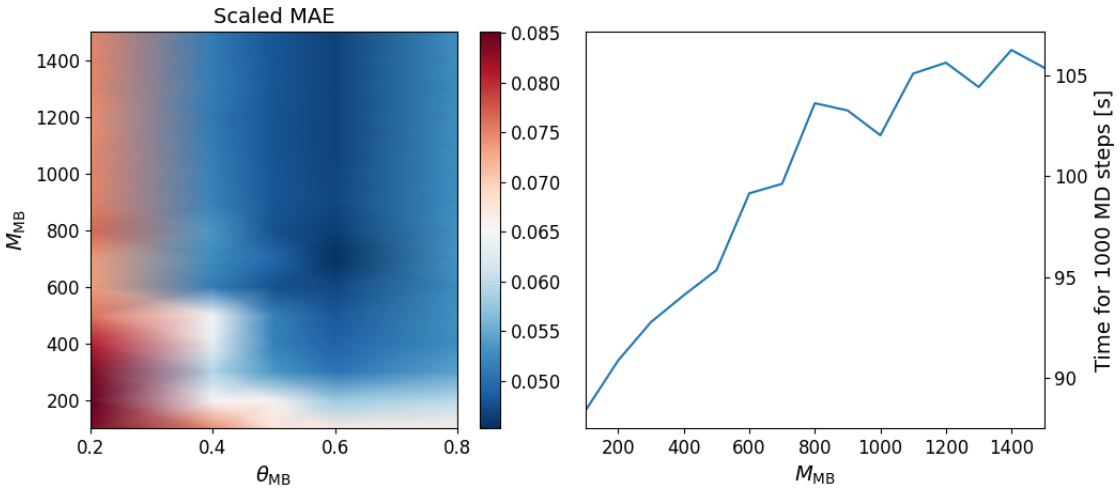

Fig. 4.7: *Scaled MAE of energy and forces as a function of the number of sparse points M_{MB} and SOAP descriptor width θ_{MB} as obtained from a four-fold cross-validation (left) and average computational costs as a function of M_{MB} taken from a 5000 steps MD simulation of the metal-rich (101) IrO_2 surface (right).[188] The minimum w.r.t. to the descriptor width is identified for $\theta_{MB} = 0.6$. Due to only marginally increasing computer costs for increasing number of sparse points we settle for an exceeding $M_{MB} = 2000$ since we are anticipating a significantly larger final training set (see text).*

two-body potential with $\theta_{2b} = 1.0$. This is also within the recommended width range as reported in Ref. [54]. The optimization is then performed on a logarithmic grid for four different σ_f:σ_ε ratios as illustrated in Fig. 4.6 and the optimal regularization is determined to be $\sigma_\varepsilon = 10^{-3}$ and $\sigma_f = 10^{-2}$. Attention might further be drawn to the fact that multiple hyperparameter sets perform almost identical as already pointed out in the beginning.

In a second step the number of sparse points M_{MB} and the descriptor width θ_{MB} are investigated. The performance results are shown in the left panel of Fig. 4.7. Furthermore, the average computational costs as a function of M_{MB} is illustrated in the right panel since the number of sparse points is a convergence parameter. We observe a plateau with similarly well performing parameter sets for $\theta_{MB} > 0.3$ and $M_{MB} > 600$.

As a matter of fact, the computational costs do not increase as rapidly as expected and therefore we select $M_{MB} = 2000$. While this is well beyond the number of atoms N_{at} for the initial training set and will hence be decreased automatically as long as $N_{at} < 2000$ by the GAP formalism (see appendix C), it ensures that the computational costs are capped for the constantly extended training set. Obviously this also implies that the accuracy is limited and might decrease, if $N_{at} > 2000$. Indeed the final training set of [2] includes slightly more than 2000 iridium and well beyond 3000 oxygen environments, yet we do not observe a severe drop in accuracy at this point.

In a final step the influence of the two remaining hyperparameters n_{max} and l_{max} on the scaled MAE is investigated as illustrated in the right panel of Fig. 4.8. Here the plateau is even more pronounced with almost identical MAEs for $n_{max} > 6$ while the influence of l_{max} is basically negligible indicating a minor dependence on the angular information - at least for the initial training. In stark contrast, the computational costs increases exponentially with larger n_{max} and l_{max}. We thus settle for $n_{max} = 8$ and $l_{max} = 4$ providing an almost converged description at very reasonable costs.

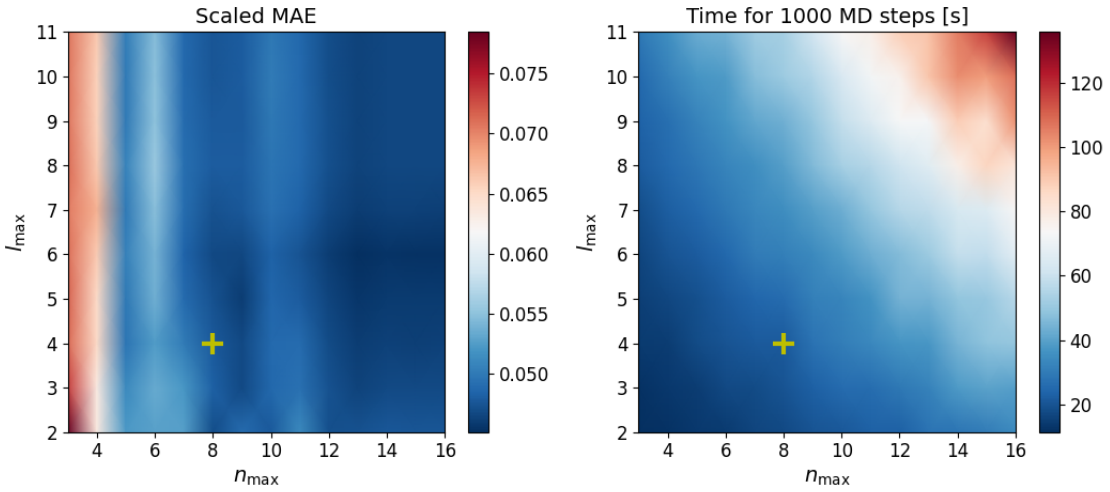

Fig. 4.8: *Scaled MAE of energy and forces as a function of the truncation parameters $n_{max} = 15$ and $l_{max} = 10$ as obtained from a four-fold cross-validation (left) and average computational costs as taken from a 5000 steps MD simulation of the metal-rich (101) IrO_2 surface (right).[188] Large values of n_{max} and l_{max} yield no benefit in accuracy but significantly increased computational cost thus we select $n_{max} = 8$ and $l_{max} = 4$ (indicated by the yellow cross).*

Tab. 4.1: *IrO_2 GAP hyperparameters employed in the two publications associated with this thesis and summarized in section 5.*

	r_{cut} [Å]	θ_{2B} [Å]	δ_{2B} [eV]	M_{2b}	θ_{MB} [Å]	n_{max}	l_{max}	δ_{MB} [eV]	M_{MB}	σ_ε [eV]	σ_f [eV/Å]
[1]	5.5	1.0	1.0	20	0.5	10	3	0.1	1000	0.01	0.1
[2]	5.0	1.0	0.362	25	0.6	8	4	0.1	2000	0.001	0.01

4.3.5 Hyperparameters - How crucial are they? A personal note.

Throughout my PhD I applied several different sets of hyperparameters. Naturally, in the beginning I was choosing hyperparameters based on chemical intuition and some superficial tests and then gradually implemented more and more systematic selection criteria. Yet when focused on finding new surface structures and extending the training set the hyperparameters had to be fixed - for better or worse. In table 4.1 the two most important sets of IrO_2 hyperparameters, viz. the ones applied in my two publications are reported.

The hyperparameters from the first publications have been mostly obtained via cross-validation based on an omnium gatherum of various structures assembled in the first period of my ML journey and a decent amount of chemical intuition due to a rather limited number of publications covering this topic back then. Even with this improvable selection process we identified multiple novel, low-energy IrO_2 surface complexions.[1]

Nonetheless, it was our concern to provide a guideline for a more methodological and systematic hyperparameter selection in the second publication and the above discussed multi-step process reflects this efforts. At first glance the hyperparameters might look similar, however especially the differences in regularization (σ_ε,σ_f) and two-body scaling δ_{2B} are non-negligible. Since adapting

a smaller regularization and an increased focus on the SOAP contribution the second set of hyperparameters leads to a much more flexible potential and thus higher accuracy w.r.t. to the training data. As a potential downside of this high flexibility/accuracy though many of the minimum structures determined via preliminary GAPs were not confirmed as minimum by the subsequent DFT calculation indicating a larger discrepancy between GAP and DFT PES outside the configuration space covered by the training set.

That said, after iteratively converging the training set both hyperparameter sets identified *exactly* the same low-energy surface structures (compare [2] for the convergence protocol). To be quite frank, this was a relief since a distinct output that can only be achieved by a very specific combination of hyperparameters, should be treated very carefully. From my perspective, analyzing the influence of hyperparameters in general is inevitable - regardless of the actual ML method. Yet this hyperparameter analysis should be aiming on avoiding artificial results and identifying plateaus in the parameter space, instead of focusing on finding the absolute optimum.

5 Publications

As this thesis is publication based, in this chapter a summary of my two publications that resulted from my research during my PhD period is given. Each overview includes a brief summary of the genesis and its content and is followed by a more detailed elaboration on my personal contribution. The corresponding full articles together with the respective supporting information can be found in the appendix of this thesis.

5.1 IrO_2 Surface Complexions Identified through Machine Learning and Surface Investigations

Jakob Timmermann, Florian Kraushofer, Nikolaus Resch, Peigang Li, Yu Wang, Zhiqiang Mao, Michele Riva, Yonghyuk Lee, Carsten Staacke, Michael Schmid, Christoph Scheurer, Gareth S. Parkinson, Ulrike Diebold and Karsten Reuter
Phys. Rev. Lett. 125, 206101 (2020).
DOI: 10.1103/PhysRevLett.125.206101

Summary: During an initial *ab initio* study of IrO_2 nanoparticles and surfaces, it quickly became obvious that relevant insights considering the catalytic surface demand a method multiple orders of magnitude faster than DFT. As classical force fields in this case are insufficient due to their lack of reactivity we turned to the Gaussian Approximation Potential (GAP) framework as a reactive, interatomic Machine Learning (ML) potential. At that time no GAP for a multi-component solid material other than $Ge_2Sb_2Te_5$[189] has been published yet. Accordingly, we had to develop our own method: a generation-based GAP training protocol to adequately sample the configuration space and identify global minima for a set of IrO_2 surface structures. In this protocol an initial training set including bulk, surface and nanoparticle structures available from previous studies is extended within each generation, successively refining the associated GAP. To this end the current GAP is used to run simulated annealing (SA) simulations of all low-index surface structures providing a pool of new structures. From this pool of structures a varying number of candidates is selected via visual inspection for consecutive DFT calculations. The new DFT data is then integrated in the training set for the next generation. Over five generations we identified, i.a. four novel, low-energy complexions for metal-rich IrO_2 surfaces that significantly alter the surface free energy phase diagram and predicted the (101) to be the predominant surface at low oxygen potentials. Our structure prediction was then validated together with the chair of Prof. Ulrike Diebold at the Technical University Vienna by multiple experiments and additional calculations: Low-energy electron diffraction images of IrO_2 single crystals exposing solely (101)-type surfaces confirm a (1×1) surface unit cell size hence ruling out any reconstruction of higher symmetry. Scanning-tunneling microscopy images show a zigzag pattern that matches the surface oxygen sites of the (101) complexion. Finally, x-ray photoelectron spectroscopy displays a shift in the binding-energy of surface iridium (compared to bulk iridium) that is in perfect agreement with our initial-state calculations of the respective DFT Kohn-Sham orbitals.

Individual Contributions: After realizing that a shift away from pure DFT calculations towards a faster yet reactive method was inevitable, Christoph Scheurer and Karsten Reuter introduced me to the GAP model. Fruitful discussion with Carsten Staacke helped me to understand the theory and select a first set of hyperparameters. Already the first SA simulations based on the initial GAP revealed several unknown GAP minimum structures and subsequent DFT calculations confirmed that one of them - the metal-rich (101) structure - also constituted a new, unknown DFT minimum. I quickly realized that the GAP could be significantly improved by including the new structures in a training set for a consecutive GAP training. This way the generation-based learning approach was conceived. Within the following generations, I manually selected candidates based on visual comparison to available training structures. I further recalculated all, and confirmed some of the complexions for RuO_2 and carried out the calculations necessary for interpreting the XPS spectrum. The manuscript was jointly written and edited by all authors.

5.2 Data-Efficient Iterative Training of Gaussian Approximation Potentials: Application to Surface Structure Determination of Rutile IrO_2 and RuO_2

Jakob Timmermann, Yonghyuk Lee, Carsten Staacke, Johannes T. Margraf, Christoph Scheurer and Karsten Reuter
J. Chem. Phys. .
DOI: 10.1063/5.0071249

Summary: Despite its instant success the generation-based training protocol as summarized above had an obvious flaw: the selection process via visual inspection is time-consuming, highly subjective, and can not be automated. Accordingly, we introduced a similarity measure as a systematic, quantifiable selection criterion into our workflow and developed an updated iterative and automated training protocol for the identification of global minimum structures of arbitrary metal oxide surfaces. After each SA simulation the similarity of the final GAP minimum structure and the respective training structures is measured based on the associated atomic environments via the SOAP kernel distance. If the kernel distance surpasses a material specific threshold the GAP minimum structure is classified as unknown and automatically selected for a consecutive DFT calculation. Starting from an initial training set the GAP is refined via iteration of SA simulations, DFT calculations and retraining until no further unknown GAP minimum structures are obtained via SA runs. We further present a systematic yet data-efficient scheme for bootstrapping the initial training set, detailed heuristics on how to test and select appropriate hyperparameters, and a straight-forward approach to determine the similarity threshold. This fully-automatized, iterative training protocol is then applied to IrO_2 and RuO_2 and reveals additional low-energy complexions for both materials. Our workflow can further be extended to different systems and is easily adapted, e.g. by substituting SA by any alternative sampling method.

Individual Contributions: Already in the final generations of the first publication the identification of novel structures via visual inspection became tiresome and increasingly prone to human error. Accordingly, determining a fast and strictly reproducible selection process that would also allow for automation was my priority after the general training concept had proven itself as such. Measuring structural changes via the SOAP kernel distance to me seemed and still seems like the most promising and logic solution considering the GAP framework, which does not provide any intrinsic uncertainty measurement. I tested and integrated the similarity measure into our workflow together with several subtleties necessary for a fully automated roll out such as a simple approach to determine the material specific similarity threshold within the first generation. Finally, Yonghyuk and I developed a systematic testing suite for the hyperparameter selection as outlined in full detail in chapter 4.3 and applied the final workflow to IrO_2 and RuO_2. The manuscript was jointly written and edited by all authors.

6 Summary, Conclusions and Outlook

Hydrogen gas obtained from on-site water electrolysis coupled to renewable sources will be a cornerstone of the future, decentralized energy landscape as a clean, versatile and storable energy carrier and bulk chemical. Proton Exchange Membrane and Alkaline electrolyzers are to date the only two setups that are assumed to meet industrial requirements and challenge the currently cheaper and thus predominant steam reforming. Although the PEM cell offers some essential advantages over the Alkaline Electrolyzer such as higher power density and pressure and a more compact stack design, the roll-out at industrial scale is a long time coming. This is mainly due to the harsh, corrosive operating conditions, especially at the anode side, and the hence very limited number of potential catalysts. Effectively IrO_2 is still the only stable catalytic material. However, the very low abundance of iridium demands a metal loading reduction of at least one order of magnitude. To achieve such an increase in performance it is beneficial if not indispensable to gain knowledge of the atomic processes and structures involved in oxygen evolution reaction (OER) at the anode. Yet due to experimental (and computational) restrictions this knowledge is still very limited. Among other things, the actual surface morphologies of the individual facets of catalyst-particles have not been conclusively identified preventing the further analysis of potential active centers. DFT calculations have proven to constitute a powerful tool considering the classification of different surface morphologies, but ultimately have to capitulate given the sheer number of calculations required by global optimization techniques. In recent years, there is increasing evidence that Machine Learning (ML) methods might close exactly this gap, as they provide (almost) DFT-accuracy at a fraction of the costs.

Even though this thesis was not intended to evolved around an ML application, the challenges of a global optimization of a set of surface structures almost inevitably led me to consider ML methods that were emerging at the time. Already the tentative steps indicated the great potential of combining the advantages of ML and DFT methods. The first version of our iterative training protocol - still heavily human supervised - revealed multiple unknown surface morphologies, so-called complexions, that have been experimentally validated by our collaborators in Vienna and reported in a joint publication[1]. A fully automated, data-efficient, iterative training protocol for structure identification via simulated annealing was then presented in the second publication[2]. To be frank, the seemingly effortless identification of new structures based on such a lean, simplistic protocol came as a surprise to me. While this partially can be attributed to material specifics such as a high locality and clearly defined PES minima, these findings would have not been possible without the GAP ML method.

Very sceptical w.r.t. ML methods at first, I quickly put aside my reservations and realized that ML potentials provide two key advantages I have always craved for when working with classical force fields: reactivity and seamless integration of new data. The constant expansion of my practical experience (and eventually also updating my theoretical knowledge) left me no choice but to recognize that ML potentials open up possibilities in computational chemistry, so far unheard of. That *does not* mean that ML methods are a panacea and transfer without further ado and without restriction to all major challenges in chemistry. Just on the contrary, we are still getting to know

what ML methods are capable off - and what not. Relentless analysis and, if necessary, tedious adjustments of new ML potentials should remain a main driver in this field of research. For me personally it was of immense importance to discover that different hyperparameters still lead to the identification of exactly the same low-energy complexions in our iterative training protocol. This was a substantial boost for my confidence in Machine Learning as it basically confirms that ML potentials reflect the underlying physics over a broad range of hyperparameters. Obviously, the frequent evaluation of the GAP minimum structures via DFT calculations within the iterative training protocol serves as built-in validation. Eventually though, the system size will exceed the DFT limit and new validation respectively evaluation schemes have to be applied.

I hope that my work helped to lay the foundation for further research considering the OER on IrO_2 and RuO_2 surfaces. Two topics in particular, come to my mind: developing a GAP training protocol for a metal-water interface or sampling the actual OER on selected surfaces, e.g. via nudged elastic band simulations based on a specifically tailored GAP. Running excessive simulations of nanoparticles in aqueous solution with a highly accurate, reactive and flexible potential or extracting a complex reaction mechanism on a variety of different catalytic surfaces - two things that seemed utopian at the beginning of my scientific studies less than 10 years ago, are now not far from becoming reality. I guess, therein lies the magic of science.

Danksagung

Mein erster Dank gilt meinen Doktorvater Prof. Karsten Reuter ohne den diese Arbeit nicht möglich gewesen wäre und der mir sowohl mit wissenschaftlichem als auch strategischem Rat sowie auf diversen Wies'n Besuchen und Konferenzfeiern zur Seite gestanden ist.

Direkt danach möchte ich Dr. Christoph Scheurer danken, der schon seit meinem ersten Semester entscheidend Anteil an meiner wissenschaftlichen, philosophischen und menschlichen Ausbildung trägt. So erinnere ich mich immer gerne an die ersten kurzen Gespräche in den Pausen der Vorlesung Mathematische Methoden der Chemie I. Zu diesem Zeitpunkt konnte noch niemand ahnen, dass er Jahre später meine Bachelor-, Master- und schließlich auch Doktorarbeit betreuen würde, wobei regelmäßige Gespräche abseits der Chemie (z.B. über Ernst Cassirer) ein fester Bestandteil dieser Betreuung sind und waren.

Aus den ersten Semestern meines Studiums soll Markus Sinnstein nicht unerwähnt bleiben, der mich als Übungsleiter durch seine ruhige, systematische Art stark beeinflusst hat und mir stets als Vorbild galt, wann immer ich in späteren Semestern selbst Übungen abgehalten habe. Hinsichtlich meiner Masterarbeit gebührt mein aufrichtiger Dank David: ich erinnere mich noch genau daran, wie wir uns zusammen die Arbeit von Stern und Fellar erarbeitet haben (die ich hier noch einmal explizit zitieren will [190]) und freue mich über jedes Update zu deiner Arbeit.

In den letzten Jahren habe ich gelernt, dass Forschung nur möglich ist, wenn man von Menschen umgeben ist, bei denen man mit kleinen und größeren Problemen ein offenes Ohr findet. So war das Erste-Hilfe und Admin Team vom ersten Tag immer dann zur Stelle, wenn mein Computer mal wieder nicht so wollte wie ich: vielen Dank Martin, Simon, Simeon, Xhristoph, xhristoph, Matthias, David und Steffen. Gleiches gilt für die ML-GAP Crew: Hannes, Simon, Sina Stocker und Carsten, mit denen zusammen das neue Thema seinen Schrecken schnell verloren hat. Schließlich hätte und würde ich jedes Jahr mehrere Deadlines verpassen, wären da nicht Ruth und nun Julia. Ich danke beiden dafür mich bei jedem bürokratischem Kraftakt zu unterstützen.

Fast fünf Jahre Forschung sind jedoch auch nur dann durchzuhalten, wenn aus Kollegen Freunde werden mit denen man nach (und manchmal während) der Arbeitszeit singen, lachen, quatschen und bis spät nachts zusammensitzen kann. Hier fallen mir zuallererst die sechs grandiosen Gruppenworkshops ein, wofür ich an dieser Stelle den jeweiligen Organisatoren (Mitch, Cristina, David, Sina, Carsten, Thorben) noch einmal das größte Lob aussprechen will. Genauso grandios waren die Aprés-Workshop Trips nach Neapel (Motto: Buongiorno Napoli) und Amsterdam (Motto: Rotlichtbezirk) zusammen mit Sina, Marta, Cri, Chiara, Hanna, Matthias, Mitch, Carsten, David, Patrick, Christian und Simi. Durch zahlreiche DPG Tagungen, gemeinsame Wies'n und Eishockeyspiel Besuche, Segelturns, Weihnachtsfeiern und unglaublich leckere International Food Evenings wurde es auch sonst am Lehrstuhl nie langweilig. In Erinnerung bleiben wird mir u.a. ein Dresdner Karaoke Abend mit Chiara und Hendrick, Käsefonduerühren mit Ahad und Schneebiesln mit Nico. Enormen Spaß hat mir auch die Entwicklung des Crystal Math Spiels gemacht, an dem Harald, Daniel, Simiam, Simone und ich zwei Wochen intensiv gefeilt haben. Ein gemeinsamer Sisyphosbesuch hat mir außerdem gezeigt, dass ich mir um das Party-Vermächtnis des Lehrstuhls keine Sorge machen muss; Coco, Thorben, Sina Z. und Alexandra - keep it up!

Natürlich danke ich meinen beiden Safari-Büro Mitstreitern: Cristina u.a. für die Pasta und Christian für alle unsere Erlebnissen und Gespräche seit dem Semperoperbesuch. Des Weiteren danke ich Mr. Isar/Spree Funk Session himself, Simiam Ghan für seine Akkordeon- und Klavierbegleitung und für seine wundervolle und inspirierende Neugierde und Kreativität sowie meinem Fitness-Compadre Carsten u.a. dafür, das wir beide jetzt in einer der besten Bars Münchens als Pilsdoktoren bekannt und verewigt sind. Mein Dank gilt auch Yonghyuk, der meine manchmal (zu) hastige Arbeitsweise durch seine Akribie ausgeglichen hat und mir in so manch frustrierende Stunde beigestanden ist, Sina Stegmaier, Hanna und Frederic für all die netten Küchengespräche, sei es in Berlin oder München und Wenbin für den trockensten Humor der Welt.

Selbstverständlich will ich hier auch der Deutsche Bundesstiftung Umwelt für ihre - über das Finanzielle hinausgehende - Unterstützung und im Speziellen meinem Betreuer Dr. Christian Schaefer und Sabine Dannhauer danken. Jedes der drei DBU Seminare war (exklusive des Essens) ein absolutes Highlight für mich. An dieser Stelle möchte ich mich auch bei Thorben und Peter, zwei Stipendiatskollegen für Joggingrunden, Fußballabende und eine tolle Bergwanderung bedanken.

Wer mich kennt, weiß, dass sich mein Leben in den letzten fünf Jahren nicht ausschließlich am Lehrstuhl abgespielt hat und dass Freunde doch das Schönste auf dieser Welt sind. Daher danke ich den Schnabuletti Jungs (Baba, Febo, Knaui, Lenz, Manu, Mathe, Memo, Moritz und Valt) für die unglaublich herzliche Gemeinschaft, die schon fast jahrzehntelange Freundschaft und einen Chatverlauf der weltweit wohl seinesgleichen sucht. Was als Berlinbesuch begann, hat sich durch gemeinsame Tage und Nächte, Urlaube sowie Hummer & Champagner Abende längst verselbstständigt. Genauso danke ich der S.F.C. (Grisi, Flo, Ferdi, Samir, Vally, Niggl, Gil und noch einmal Mathe und Memo) für Freundschaft die bis auf die Schulbank, bis zu den ersten Flauchernächten und Maratbesuchen zurückreicht. Leipzig und Wien bleiben! Ich danke den alten und neuen, Münchner-, Berliner-, Wiener-, Musiker-, Sportler- und Kneipenfreunden: Sarah und den Baadergirls, Julieta, der Slowakei-Crew, Phil und Manu, Alex, Sven und Rico, den Barcuzzi-Jungs Wiede und Olli, Petra & Michi, Jo und Ruppi sowie meinen beiden Patenkindern Lotta und Carlo. Mein spezieller Dank für die gemeinsam geschriebenen Songs und Musikvideos, den riesigen kreativen Input und all die damit verbundenen schönen Stunden gilt Riotlee. Dr. Martin und Knaui danke ich für die feinsten Küchenparties, immer neue Musik und eine dermaßen herzliche Gastfreundschaft.

Unendlicher Dank gilt meiner Heimatstadt München, für die ruhige Unterstützung in all den Jahren und selbstverständlich auch Berlin, dieser aufregenden, lauten, wilden Stadt und ihren zahlreichen Kneipen, namentlich Franken, Schumanns, Maroto, Geyerwally, Pilsdoktor und Elefant.

Selbstverständlich danke ich auch den vier Freunden, die mich von Anfang an auf dieser, mal zielstrebigen, mal irrlichtenden (Studiums)Reise begleiten haben: Manu (El Presidente), Basti, Lenz und Sevi und damit dem Boyz-n-the hood Club - ihr wisst's ja eh. Tausend Dank.

Mein tiefster Dank gilt schließlich den vier Menschen, die mich schon viel länger auf der Reise namens Leben begleiten: meinen beiden Schwestern Annette und Clara und meinen Eltern.

Und zu guter Letzt: Danke Joya ♥

Rockin' steady - München, November, 2021

Bibliography

[1] J. Timmermann, F. Kraushofer, N. Resch, P. Li, Y. Wang, Z. Mao, M. Riva, Y. Lee, C. Staacke, M. Schmid, C. Scheurer, G. S. Parkinson, U. Diebold, and K. Reuter, Phys. Rev. Lett. **125**, 206101 (2020) (cit. on pp. i, 2, 24, 27, 40, 47).

[2] J. C. Timmermann, Y. Lee, C. G. Staacke, J. T. Margraf, C. Scheurer, and K. Reuter, J. Chem. Phys **155**, 244107 (2021) (cit. on pp. i, 2, 24, 26, 27, 35, 38–41, 47).

[3] S. B. Destatis/StBA, *Datenreport 2021 - kapitel 13: umwelt, energie und mobilität*, (2021) `https://www.destatis.de/DE/Service/Statistik-Campus/Datenreport/Downloads/datenreport-2021-kap-13.html` (visited on 2021-10-01) (cit. on p. 1).

[4] M. Carmo, D. L. Fritz, J. Mergel, and D. Stolten, Int. J. Hydrog. **38**, 4901 (2013) (cit. on pp. 1, 6, 8–12).

[5] D. Parra, M. Swierczynski, D. I. Stroe, S. Norman, A. Abdon, J. Worlitschek, T. O'Doherty, L. Rodrigues, M. Gillott, X. Zhang, C. Bauer, and M. K. Patel, Renew. Sustain. Energy Rev. **79**, 730 (2017) (cit. on p. 1).

[6] K. Ayers, N. Danilovic, R. Ouimet, M. Carmo, B. Pivovar, and M. Bornstein, Annu. Rev. Chem. Biomol. Eng. **10**, 219 (2019) (cit. on pp. 1, 6, 9–12).

[7] S. Chu, Y. Cui, and N. Liu, Nat. Mater. **16**, 16 (2017) (cit. on p. 1).

[8] T. M. Gür, Energy Environ. Sci. **11**, 2696 (2018) (cit. on p. 1).

[9] T. Mahlia, T. Saktisahdan, A. Jannifar, M. Hasan, and H. Matseelar, Renew. Sustain. Energy Rev. **33**, 532 (2014) (cit. on p. 1).

[10] F. Ausfelder and A. Bazzanella, "Hydrogen in the chemical industry," in *Hydrogen science and engineering : materials, processes, systems and technology* (John Wiley & Sons, Ltd, 2016) Chap. 2, pp. 19–40 (cit. on p. 1).

[11] M. Schalenbach, G. Tjarks, M. Carmo, W. Lueke, M. Mueller, and D. Stolten, J. Electrochem. Soc. **163**, F3197 (2016) (cit. on pp. 1, 8, 10).

[12] M. David, C. Ocampo-Martínez, and R. Sánchez-Peña, J. Energy Storage **23**, 392 (2019) (cit. on pp. 1, 8).

[13] J. Brauns and T. Turek, Processes **8**, `10.3390/pr8020248` (2020) (cit. on pp. 1, 9).

[14] J. Rossmeisl, A. Logadottir, and J. Nørskov, Chem. Phys. **319**, 178 (2005) (cit. on pp. 1, 15, 16).

[15] J. Rossmeisl, Z.-W. Qu, H. Zhu, G.-J. Kroes, and J. Nørskov, J. Electroanal. Chem. **607**, 83 (2007) (cit. on pp. 1, 6, 15, 16, 24).

[16] M. Bernt, A. Siebel, and H. A. Gasteiger, J. Electrochem. Soc. **165**, F305 (2018) (cit. on pp. 1, 6, 11).

[17] C. C. L. McCrory, S. Jung, J. C. Peters, and T. F. Jaramillo, J. Am. Chem. Soc. **135**, 16977 (2013) (cit. on pp. 1, 8).

[18] T. Reier, M. Oezaslan, and P. Strasser, ACS Catal. **2**, 1765 (2012) (cit. on p. 1).

[19] S. Cherevko, A. R. Zeradjanin, A. A. Topalov, N. Kulyk, I. Katsounaros, and K. J. J. Mayrhofer, ChemCatChem **6**, 2219 (2014) (cit. on pp. 1, 11).

[20] S. Cherevko, S. Geiger, O. Kasian, N. Kulyk, J.-P. Grote, A. Savan, B. R. Shrestha, S. Merzlikin, B. Breitbach, A. Ludwig, and K. J. Mayrhofer, Catalysis Today **262**, 170 (2016) (cit. on pp. 1, 11, 14).

[21] N. Danilovic, R. Subbaraman, K.-C. Chang, S. H. Chang, Y. J. Kang, J. Snyder, A. P. Paulikas, D. Strmcnik, Y.-T. Kim, D. Myers, V. R. Stamenkovic, and N. M. Markovic, J. Phys. Chem. Lett. **5**, 2474 (2014) (cit. on pp. 1, 11, 14).

[22] C. Spöri, J. T. H. Kwan, A. Bonakdarpour, D. P. Wilkinson, and P. Strasser, Angew. Chem. **56**, 5994 (2017) (cit. on p. 1).

[23] H. Over, ACS Catal. **0**, 8848 (2021) (cit. on pp. 1, 2, 11, 14, 16, 17).

[24] K. Chen, R. J. Walker, R. L. Rudnick, S. Gao, R. M. Gaschnig, I. S. Puchtel, M. Tang, and Z.-C. Hu, Geochim. Cosmochim. Acta **191**, 1 (2016) (cit. on p. 1).

[25] U. Babic, M. Suermann, F. N. Büchi, L. Gubler, and T. J. Schmidt, J. Electrochem. Soc. **164**, F387 (2017) (cit. on pp. 1, 6, 12).

[26] M. Bernt, A. Hartig-Weiß, M. F. Tovini, H. A. El-Sayed, C. Schramm, J. Schröter, C. Gebauer, and H. A. Gasteiger, Chem. Ing. Tech. **92**, 31 (2020) (cit. on pp. 1, 6, 12).

[27] C. Minke, M. Suermann, B. Bensmann, and R. Hanke-Rauschenbach, Int. J. Hydrog. **46**, 23581 (2021) (cit. on pp. 1, 12).

[28] Y. Lee, J. Suntivich, K. c. r. J. May, E. E. Perry, and Y. Shao-Horn, J. Phys. Chem. Lett. **3**, 399 (2012) (cit. on pp. 1, 11, 12).

[29] P. Lettenmeier, J. Majchel, L. Wang, V. A. Saveleva, S. Zafeiratos, E. R. Savinova, J.-J. Gallet, F. Bournel, A. S. Gago, and K. A. Friedrich, Chem. Sci. **9**, 3570 (2018) (cit. on pp. 1, 12).

[30] T. Binninger, E. Fabbri, A. Patru, M. Garganourakis, J. Han, D. F. Abbott, O. Sereda, R. Kötz, A. Menzel, M. Nachtegaal, and T. J. Schmidt, J. Electrochem. Soc. **163**, H906 (2016) (cit. on pp. 1, 13, 14).

[31] E. Oakton, D. Lebedev, M. Povia, D. F. Abbott, E. Fabbri, A. Fedorov, M. Nachtegaal, C. Copéret, and T. J. Schmidt, ACS Catal. **7**, 2346 (2017) (cit. on pp. 1, 13).

[32] Y. Pi, Q. Shao, P. Wang, J. Guo, and X. Huang, Adv. Funct. Mater. **27**, 1700886 (2017) (cit. on pp. 1, 13).

[33] C. Ma, W. Sun, W. Qamar Zaman, Z. Zhou, H. Zhang, Q. Shen, L. Cao, and J. Yang, ACS Appl. Mater. Interfaces **12**, 34980 (2020) (cit. on p. 1).

[34] O. Diaz-Morales, S. Raaijman, R. Kortlever, P. J. Kooyman, T. Wezendonk, J. Gascon, W. T. Fu, and M. T. M. Koper, Nat. Commun. **7**, 12363 (2016) (cit. on pp. 1, 13).

[35] S. T. Hunt, M. Milina, A. C. Alba-Rubio, C. H. Hendon, J. A. Dumesic, and Y. Román-Leshkov, Science **352**, 974 (2016) (cit. on pp. 1, 13).

[36] H. N. Nong, L. Gan, E. Willinger, D. Teschner, and P. Strasser, Chem. Sci. **5**, 2955 (2014) (cit. on pp. 1, 13, 16).

[37] B. M. Tackett, W. Sheng, S. Kattel, S. Yao, B. Yan, K. A. Kuttiyiel, Q. Wu, and J. G. Chen, ACS Catal. **8**, 2615 (2018) (cit. on pp. 1, 13, 24).

[38] C. V. Pham, M. Bühler, J. Knöppel, M. Bierling, D. Seeberger, D. Escalera-López, K. J. Mayrhofer, S. Cherevko, and S. Thiele, Appl. Catal. B **269**, 118762 (2020) (cit. on pp. 1, 13).

[39] T. Reier, H. N. Nong, D. Teschner, R. Schlögl, and P. Strasser, Adv. Energy Mater. **7**, 1601275 (2017) (cit. on pp. 1, 11, 14, 16, 17).

[40] K. A. Stoerzinger, L. Qiao, M. D. Biegalski, and Y. Shao-Horn, J. Phys. Chem. Lett. **5**, 1636 (2014) (cit. on pp. 1, 15, 17).

[41] J. A. Gauthier, C. F. Dickens, L. D. Chen, A. D. Doyle, and J. K. Nørskov, J. Phys. Chem. C **121**, 11455 (2017) (cit. on pp. 1, 16, 17).

[42] Y. Ping, R. J. Nielsen, and W. A. Goddard, J. Am. Chem. Soc. **139**, 149 (2017) (cit. on pp. 1, 15–17, 24).

[43] D. Opalka, C. Scheurer, and K. Reuter, ACS Catal. **9**, 4944 (2019) (cit. on pp. 1, 17, 24).

[44] M. G. Mavros, T. Tsuchimochi, T. Kowalczyk, A. McIsaac, L.-P. Wang, and T. V. Voorhis, Inorg. Chem. **53**, 6386 (2014) (cit. on pp. 1, 16).

[45] K. S. Exner and H. Over, ACS Catal. **9**, 6755 (2019) (cit. on pp. 1, 15, 17).

[46] Y. Yang, Y. Xiong, R. Zeng, X. Lu, M. Krumov, X. Huang, W. Xu, H. Wang, F. J. DiSalvo, J. D. Brock, D. A. Muller, and H. D. Abruña, ACS Catal. **11**, 1136 (2021) (cit. on pp. 2, 14).

[47] F. G. Sen, A. Kinaci, B. Narayanan, S. K. Gray, M. J. Davis, S. K. R. S. Sankaranarayanan, and M. K. Y. Chan, J. Mater. Chem. A **3**, 18970 (2015) (cit. on pp. 2, 26).

[48] A. K. Rappe and W. A. Goddard, J. Phys. Chem. **95**, 3358 (1991) (cit. on p. 2).

[49] P. M. Morse, Phys. Rev. **34**, 57 (1929) (cit. on pp. 2, 26).

[50] J. Behler and M. Parrinello, Phys. Rev. Lett. **98**, 146401 (2007) (cit. on p. 2).

[51] J. Behler, Int. J. Quantum Chem. **115**, 1032 (2015) (cit. on p. 2).

[52] A. P. Bartók, M. C. Payne, R. Kondor, and G. Csányi, Phys. Rev. Lett. **104**, 136403 (2010) (cit. on p. 2).

[53] A. P. Bartók, R. Kondor, and G. Csányi, Phys. Rev. B **87**, 184115 (2013) (cit. on p. 2).

[54] V. L. Deringer, A. P. Bartók, N. Bernstein, D. M. Wilkins, M. Ceriotti, and G. Csányi, Chem. Rev. **121**, 10073 (2021) (cit. on pp. 2, 27, 30, 32, 33, 39).

[55] A. P. Bartók, S. De, C. Poelking, N. Bernstein, J. R. Kermode, G. Csányi, and M. Ceriotti, Sci. Adv. **3**, e1701816 (2017) (cit. on pp. 2, 27).

[56] A. P. Bartók, J. Kermode, N. Bernstein, and G. Csányi, Phys. Rev. X **8**, 041048 (2018) (cit. on pp. 2, 27).

[57] D. Dragoni, T. D. Daff, G. Csányi, and N. Marzari, Phys. Rev. Materials **2**, 013808 (2018) (cit. on pp. 2, 27).

[58] P. Gkeka, G. Stoltz, A. Barati Farimani, Z. Belkacemi, M. Ceriotti, J. D. Chodera, A. R. Dinner, A. L. Ferguson, J.-B. Maillet, H. Minoux, C. Peter, F. Pietrucci, A. Silveira, A. Tkatchenko, Z. Trstanova, R. Wiewiora, and T. Lelièvre, J. Chem. Theory Comput. **16**, 4757 (2020) (cit. on pp. 2, 27).

[59] P. Rowe, V. L. Deringer, P. Gasparotto, G. Csányi, and A. Michaelides, J. Chem. Phys **153**, 034702 (2020) (cit. on pp. 2, 27).

[60] R. Jinnouchi, K. Miwa, F. Karsai, G. Kresse, and R. Asahi, J. Phys. Chem. Lett. **11**, 6946 (2020) (cit. on pp. 2, 27).

[61] J. Vandermause, S. B. Torrisi, S. Batzner, Y. Xie, L. Sun, A. M. Kolpak, and B. Kozinsky, Npj Comput. Mater. **6**, 20 (2020) (cit. on pp. 2, 27).

[62] M. K. Bisbo and B. Hammer, *Global optimization of atomistic structure enhanced by machine learning*, 2020 (cit. on pp. 2, 27).

[63] C. Verdi, F. Karsai, P. Liu, R. Jinnouchi, and G. Kresse, Npj Comput. Mater. **7**, 156 (2021) (cit. on pp. 2, 27).

[64] S. Kaappa, E. G. del Rıo, and K. W. Jacobsen, Phys. Rev. B **103**, 174114 (2021) (cit. on pp. 2, 27).

[65] Y. Xie, J. Vandermause, L. Sun, A. Cepellotti, and B. Kozinsky, Npj Comput. Mater. **7**, 40 (2021) (cit. on pp. 2, 27).

[66] I. Poltavsky and A. Tkatchenko, J. Phys. Chem. Lett. **12**, 6551 (2021) (cit. on pp. 2, 27).

[67] P. Atkins, J. d. Paula, and J. Keeler, *Atkins' Physical Chemistry*, 11th ed (CRC Press LLC, 2017) (cit. on p. 5).

[68] A. R. Zeradjanin, A. A. Topalov, Q. Van Overmeere, S. Cherevko, X. Chen, E. Ventosa, W. Schuhmann, and K. J. J. Mayrhofer, RSC Adv. **4**, 9579 (2014) (cit. on p. 6).

[69] J. K. Nørskov, J. Rossmeisl, A. Logadottir, L. Lindqvist, J. R. Kitchin, T. Bligaard, and H. Jónsson, J. Phys. Chem. B **108**, 17886 (2004) (cit. on p. 6).

[70] T. Bligaard, J. Nørskov, S. Dahl, J. Matthiesen, C. Christensen, and J. Sehested, J. Catal. **224**, 206 (2004) (cit. on p. 6).

[71] J. A. Dumesic, G. W. Huber, and M. Boudart, "Principles of heterogeneous catalysis," in *Handbook of heterogeneous catalysis* (American Cancer Society, 2008) Chap. 1.1 (cit. on p. 6).

[72] D.-Y. Kuo, H. Paik, J. Kloppenburg, B. Faeth, K. M. Shen, D. G. Schlom, G. Hautier, and J. Suntivich, J. Am. Chem. Soc. **140**, 17597 (2018) (cit. on pp. 6, 17).

[73] K. S. Exner, ACS Catal. **9**, 5320 (2019) (cit. on p. 6).

[74] M. Janjua and R. Le Roy, Int. J. Hydrog. **10**, 11 (1985) (cit. on p. 6).

[75] K. Zeng and D. Zhang, Prog. Energy Combust. Sci. **36**, 307 (2010) (cit. on p. 6).

[76] N. Danilovic, R. Subbaraman, D. Strmcnik, V. Stamenkovic, and N. Markovic, J. Serb. Chem. Soc. **78** (2013) (cit. on p. 8).

[77] J. Durst, C. Simon, F. Hasché, and H. A. Gasteiger, **162**, F190 (2014) (cit. on p. 8).

[78] M. Gong, D.-Y. Wang, C.-C. Chen, B.-J. Hwang, and H. Dai, Nano Research **9**, 28 (2016) (cit. on p. 8).

[79] A. Roy, S. Watson, and D. G. Infield, Int. J. Hydrog. **31**, 1964 (2006) (cit. on p. 8).

[80] M. T. de Groot and A. W. Vreman, Electrochim. Acta **369**, 137684 (2021) (cit. on p. 8).

[81] M. Schalenbach, A. Zeradjanin, O. I. Kasian, S. Cherevko, and K. Mayrhofer, Int. J. Electrochem. Sci. **13**, 1173 (2018) (cit. on p. 8).

[82] A. N. Colli, H. H. Girault, and A. Battistel, Materials **12** (2019) (cit. on p. 8).

[83] Y. Li, B. Wei, Z. Yu, O. Bondarchuk, A. Araujo, I. Amorim, N. Zhang, J. Xu, I. C. Neves, and L. Liu, ACS Sustain. Chem. Eng. **8**, 10193 (2020) (cit. on p. 8).

[84] M. Schalenbach, O. Kasian, and K. J. Mayrhofer, Int. J. Hydrog. **43**, 11932 (2018) (cit. on p. 8).

[85] P. Trinke, P. Haug, J. Brauns, B. Bensmann, R. Hanke-Rauschenbach, and T. Turek, J. Electrochem. Soc. **165**, F502 (2018) (cit. on pp. 9, 10).

[86] D. W. Shin, M. D. Guiver, and Y. M. Lee, Chem. Rev. **117**, 4759 (2017) (cit. on p. 9).

[87] M. Bernt and H. A. Gasteiger, J. Electrochem. Soc. **163**, F3179 (2016) (cit. on p. 10).

[88] Z. Xie, S. Yu, G. Yang, K. Li, L. Ding, W. Wang, and F.-Y. Zhang, Int. J. Hydrog. **46**, 1155 (2021) (cit. on p. 10).

[89] H. In Lee, D. T. Dung, J. Kim, J. H. Pak, S. k. Kim, H. S. Cho, W. C. Cho, and C. H. Kim, Int. J. Energy Res. **44**, 1875 (2020) (cit. on p. 10).

[90] F. Bauer, S. Denneler, and M. Willert-Porada, J. Polym. Sci. B Polym. Phys. **43**, 786 (2005) (cit. on p. 10).

[91] D. R. Lide, *CRC Handbook of Chemistry and Physics*, 84th ed (CRC Press LLC, 2003) (cit. on p. 10).

[92] T. L. Doan, H. E. Lee, S. S. H. Shah, M. Kim, C.-H. Kim, H.-S. Cho, and T. Kim, Int. J. Energy Res. **45**, 14207 (2021) (cit. on pp. 10, 11).

[93] C. Liu, M. Carmo, G. Bender, A. Everwand, T. Lickert, J. L. Young, T. Smolinka, D. Stolten, and W. Lehnert, Electrochem. commun. **97**, 96 (2018) (cit. on p. 11).

[94] A. Buttler and H. Spliethoff, Renew. Sustain. Energy Rev. **82**, 2440 (2018) (cit. on p. 11).

[95] S. Sun, Z. Shao, H. Yu, G. Li, and B. Yi, J. Power Sources **267**, 515 (2014) (cit. on p. 11).

[96] C. Rakousky, U. Reimer, K. Wippermann, M. Carmo, W. Lueke, and D. Stolten, J. Power Sources **326**, 120 (2016) (cit. on p. 11).

[97] R. Frydendal, E. A. Paoli, B. P. Knudsen, B. Wickman, P. Malacrida, I. E. L. Stephens, and I. Chorkendorff, ChemElectroChem **1**, 2075 (2014) (cit. on p. 11).

[98] C. C. Pavel, F. Cecconi, C. Emiliani, S. Santiccioli, A. Scaffidi, S. Catanorchi, and M. Comotti, Angew. Chem. **53**, 1378 (2014) (cit. on p. 11).

[99] K. S. Joya and H. J. de Groot, Int. J. Hydrog. **37**, 8787 (2012) (cit. on p. 11).

[100] H. Ito, N. Kawaguchi, S. Someya, and T. Munakata, Electrochim. Acta **297**, 188 (2019) (cit. on p. 11).

[101] P. Fortin, T. Khoza, X. Cao, S. Y. Martinsen, A. Oyarce Barnett, and S. Holdcroft, J. Power Sources **451**, 227814 (2020) (cit. on p. 11).

[102] I. Vincent and D. Bessarabov, Renew. Sustain. Energy Rev. **81**, 1690 (2018) (cit. on p. 11).

[103] H. A. Miller, K. Bouzek, J. Hnat, S. Loos, C. I. Bernäcker, T. Weißgärber, L. Röntzsch, and J. Meier-Haack, Sustain. Energy Fuels **4**, 2114 (2020) (cit. on p. 11).

[104] L. D. Burke and T. O. O'Meara, J. Chem. Soc., Faraday Trans. 1 **68**, 839 (1972) (cit. on p. 11).

[105] S. Trasatti and G. Buzzanca, J. Electroanal. Chem. Interfacial Electrochem. **29**, A1 (1971) (cit. on p. 11).

[106] A. T. Mayyas, M. F. Ruth, B. S. Pivovar, G. Bender, and K. B. Wipke, **1**, 10.2172/1557965 (2019) (cit. on p. 12).

[107] J. S. Mondschein, J. F. Callejas, C. G. Read, J. Y. C. Chen, C. F. Holder, C. K. Badding, and R. E. Schaak, Chemistry of Materials **29**, 950 (2017) (cit. on p. 12).

[108] M. Huynh, T. Ozel, C. Liu, E. C. Lau, and D. G. Nocera, Chem. Sci. **8**, 4779 (2017) (cit. on p. 12).

[109] P. Cai, J. Huang, J. Chen, and Z. Wen, Angew. Chem. **56**, 4858 (2017) (cit. on p. 12).

[110] P. He, X.-Y. Yu, and X. W. (Lou, Angew. Chem. **56**, 3897 (2017) (cit. on p. 12).

[111] Z.-P. Wu, X. F. Lu, S.-Q. Zang, and X. W. (Lou, Adv. Funct. Mater. **30**, 1910274 (2020) (cit. on p. 12).

[112] S. M. Alia, B. Rasimick, C. Ngo, K. C. Neyerlin, S. S. Kocha, S. Pylypenko, H. Xu, and B. S. Pivovar, J. Electrochem. Soc. **163**, F3105 (2016) (cit. on p. 12).

[113] D. Strmcnik, M. Uchimura, C. Wang, R. Subbaraman, N. Danilovic, D. van der Vliet, A. P. Paulikas, V. R. Stamenkovic, and N. M. Markovic, Nat. Chem. **5**, 300 (2013) (cit. on p. 12).

[114] J. Lim, D. Park, S. S. Jeon, C.-W. Roh, J. Choi, D. Yoon, M. Park, H. Jung, and H. Lee, Adv. Funct. Mater. **28**, 1704796 (2018) (cit. on p. 12).

[115] Y. Pi, N. Zhang, S. Guo, J. Guo, and X. Huang, Nano Letters **16**, 4424 (2016) (cit. on p. 12).

[116] D. Chandra, N. Abe, D. Takama, K. Saito, T. Yui, and M. Yagi, ChemSusChem **8**, 795 (2015) (cit. on p. 12).

[117] C. Zhao, H. Yu, Y. Li, X. Li, L. Ding, and L. Fan, J. Electroanal. Chem. **688**, 269 (2013) (cit. on p. 12).

[118] Z.-X. Lu, Y. Shi, P. Gupta, X.-p. Min, H.-y. Tan, Z.-D. Wang, C.-q. Guo, Z.-q. Zou, H. Yang, S. Mukerjee, and C.-F. Yan, Electrochim. Acta **348**, 136302 (2020) (cit. on p. 12).

[119] Y.-T. Kim, P. P. Lopes, S.-A. Park, A.-Y. Lee, J. Lim, H. Lee, S. Back, Y. Jung, N. Danilovic, V. Stamenkovic, J. Erlebacher, J. Snyder, and N. M. Markovic, Nat. Commun. **8**, 1449 (2017) (cit. on p. 13).

[120] M. Tariq, W. Q. Zaman, W. Sun, Z. Zhou, Y. Wu, L.-m. Cao, and J. Yang, ACS Sustain. Chem. Eng. **6**, 4854 (2018) (cit. on p. 13).

[121] J. Xu, J. Li, Z. Lian, A. Araujo, Y. Li, B. Wei, Z. Yu, O. Bondarchuk, I. Amorim, V. Tileli, B. Li, and L. Liu, ACS Catal. **11**, 3402 (2021) (cit. on p. 13).

[122] H. Lv, S. Wang, J. Li, C. Shao, W. Zhou, X. Shen, M. Xue, and C. Zhang, Applied Surf. Sci. **514**, 145943 (2020) (cit. on p. 13).

[123] V. A. Saveleva, L. Wang, W. Luo, S. Zafeiratos, C. Ulhaq-Bouillet, A. S. Gago, K. A. Friedrich, and E. R. Savinova, J. Phys. Chem. Lett. **7**, 3240 (2016) (cit. on p. 13).

[124] C. Roy, R. R. Rao, K. A. Stoerzinger, J. Hwang, J. Rossmeisl, I. Chorkendorff, Y. Shao-Horn, and I. E. L. Stephens, ACS Energy Lett. **3**, 2045 (2018) (cit. on pp. 14, 16–18).

[125] E. Fabbri and T. J. Schmidt, ACS Catal. **8**, 9765 (2018) (cit. on pp. 14, 17).

[126] D. Li, C. Batchelor-McAuley, and R. G. Compton, Appl. Mater. Today **18**, 100404 (2020) (cit. on p. 14).

[127] S. Geiger, O. Kasian, M. Ledendecker, E. Pizzutilo, A. M. Mingers, W. T. Fu, O. Diaz-Morales, Z. Li, T. Oellers, L. Fruchter, A. Ludwig, K. J. J. Mayrhofer, M. T. M. Koper, and S. Cherevko, Nat. Catal. **1**, 508 (2018) (cit. on p. 14).

[128] C. Spöri, P. Briois, H. N. Nong, T. Reier, A. Billard, S. Kühl, D. Teschner, and P. Strasser, ACS Catal. **9**, 6653 (2019) (cit. on p. 14).

[129] J. Suntivich, K. J. May, H. A. Gasteiger, J. B. Goodenough, and Y. Shao-Horn, Science **334**, 1383 (2011) (cit. on p. 14).

[130] J. O. Bockris, J. Chem. Phys **24**, 817 (1956) (cit. on p. 15).

[131] Y.-H. Fang and Z.-P. Liu, J. Am. Chem. Soc. **132**, 18214 (2010) (cit. on pp. 15–17).

[132] P. Castelli, S. Trasatti, F. H. Pollak, and W. E. O'Grady, J. Electroanal. Chem. Interfacial Electrochem. **210**, 189 (1986) (cit. on pp. 15, 17).

[133] R. R. Rao, M. J. Kolb, N. B. Halck, A. F. Pedersen, A. Mehta, H. You, K. A. Stoerzinger, Z. Feng, H. A. Hansen, H. Zhou, L. Giordano, J. Rossmeisl, T. Vegge, I. Chorkendorff, I. E. L. Stephens, and Y. Shao-Horn, Energy Environ. Sci. **10**, 2626 (2017) (cit. on pp. 16, 17).

[134] K. A. Stoerzinger, O. Diaz-Morales, M. Kolb, R. R. Rao, R. Frydendal, L. Qiao, X. R. Wang, N. B. Halck, J. Rossmeisl, H. A. Hansen, T. Vegge, I. E. L. Stephens, M. T. M. Koper, and Y. Shao-Horn, ACS Energy Lett. **2**, 876 (2017) (cit. on pp. 16–18).

[135] R. R. Rao, M. J. Kolb, L. Giordano, A. F. Pedersen, Y. Katayama, J. Hwang, A. Mehta, H. You, J. R. Lunger, H. Zhou, N. B. Halck, T. Vegge, I. Chorkendorff, I. E. L. Stephens, and Y. Shao-Horn, Nat. Catal. **3**, 516 (2020) (cit. on pp. 16, 17).

[136] I. C. Man, H.-Y. Su, F. Calle-Vallejo, H. A. Hansen, J. I. Martínez, N. G. Inoglu, J. Kitchin, T. F. Jaramillo, J. K. Nørskov, and J. Rossmeisl, ChemCatChem **3**, 1159 (2011) (cit. on p. 16).

[137] Z.-J. Zhao, S. Liu, S. Zha, D. Cheng, F. Studt, G. Henkelman, and J. Gong, Nat. Rev. Mater. **4**, 792 (2019) (cit. on p. 16).

[138] K. S. Exner, I. Sohrabnejad-Eskan, and H. Over, ACS Catal. **8**, 1864 (2018) (cit. on pp. 16, 17).

[139] J. A. Gauthier, S. Ringe, C. F. Dickens, A. J. Garza, A. T. Bell, M. Head-Gordon, J. K. Nørskov, and K. Chan, ACS Catal. **9**, 920 (2019) (cit. on p. 16).

[140] D.-Y. Kuo, J. K. Kawasaki, J. N. Nelson, J. Kloppenburg, G. Hautier, K. M. Shen, D. G. Schlom, and J. Suntivich, J. Am. Chem. Soc. **139**, 3473 (2017) (cit. on pp. 16, 17).

[141] A. Groß and S. Sakong, Curr. Opin. Electrochem. **14**, 1 (2019) (cit. on p. 16).

[142] K. S. Exner, ChemCatChem **11**, 3234 (2019) (cit. on p. 17).

[143] G. Novell-Leruth, G. Carchini, and N. López, J. Chem. Phys **138**, 194706 (2013) (cit. on p. 17).

[144] A. Grimaud, O. Diaz-Morales, B. Han, W. T. Hong, Y.-L. Lee, L. Giordano, K. A. Stoerzinger, M. T. M. Koper, and Y. Shao-Horn, Nat. Chem. **9**, 457 (2017) (cit. on p. 17).

[145] S. Fierro, T. Nagel, H. Baltruschat, and C. Comninellis, Electrochem. commun. **9**, 1969 (2007) (cit. on p. 17).

[146] K. Macounova, M. Makarova, and P. Krtil, Electrochem. commun. **11**, 1865 (2009) (cit. on p. 17).

[147] K. Schweinar, B. Gault, I. Mouton, and O. Kasian, J. Phys. Chem. Lett. **11**, 5008 (2020) (cit. on p. 18).

[148] G. A. Somorjai, Annu. Rev. Phys. Chem. **45**, 721 (1994) (cit. on pp. 18, 26).

[149] J. Aßmann, D. Crihan, M. Knapp, E. Lundgren, E. Löffler, M. Muhler, V. Narkhede, H. Over, M. Schmid, A. P. Seitsonen, and P. Varga, Angew. Chem. **44**, 917 (2005) (cit. on pp. 18, 26).

[150] F. Polo-Garzon, Z. Bao, X. Zhang, W. Huang, and Z. Wu, ACS Catal. **9**, 5692 (2019) (cit. on pp. 18, 26).

[151] H. Chen, L. Shi, X. Liang, L. Wang, T. Asefa, and X. Zou, Angew. Chem. **59**, 19654 (2020) (cit. on p. 19).

[152] G. Wulff, *Zur Frage der Geschwindigkeit des Wachsthums und der Auflösung der Krystallflächen*, Vol. 34 (1901), pp. 449–530 (cit. on p. 19).

[153] W. Sun and G. Ceder, Surf. Sci. **669**, 50 (2018) (cit. on p. 19).

[154] J. Mackenzie, A. Moore, and J. Nicholas, J. Phys. Chem. Solids **23**, 185 (1962) (cit. on p. 19).

[155] J. Mackenzie and J. Nicholas, J. Phys. Chem. Solids **23**, 197 (1962) (cit. on p. 19).

[156] H. P. Bonzel and M. Nowicki, Phys. Rev. B **70**, 245430 (2004) (cit. on p. 22).

[157] J. Métois and P. Müller, Surf. Sci. **548**, 13 (2004) (cit. on p. 22).

[158] R. N. Shimizu and N. R. Demarquette, J. Appl. Polym. Sci. **76**, 1831 (2000) (cit. on p. 22).

[159] E. M. Baba, C. E. Cansoy, and E. O. Zayim, Appl. Surf. Sci. **350**, 115 (2015) (cit. on p. 22).

[160] K. Reuter and M. Scheffler, Phys. Rev. B **65**, 035406 (2001) (cit. on p. 22).

[161] K. Reuter, Catal. Lett. **146**, 541 (2016) (cit. on p. 22).

[162] K. K. Irikura, J. Phys. Chem. Ref. Data **36**, 389 (2007) (cit. on p. 23).

[163] J. W. Arblaster, Platin. Met. Rev. **54**, 93 (2010) (cit. on p. 23).

[164] V. Monteseguro, J. A. Sans, V. Cuartero, F. Cova, I. A. Abrikosov, W. Olovsson, C. Popescu, S. Pascarelli, G. Garbarino, H. J. M. Jönsson, T. Irifune, and D. Errandonea, Sci. Rep. **9**, 8940 (2019) (cit. on p. 23).

[165] M. W. Chase, *NIST-JANAF Thermochemical Tables*, 4th ed (AIP, 1998) (cit. on p. 23).

[166] J. Zhang and V.-A. Glezakou, Int. J. Quantum Chem. **121**, e26553 (2021) (cit. on pp. 24, 25).

[167] P. Havu, V. Blum, V. Havu, P. Rinke, and M. Scheffler, Phys. Rev. B **82**, 161418 (2010) (cit. on p. 24).

[168] F. Hanke and J. Björk, Phys. Rev. B **87**, 235422 (2013) (cit. on p. 24).

[169] A. Ramstad, G. Brocks, and P. J. Kelly, Phys. Rev. B **51**, 14504 (1995) (cit. on p. 24).

[170] A. Ohtake, Surf. Sci. Rep. **63**, 295 (2008) (cit. on p. 24).

[171] A. Gloystein, N. Nilius, J. Goniakowski, and C. Noguera, J. Phys. Chem. C **124**, 26937 (2020) (cit. on p. 24).

[172] B. Stanka, W. Hebenstreit, U. Diebold, and S. Chambers, Surf. Sci. **448**, 49 (2000) (cit. on p. 24).

[173] G. S. Parkinson, Surf. Sci. Rep. **71**, 272 (2016) (cit. on p. 24).

[174] G. S. Herman, M. R. Sievers, and Y. Gao, Phys. Rev. Lett. **84**, 3354 (2000) (cit. on p. 24).

[175] Y. Liang, S. Gan, S. A. Chambers, and E. I. Altman, Phys. Rev. B **63**, 235402 (2001) (cit. on pp. 24, 25).

[176] M. R. Castell, Surf. Sci. **505**, 1 (2002) (cit. on p. 24).

[177] P. J. M. van Laarhoven and E. H. L. Aarts, "Simulated annealing," in *Simulated annealing: theory and applications* (Springer Netherlands, Dordrecht, 1987), pp. 7–15 (cit. on p. 25).

[178] D. J. Wales and J. P. K. Doye, J. Phys. Chem. A **101**, 5111 (1997) (cit. on p. 25).

[179] R. Storn and K. Price, J. Glob. Optim. **11**, 341 (1997) (cit. on p. 25).

[180] R. Eberhart and J. Kennedy, in Mhs'95. proceedings of the sixth international symposium on micro machine and human science (1995), pp. 39–43 (cit. on p. 25).

[181] S. T. Call, D. Y. Zubarev, and A. I. Boldyrev, J. Comput. Chem. **28**, 1177 (2007) (cit. on p. 25).

[182] A. Hartmann and H. Rieger, *Optimization algorithms in physics*, 1st ed. (John Wiley & Sons, Ltd, 2001) (cit. on p. 25).

[183] D. Frenkel and B. Smit, *Understanding molecular simulation: from algorithms to applications*, Second, Vol. 1, Computational Science Series (Academic Press, San Diego, 2002) (cit. on p. 25).

[184] J. W. Ponder and D. A. Case, in *Protein simulations*, Vol. 66, Advances in Protein Chemistry (Academic Press, 2003), pp. 27–85 (cit. on p. 26).

[185] A. K. Rappe and W. A. Goddard, J. Phys. Chem. **95**, 3358 (1991) (cit. on p. 26).

[186] A. C. T. van Duin, S. Dasgupta, F. Lorant, and W. A. Goddard, J. Phys. Chem. A **105**, 9396 (2001) (cit. on p. 26).

[187] A. Tikhonov, A. Goncharsky, V. Stepanov, and A. G. Yagola, Vol. 1 (1995), pp. 1–253 (cit. on p. 29).

[188] The MD calculation was performed on two Xeon Gold 6148 processors (Skylake (SKL), 20 cores 2.4 GHz) connected through a 100 Gb/s OmniPath interconnect. (cit. on pp. 39, 40).

[189] F. C. Mocanu, K. Konstantinou, T. H. Lee, N. Bernstein, V. L. Deringer, G. Csányi, and S. R. Elliott, J. Phys. Chem. B **122**, 8998 (2018) (cit. on p. 44).

[190] H. A. Stern and S. E. Feller, J. Chem. Phys **118**, 3401 (2003) (cit. on p. 49).

Appendices

A Publications

A.1 IrO_2 Surface Complexions Identified through Machine Learning and Surface Investigations

Jakob Timmermann, Florian Kraushofer, Nikolaus Resch, Peigang Li, Yu Wang, Zhiqiang Mao, Michele Riva, Yonghyuk Lee, Carsten Staacke, Michael Schmid, Christoph Scheurer, Gareth S. Parkinson, Ulrike Diebold and Karsten Reuter
Phys. Rev. Lett. 125, 206101 (2020).
DOI: 10.1103/PhysRevLett.125.206101

Editors' Suggestion

IrO_2 Surface Complexions Identified through Machine Learning and Surface Investigations

Jakob Timmermann,[1] Florian Kraushofer,[2] Nikolaus Resch,[2] Peigang Li,[3] Yu Wang,[4] Zhiqiang Mao,[3,4] Michele Riva,[2] Yonghyuk Lee,[1] Carsten Staacke,[1] Michael Schmid,[2] Christoph Scheurer,[1] Gareth S. Parkinson,[2] Ulrike Diebold,[2] and Karsten Reuter[1,5,*]

[1]*Chair for Theoretical Chemistry and Catalysis Research Center, Technical University of Munich, Lichtenbergstrasse 4, D-85747 Garching, Germany*

[2]*Institute of Applied Physics, Technical University of Vienna, Wiedner Hauptstrasse 8-10/134, A-1040 Vienna, Austria*

[3]*Department of Physics and Engineering Physics, Tulane University, New Orleans, Louisiana 70118, USA*

[4]*Department of Physics, The Pennsylvania State University, University Park, Pennsylvania 16802, USA*

[5]*Fritz-Haber-Institut der Max-Planck-Gesellschaft, Faradayweg 4-6, D-14195 Berlin, Germany*

(Received 5 July 2020; accepted 22 September 2020; published 10 November 2020)

A Gaussian approximation potential was trained using density-functional theory data to enable a global geometry optimization of low-index rutile IrO_2 facets through simulated annealing. *Ab initio* thermodynamics identifies (101) and (111) (1×1) terminations competitive with (110) in reducing environments. Experiments on single crystals find that (101) facets dominate and exhibit the theoretically predicted (1×1) periodicity and x-ray photoelectron spectroscopy core-level shifts. The obtained structures are analogous to the complexions discussed in the context of ceramic battery materials.

DOI: 10.1103/PhysRevLett.125.206101

First-principles computations based on density-functional theory (DFT) have become a standard tool to determine surface structure. In the standard approach, a set of trial structures are optimized geometrically to identify minima on the ground-state potential-energy surface. Observables are computed to check for consistency with experimental data, and one structure is declared best. While successful, this approach depends on the trial structures, and it is possible that the true surface is simply missed.

With the increasing efficiency of DFT calculations and computational power, DFT-based, global geometry optimization has been heralded as a significant step to overcome this limitation [1–6]. Despite impressive successes of simulated annealing or basin hopping work, this direct approach has never truly affected the popularity of the "trial set and local geometry optimization" approach. The excessive number of computations required by even the most efficient algorithms [7,8] leads to an intractable computational demand, particularly for reconstructions with large surface unit cells. Fortunately, machine-learned (ML) interatomic potentials [9,10] may now overcome this deadlock, and enable a paradigm shift in our approach to automatic structure searches. These potentials can be trained with a feasible number of DFT calculations and, if needed, can be retrained on the fly in the course of an ongoing global geometry optimization. Crucially, the optimization is performed using the inexpensive ML potential, which enables extensive sampling of the configuration space.

Here, we use this approach to find the most stable surface terminations of rutile-structured oxides. Our motivation came from empirical reports that IrO_2 catalysts for proton-exchange membrane water electrolysis exhibit increased activity following electrochemical activation with a small number of reductive formation cycles [11,12]. We hypothesized this might originate in a metal-rich complexion, which is similar to the complexions discussed in the context of ceramic battery materials [13]. A complexion is a surface (or interfacial) phase that possesses a thermodynamically determined equilibrium thickness on the order of nanometers, but is neither a thin version of a known 3D bulk phase nor merely a reconstructed surface layer. While the ubiquity and importance of complex (often large surface-unit-cell) reconstructions at surfaces of compound catalysts under operation conditions is well known [14–18], complexions can be more subtle by only involving deeper compositional changes at unchanged translational symmetry. After training a ML Gaussian approximation potential (GAP) [19,20] with DFT data, simulated-annealing-based global optimization immediately leads to very stable new terminations on the (101) and (111) low-index surfaces of rutile IrO_2 with mixed Ir—Ir and Ir—O bonding. Direct *ab initio* thermodynamics [21] calculations confirm the high stability of these complexions under strongly reducing conditions [22]—not only on IrO_2, but also on RuO_2, which is the alternative state-of-the-art rutile-structured catalyst used in proton-exchange membrane electrolysis. The theoretical predictions are supported by surface investigations of IrO_2 single crystals, which exhibit (101) facets rather than the more common low-energy (110) orientation of rutile [23,24]. Characterization by low-energy

electron diffraction (LEED), scanning-tunneling microscopy (STM), and x-ray photoelectron spectroscopy (XPS) confirms the properties of the predicted metal-rich complexions, explaining why IrO_2 nanoparticles often expose (101) facets [25–31].

Our investigation starts with the creation of a reference database of DFT structures to train the nonparametric GAP potential. GAPs decompose the total energy of a system into a sum of atomic energies that depend on the local chemical environment [19,20]. This dependence is learned from the atomic environments present in the reference database through Gaussian process regression. For energy predictions, the similarity between each atom in an unknown structure and representative training atoms is then determined via a kernel function. In this work, we employ the smooth overlap of atomic positions kernel [32], which considers all neighboring atoms within a radius of 5.5 Å, combined with a simple two-body kernel based on interatomic distances. The reference database comprises 136 structures calculated with QUANTUMESPRESSO [33] and the revised Perdew-Burke-Ernzerhof (RPBE) [34] exchange-correlation functional. These structures span a range of most diverse chemical environments, and comprise various optimized or near-optimum crystalline bulk and low-index surface geometries of different stoichiometry, as well as highly nonequilibrium structures taken from snapshots of high-temperature molecular dynamics (MD) simulations of differently shaped and sized nanoparticles. Validated against an equally diverse set of 39 structures not used in the training, the final GAP reproduces the widely varying DFT formation energies with a mean average error of 25 meV/atom.

To explore a possible formation of complexions, we performed extensive simulated-annealing MD runs for all five symmetry-inequivalent low-index surfaces [35] of rutile IrO_2, each time starting with the metal-rich regular (1×1) termination expected under reducing conditions. Specifically, we employ periodic boundary-condition supercells with thick slabs comprising at least seven rutile trilayers and (3×3) or (4×4) surface unit cells as further detailed in the Supplemental Material (SM) [36]. The temperature is initially raised to around 1000 K for 20 ps, before a slow cooling rate of 3 K/ps is applied during an additional 250 ps. After a final geometry optimization, we obtain new structures with a significantly lower energy, in particular for the (101) [or the symmetry equivalent (011)] and the (111) orientations. Analysis of these structures (Fig. 1) reveals that neither correspond to a reconstruction with a lowered translational symmetry, but is instead a reordering of the original rutile layering sequence that preserves the regular (1×1) lateral periodicity. Direct recalculation and geometry reoptimization of these structures at the DFT-RPBE level confirms the reliability of the GAP prediction. The structures are significantly lower in energy than the regular Ir-rich (1×1) termination for the respective orientation and, in slabs where at least the five topmost layers are allowed to move, the regular Ir-rich (101) termination relaxes barrierlessly into the new complexion.

Within an *ab-initio* thermodynamics framework [21], we can compare the stability of these new structures to all other possible and known (1×1) terminations of rutile IrO_2. Generally, there is at least one metal-rich, one stoichiometric, and one oxygen-rich termination for each low-index facet, with some facets lacking some terminations and some facets additionally allowing for an oxygen-superrich termination (Figs. S7–S11 of SM [36]) [44]. Figure 1 shows the resulting surface phase diagram. Only the lowest surface free energy is shown for each facet as a function of the chemical potential of oxygen $\Delta\mu_O$, and a kink in the

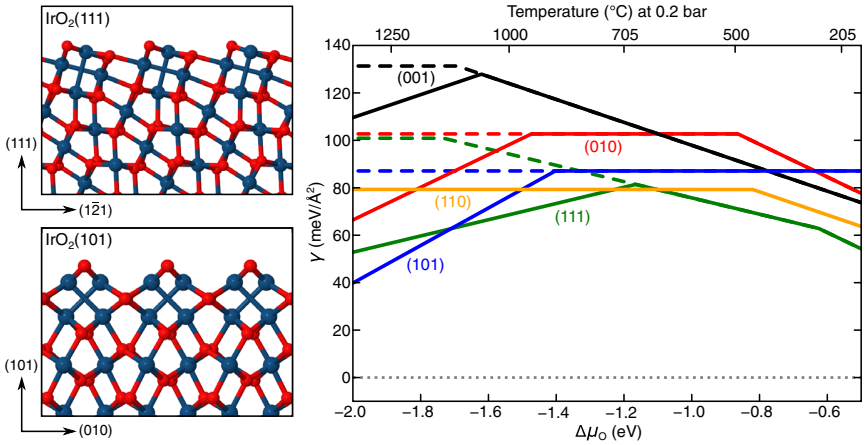

FIG. 1. Left: side views of identified complexions. Ir and O atoms are drawn as blue (large) and red (small) spheres, respectively. Right: computed surface free energies γ of the five symmetry-inequivalent low-index facets in a pure oxygen atmosphere. In the top x axis, the dependence on the oxygen chemical potential $\Delta\mu_O$ is translated into a temperature scale at 0.2 bar pressure (the oxygen partial pressure in air). The dashed lines indicate the surface free energies without complexions.

surface free-energy line reflects a change in the most stable termination. Metal-rich terminations exhibit a positive slope, O-rich terminations a negative slope, and stoichiometric terminations are independent of $\Delta\mu_O$. For low oxygen chemical potentials, the complexions significantly lower the surface free energy and change the relative energetic ordering. The same form and relative ordering of the surface free energies is obtained with the stronger-binding Perdew-Burke-Ernzerhof (PBE) [45] functional, but the entire phase diagram shifts to lower $\Delta\mu_O$ (see Fig. S13 of SM [36]). While we cannot quantify the gas-phase conditions of the phase stability, the (110) facet would clearly be the lowest-energy orientation in reducing environments in the absence of complexations, in line with the predominant focus of surface-science work on this particular facet [23,24]. The stability of the complexions makes the (101) and (111) facets energetically competitive.

In order to test this surprising finding, we investigate the surfaces of IrO_2 single crystals grown in a tube furnace with an O_2 inflow of 100 ml/min at atmospheric pressure. Ir was supplied from Ir powder (Alfa Aesar, 99.99%) at 1250 °C, and flake-shaped IrO_2 crystals formed at the colder end of the furnace (1000 °C). Two of the larger crystallites (both ca. 3 mm^2 top surface area) were chosen for surface studies. Electron backscatter diffraction immediately reveals that all areas where a diffraction pattern could be identified expose (101)-type surfaces (Fig. S18 of SM [36]).

The two IrO_2 samples were then loaded to an ultrahigh vacuum (UHV) chamber and prepared by sputtering (1 keV Ar^+ ions, $p_{Ar} = 8 \times 10^{-6}$ mbar, 10 min) and annealing in oxygen (450 °C, 40 min). Oxygen gas was dosed through an oxygen shower, with the gas outlet very close to the sample. This increases the local pressure by a factor of 10–30 compared to the O_2 pressure measured in the chamber (5×10^{-6} mbar).

Low-energy electron diffraction (LEED) images [Fig. 2(b) herein, and Fig. S20 in the SM [36]] reveal a rectangular pattern with the spots moving toward the center of the screen with increasing incident beam energy. The unit cell size of $(0.58 \pm 0.04) \times (0.47 \pm 0.04)$ nm^2 was quantified using LEED patterns of a Pd(111) single crystal as a reference. These numbers are in good agreement with the (1×1) unit cell of $IrO_2(101)$ (0.55×0.45 nm^2). Some additional diffraction spots are also observed, but these move in nonradial directions with increasing energy, indicating the presence of other facets for which the beam incidence is off normal.

STM images acquired at room temperature after UHV preparation [Fig. 2(a)] exhibit a zigzag pattern with (1×1) periodicity. Since the intrinsic drift of the STM scanner cannot be corrected by comparison to a known structure, distance measurements are unreliable, but the 0.55×0.45 nm^2 spacing expected for an $IrO_2(101)$-(1×1) unit cell fits the data within the expected error. Some bright

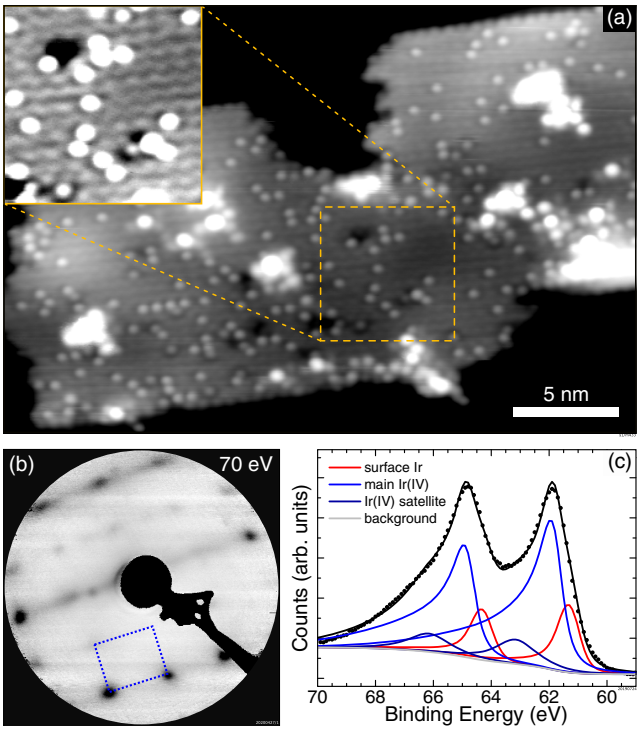

FIG. 2. IrO_2 crystal after UHV preparation. (a) STM image of the IrO_2 sample (30×20 nm^2, $U_{sample} = -2$ V, $I_{tunnel} = 0.2$ nA) with the inset processed to enhance the visibility of the atomic corrugation. (b) LEED pattern from one of the IrO_2 crystals ($E_{electron} = 70$ eV). A rectangular pattern (unit cell drawn in blue) is clearly visible, and its diffraction spots move toward the center of the screen with increasing energy, as expected for normal beam incidence. (c) XPS data (points) and fit (lines) of the Ir $4f$ region (Mg Kα anode).

point features are also visible, which we attribute to either lattice defects or adsorbates. Interestingly, the periodicity of these protrusions cannot be reconciled with a bulk-truncated (1×1) surface (Fig. S22 [36]). On the proposed complexion, the features are located at surface oxygen sites, allowing tentative assignment as either surface hydroxyls or oxygen vacancies.

On one of the samples, a second, pseudohexagonal surface phase was also observed (Fig. S19 [36]). The nearest-neighbor distances were determined as ≈0.55 nm, which would fit an $IrO_2(111)$-(1×1) unit cell. However, since the unit-cell angle cannot be accurately determined by STM alone, a (2×2) superstructure on Ir(111) could, in principle, also fit the data. We also note that a hexagonal reconstruction of the (101) facet was previously observed on rutile $TiO_2(101)$ [46] and attributed to contamination.

XPS of the Ir $4f$ region is shown in Fig. 2(c). We fit the spectrum using peak shapes and oxide satellite peak positions from Ref. [47], which results in a peak at 61.9 eV (blue) due to Ir(IV) and a lower-binding-energy component shifted by 0.6 eV at 61.3 eV (red). This agrees with our initial-state calculations of the $4f$ DFT

Kohn-Sham orbital positions for the $IrO_2(101)$ complexion, which yield an initial-state shift of 0.6 eV for the top two Ir layers with respect to a bulklike Ir atom deeper in the IrO_2 slab using both the RPBE and PBE functionals (see SM [36]). A much larger shift (1.1 eV toward lower binding energies) is predicted for the top layer of the regular Ir-rich (101) termination. We also acquired Ir $4f$ XPS peaks from a freshly sputtered sample (Fig. S21 [36]), which is dominated by a strong contribution of metallic surface iridium at 60.9 eV, in agreement with the position reported in the literature for Ir single crystals [32]. Overall, the experimental evidence clearly shows that the crystals are dominated by (101) facets with a (1×1) surface symmetry, and supports the predicted $IrO_2(101)$-(1×1) complexion. Since the crystal growth direction was not enforced, and the relatively rough, vicinal surfaces would have faceted to a more stable orientation, the dominance of the (101) surface is an indirect confirmation of its thermodynamic stability at the growth conditions.

In our view, the complexions are precursors to a full reduction of the bulk oxide. Two layers with mixed Ir—O and Ir—Ir bonding are obtained through a mere reordering of the rutile layering sequence of the (101) and (111) orientations. The increased coordination of the topmost Ir atoms (from threefold to fourfold) stabilizes the structures. Adding further equivalent complexion layers does not further increase this coordination, and we calculate higher surface free energies for such structures (see Fig. S12 [36]). As such, the identified complexions are novel 2D interphases, and not just thin versions of known 3D bulk structures. They are thus quite analogous to the much discussed surface oxides as precursors to a full oxidation of transition metals [48–50].

With this understanding, one would expect complexions to be a general feature of oxides in reducing environments, and follow-up computations predict that analogous complexions render the (101) and (111) facets energetically competitive for rutile RuO_2 under reducing conditions (Fig. S14 [36]).

In summary, a completely unexpected class of surface structures was readily identified for a well-studied type of oxide crystals using ML interatomic potentials. That such simple structures have consistently eluded previous trial-structure-based surface structure determination work on IrO_2 or RuO_2 shows them to be counterintuitive, and one wonders how many more surprises await us when global geometry optimization based on predictive-quality machine-learned potentials has reached full maturity.

See Supplemental Material [36] for additional detailed information on the reference database employed for the training of the ML potential and simulated-annealing runs, on the *ab initio* thermodynamics results, on the initial-state core level-shift calculations, as well as on the experimental growth and characterization work.

All input and output files for the DFT training structures are available at the NOMAD database [51].

This research was supported by the Kopernikus/P2X programme (Cluster FC-A1) of the German Federal Ministry of Education and Research, the German Federal Environmental Foundation DBU, and the German Academic Exchange Service DAAD. U. D., M. R., and F. K. acknowledge support by the Austrian Science Fund (FWF, Z-250, Wittgenstein Prize). G. S. P. acknowledges funding from the European Research Council (ERC) under the European Union's Horizon 2020 research and innovation program Grant Agreement No. 864628. N. R. was supported by the Austrian Science Fund (FWF, Y847-N20, START Prize). Z. M. acknowledges the support from the U.S. National Science Foundation under Grant No. DMR 1917579. We acknowledge fruitful discussions with Johannes Margraf and Simon Wengert. The authors thank Andreas Steiger-Thirsfeld (Universitäre Service-Einrichtung für Transmissions-Elektronenmikroskopie, TU Wien) for support with SEM measurements.

*Corresponding author.
karsten.reuter@ch.tum.de

[1] G. Kresse, W. Bergermayer, R. Podloucky, E. Lundgren, R. Koller, M. Schmid, and P. Varga, Complex surface reconstructions solved by *ab initio* molecular dynamics, Appl. Phys. A **76**, 701 (2003).
[2] H. A. Hussein, J. B. A. Davis, and R. L. Johnston, DFT global optimisation of gas-phase and MgO-supported sub-nanometre AuPd clusters, Phys. Chem. Chem. Phys. **18**, 26133 (2016).
[3] C. Panosetti, K. Krautgasser, D. Palagin, K. Reuter, and R. J. Maurer, Global materials structure search with chemically motivated coordinates, Nano Lett. **15**, 8044 (2015).
[4] L. B. Vilhelmsen and B. Hammer, A genetic algorithm for first principles global structure optimization of supported nano structures, J. Chem. Phys. **141**, 044711 (2014).
[5] R. B. Wexler, T. Qiu, and A. M. Rappe, Automatic prediction of surface phase diagrams using *ab initio* grand canonical Monte Carlo, J. Phys. Chem. C **123**, 2321 (2019).
[6] Y. Zhou, M. Scheffler, and L. M. Ghiringhelli, Determining surface phase diagrams including anharmonic effects, Phys. Rev. B **100**, 174106 (2019).
[7] D. J. Wales, J. P. K. Doye, M. A. Miller, P. N. Mortenson, and T. R. Walsh, Energy landscapes: From clusters to biomolecules, in *Advances in Chemical Physics*, edited by I. Prigogine and S. A. Rice (Wiley, 2000), Vol. 115, https://doi.org/10.1002/9780470141748.ch1.
[8] J. D. Pintér, *Global Optimization: Scientific and Engineering Case Studies*, Nonconvex Optimization and Its Applications, Vol. 85 (Springer, New York, 2006).
[9] M. Rupp, O. A. von Lilienfeld, and K. Burke, Guest editorial: special topic on data-enabled theoretical chemistry, J. Chem. Phys. **148**, 241401 (2018).
[10] J. Behler, Perspective: Machine learning potentials for atomistic simulations, J. Chem. Phys. **145**, 170901 (2016).

[11] A. Weiß, A. Siebel, M. Bernt, T.-H. Shen, V. Tileli, and H. A. Gasteiger, Impact of intermittent operation on lifetime and performance of a PEM water electrolyzer, J. Electrochem. Soc. **166**, F487 (2019).
[12] T. Reier, D. Teschner, T. Lunkenbein, A. Bergmann, S. Selve, R. Kraehnert, R. Schlögl, and P. Strasser, Electrocatalytic oxygen evolution on iridium oxide: Uncovering catalyst-substrate interactions and active iridium oxide species, J. Electrochem. Soc. **161**, F876 (2014).
[13] J. Luo, Let thermodynamics do the interfacial engineering of batteries and solid electrolytes, Energy Storage Mater. **21**, 50 (2019).
[14] J. M. P. Martirez, S. Kim, E. H. Morales, B. T. Diroll, M. Cargnello, T. R. Gordon, C. B. Murray, D. A. Bonnell, and A. M. Rappe, Synergistic oxygen evolving activity of a TiO_2-rich reconstructed $SrTiO_3(001)$ surface, J. Am. Chem. Soc. **137**, 2939 (2015).
[15] X. Rong and A. M. Kolpak, Ab initio approach for prediction of oxide surface structure, stoichiometry, and electrocatalytic activity in aqueous solution, J. Phys. Chem. Lett. **6**, 1785 (2015).
[16] A. B. Laursen *et al.*, Climbing the volcano of electrocatalytic activity while avoiding catalyst corrosion: Ni_3P, a hydrogen evolution electrocatalyst stable in both acid and alkali, ACS Catal. **8**, 4408 (2018).
[17] R. B. Wexler, J. M. P. Martirez, and A. M. Rappe, Active role of phosphorus in the hydrogen evolving activity of nickel phosphide (0001) surfaces, ACS Catal. **7**, 7718 (2017).
[18] M. Riva, M. Kubicek, X. Hao, G. Franceschi, S. Gerhold, M. Schmid, H. Hutter, J. Fleig, C. Franchini, B. Yildiz, and U. Diebold, Influence of surface atomic structure demonstrated on oxygen incorporation mechanism at a model perovskite oxide, Nat. Commun. **9**, 1 (2018).
[19] A. P. Bartók, M. C. Payne, R. Kondor, and G. Csányi, Gaussian Approximation Potentials: The Accuracy of Quantum Mechanics, without the Electrons, Phys. Rev. Lett. **104**, 136403 (2010).
[20] V. L. Deringer, M. A. Caro, and G. Csányi, Machine learning interatomic potentials as emerging tools for materials science, Adv. Mater. **31**, 1902765 (2019).
[21] K. Reuter, *Ab initio* thermodynamics and first-principles microkinetics for surface catalysis, Catal. Lett. **146**, 541 (2016).
[22] C. L. McDaniel and S. J. Schneider, Phase relations in the Ru-Ir-O_2 system in air, J. Res. Natl. Bur. Stand., Sect. A **73A**, 213 (1969).
[23] Z. Liang, T. Li, M. Kim, A. Asthagiri, and J. F. Weaver, Low-temperature activation of methane on the $IrO_2(110)$ surface, Science **356**, 299 (2017).
[24] M. J. S. Abb, T. Weber, L. Glatthaar, and H. Over, Growth of ultrathin single-crystalline $IrO_2(110)$ films on a $TiO_2(110)$ single crystal, Langmuir **35**, 7720 (2019).
[25] Y. Lee, J. Suntivich, K. J. May, E. E. Perry, and Y. Shao-Horn, Synthesis and activities of rutile IrO_2 and RuO_2 nanoparticles for oxygen evolution in acid and alkaline solutions, J. Phys. Chem. Lett. **3**, 399 (2012).
[26] X. Zeng, D. Dang, L. Leng, C. You, G. Wang, C. Zhu, and S. Liao, Doped reduced graphene oxide mounted with IrO_2 nanoparticles shows significantly enhanced performance as a cathode catalyst for Li-O_2 batteries, Electrochim. Acta **192**, 431 (2016).
[27] C. Felix, J. B. Bladergroen, V. Linkov, G. B. Pollet, and S. Pasupathi, *Ex-situ* electrochemical characterization of IrO_2 synthesized by a modified Adams fusion method for the oxygen evolution reaction, Catalysts **9**, 318 (2019).
[28] W.-H. Ryu, Y. W. Lee, Y. S. Nam, D.-Y. Youn, C. B. Park, and I.-D. Kim, Crystalline IrO_2-decorated TiO_2 nanofiber scaffolds for robust and sustainable solar water oxidation, J. Mater. Chem. A **2**, 5610 (2014).
[29] W. W. Pai, T. Y. Wu, C. H. Lin, B. X. Wang, Y. S. Huang, and H. L. Chou, A cross-sectional scanning tunneling microscopy study of IrO_2 rutile single crystals, Surf. Sci. **601**, L69 (2007).
[30] S. Anantharaj, P. E. Karthik, and S. Kundu, Self-assembled IrO_2 nanoparticles on a DNA scaffold with enhanced catalytic and oxygen evolution reaction (OER) activities, J. Mater. Chem. A **3**, 24463 (2015).
[31] K. Guo, Y. Li, T. Yuan, X. Dong, X. Li, and H. Yang, Ultrafine IrO2 nanoparticle-decorated carbon as an electrocatalyst for rechargeable Li-O_2 batteries with enhanced charge performance and cyclability, J. Solid State Electrochem. **19**, 821 (2015).
[32] A. P. Bartók, R. Kondor, and G. Csányi, On representing chemical environments, Phys. Rev. B **87**, 184115 (2013).
[33] P. Giannozzi *et al.*, QUANTUM ESPRESSO: a modular and open-source software project for quantum simulations of materials, J. Phys.: Condens. Matter **21**, 395502 (2009).
[34] B. Hammer, L. B. Hansen, and J. K. Nørskov, Improved adsorption energetics within density-functional theory using revised Perdew-Burke-Ernzerhof functionals, Phys. Rev. B **59**, 7413 (1999).
[35] D. Opalka, C. Scheurer, and K. Reuter, *Ab Initio* thermodynamics insight into the structural evolution of working IrO_2 catalysts in proton-exchange membrane electrolyzers, ACS Catal. **9**, 4944 (2019).
[36] See Supplemental Material at http://link.aps.org/supplemental/10.1103/PhysRevLett.125.206101 for additional details regarding computations and experiments, which also includes Refs. [37–43].
[37] D. R. Hamann, Optimized norm-conserving Vanderbilt pseudopotentials, Phys. Rev. B **88**, 085117 (2013).
[38] K. Reuter and M. Scheffler, Composition, structure, and stability of $RuO_2(110)$ as a function of oxygen pressure, Phys. Rev. B **65**, 035406 (2001).
[39] K. Reuter and M. Scheffler, First-Principles Atomistic Thermodynamics for Oxidation Catalysis: Surface Phase Diagrams and Catalytically Interesting Regions, Phys. Rev. Lett. **90**, 046103 (2003).
[40] M. W. Chase, *NIST-JANAF Thermochemical Tables*, 4th ed. (AIP, New York, 1998), https://dx.doi.org/10.18434/T42S31.
[41] M. Schmid, Chemical potential calculator, http://www.iap.tuwien.ac.at/www/surface/chemical_potentials.
[42] V. Blum, R. Gehrke, F. Hanke, P. Havu, V. Havu, X. Ren, K. Reuter, and M. Scheffler, *Ab initio* molecular simulations with numeric atom-centered orbitals, Comput. Phys. Commun. **180**, 2175 (2009).
[43] V. Pfeifer *et al.*, The electronic structure of iridium oxide electrodes active in water splitting, Phys. Chem. Chem. Phys. **18**, 2292 (2016).

[44] T. Wang, J. Jelic, D. Rosenthal, and K. Reuter, Exploring pretreatment-morphology relationships: ab initio Wulff construction for RuO_2 nanoparticles under oxidising conditions, ChemCatChem **5**, 3398 (2013).

[45] J. P. Perdew, K. Burke, and M. Ernzerhof, Generalized Gradient Approximation Made Simple, Phys. Rev. Lett. **77**, 3865 (1996).

[46] O. Dulub, C. Di Valentin, A. Selloni, and U. Diebold, Structure, defects, and impurities at the rutile $TiO_2(001)$ -(2×1) surface: A scanning tunneling microscopy study, Surf. Sci. **600**, 4407 (2006).

[47] S. J. Freakley, J. Ruiz-Esquius, and D. J. Morgan, The X-ray photoelectron spectra of Ir, IrO_2 and $IrCl_3$ revisited, Surf. Interface Anal. **49**, 794 (2017).

[48] E. Lundgren, G. Kresse, C. Klein, M. Borg, J. N. Andersen, M. De Santis, Y. Gauthier, C. Konvicka, M. Schmid, and P. Varga, Two-Dimensional Oxide on Pd(111), Phys. Rev. Lett. **88**, 246103 (2002).

[49] C. T. Campbell, Transition Metal Oxides: Extra Thermodynamic Stability as Thin Films, Phys. Rev. Lett. **96**, 066106 (2006).

[50] K. Reuter, Nanometer and subnanometer thin oxide films at surfaces of late transition metals, in *Nanocatalysis*, edited by U. Heiz and U. Landman (Springer, Berlin, 2007), p. 343–376, https://doi.org/10.1007/978-3-540-32646-5_5.

[51] All input and output files for the DFT training structures are available at the NOMAD database and can be retrieved under the link https://dx.doi.org/10.17172/NOMAD/2020.08.23-2.

A.2 Data-Efficient Iterative Training of Gaussian Approximation Potentials: Application to Surface Structure Determination of Rutile IrO_2 and RuO_2

Jakob Timmermann, Yonghyuk Lee, Carsten Staacke, Johannes T. Margraf, Christoph Scheurer and Karsten Reuter
J. Chem. Phys. (in press)
DOI: 10.1063/5.0071249

Data-Efficient Iterative Training of Gaussian Approximation Potentials: Application to Surface Structure Determination of Rutile IrO_2 and RuO_2

Jakob Timmermann,[1] Yonghyuk Lee,[1] Carsten Staacke,[1] Johannes T. Margraf,[1] Christoph Scheurer,[1] and Karsten Reuter[1]

Fritz-Haber-Institut der Max-Planck-Gesellschaft, Faradayweg 4-6, D-14195 Berlin (Germany)

(*Electronic mail: reuter@fhi-berlin.mpg.de)

(Dated: 3 November 2021)

Machine-learning interatomic potentials like Gaussian Approximation Potentials (GAPs) constitute a powerful class of surrogate models to computationally involved first-principles calculations. At similar predictive quality but significantly reduced cost, they could leverage otherwise barely tractable extensive sampling as in global surface structure determination (SSD). This efficiency is jeopardized though, if an *a priori* unknown structural and chemical search space as in SSD requires an excessive number of first-principles data for the GAP training. To this end, we present a general and data-efficient iterative training protocol that blends the creation of new training data with the actual surface exploration process. Demonstrating this protocol with the SSD of low-index facets of rutile IrO_2 and RuO_2, the involved simulated annealing on the basis of the refining GAP identifies a number of unknown terminations even in the restricted sub-space of (1×1) surface unit-cells. Especially in an O-poor environment, some of these, then metal-rich terminations, are thermodynamically most stable and are reminiscent of complexions as discussed for complex ceramic materials.

I. INTRODUCTION

Machine-learning (ML) interatomic potentials trained with first-principles data promise steep advances for the predictive-quality modeling and simulation of molecules and materials.[1–10] At a computational cost that is significantly reduced compared to direct first-principles calculations, such ML potentials allow to address larger system sizes or perform more extensive dynamical simulations and sampling. While typically not as cost efficient as classical force fields with fixed functional form, they straightforwardly allow to include reactivity and, most importantly, can seamlessly be improved by additional training data.[11]

This versatility also has its downsides though. With the ML potential itself completely void of any physics, the training data needs to adequately cover the structural and chemical space of interest. Depending on the application, the underlying multiple first-principles calculations for the training data could then themselves start to become a computational bottleneck. The latter is e.g. particularly pronounced for surface science or interfacial applications like heterogeneous catalysis or batteries. There, training structures may necessarily extend to large supercell calculations, which even on an efficient semi-local density-functional theory (DFT) level may constitute a formidable computational burden. This calls for data-efficient training protocols that achieve a reliable ML potential with a minimum number of DFT training data (of tractable system sizes).

A further complication in this respect is that the targeted chemical space may actually not be known *a priori* at the beginning of a study. Take the example of surface structure determination that we want to specifically pursue here. We would like to use an ML potential to afford global structure determination techniques and identify unknown, possibly complex surface structures with non-bulk-like coordinations and chemical composition. If we do not know these structures beforehand, how can we make sure our training set covers all relevant local geometric and compositional motifs, while simultaneously being of minimum size?

The obvious solution to this challenge is to resort to iterative training protocols[12]. While exploring new parts of chemical space, some form of uncertainty quantification will allow the ML potential to realize that it requires new pertinent training data. Corresponding new first-principles calculations will (ideally automatically) be initiated and the potential be retrained. By now a number of such iterative learning strategies have been reported, e.g. for elementary carbon or silicon,[13–16] binary bulk materials like zirconia,[17] nanoparticles[12,18,19] and even for selected surface morphologies[20]. While conceptionally all similar, technical differences between these approaches extend from the ML model used (e.g. full or sparse kernel regression, neural networks) over the way the uncertainty is measured (e.g. committee/ensemble methods, Bayesian uncertainty or dissimilarity to existing training data) to the way the automatized protocol is tailored to the targeted application (e.g. learning of the full potential energy surface or only of parts of it, with same or variable accuracy). In this context, we here present and detail a two-stage highly data-efficient training protocol specifically geared toward surface structure determination and based on sparse Gaussian process regression. It consists of an initial bootstrapping, in which existing domain knowledge on the system of interest is used to generate a suitable preliminary training set and arrive at a rudimentary ML potential that satisfactorily describes key physical properties. In a second stage, this training set is iteratively augmented and the potential refined. Importantly, this refinement stage uses simulated annealing (SA) on the ML potential energy surface to efficiently sample the complex phase space of surface structures and identify new training structures as those that exceed a critical dissimilarity to those already computed at the first-principles level before. In this way, the training gets intimately intermingled with the actual global optimization process and the evolving, minimum-size

training set is ideally tailored to identify candidate structures that can subsequently be compared within an *ab initio* thermodynamics surface phase diagram[21,22].

We specifically demonstrate this approach by developing Gaussian Approximation Potentials (GAPs)[1,23] for the surface structure determination of low-index rutile IrO_2 and RuO_2 facets. Both oxides are known active oxidation catalysts in thermal and electro catalysis, but equally known for their propensity to undergo surface structural and compositional changes under operating conditions[24–34]. In preceding work by some of us,[10] a GAP potential based surface structure determination could already identify hitherto unknown, so-called surface complexions for some IrO_2 facets. The iterative training of the potential was largely manual though, and involved the addition of training structures based on visual inspection or the random addition of nanoparticle and high-temperature structures for a perceived training set diversity. Unsatisfied with this, we here revisit the problem with our automated training protocol that after the initial bootstrapping does not require any further human decision making. In turn, the bootstrapping set itself consists of those reference structures (bulk, molecular, canonical surface terminations) that would always have been explicitly computed by first-principles in a surface structure determination project anyway. Gratifyingly, this new protocol identifies exactly the same complexions as the laboriously developed GAP potential before. Moreover, the transferability of the protocol is demonstrated by the application to RuO_2. In our preceding work, we had simply recomputed the identified IrO_2 complexions for this iso-structural oxide to demonstrate their stability. Intriguingly, the new protocol not only confirms this, but reveals that RuO_2 surfaces in fact exhibit an even wider variety of these novel surface terminations.

II. METHODS

A. Gaussian Approximation Potentials

GAPs are a widely used class of interatomic ML potentials, based on Gaussian process regression. A detailed description is provided in the literature.[1,23,35] For self-containment, we therefore provide here only a brief introduction to the formalism, emphasizing the aspects most relevant to this project.

Interatomic Potential: The GAPs used herein are based on a combination of two-body (2B) and many-body (MB) contributions. This means that we calculate the total energy E_{GAP} of a system from its atomic coordinates $\mathbf{X_n}$ as

$$E_{\mathrm{GAP}}(\mathbf{X_n}) = \underbrace{\sum_{i,j} \delta_{\mathrm{2B}}^2 \sum_{m=1}^{M_{\mathrm{2B}}} c_{m,\mathrm{2B}} k_{\mathrm{2B}}(r_{ij}, r_m)}_{E_{\mathrm{2B}}} + \underbrace{\sum_{i} \delta_{\mathrm{MB}}^2 \sum_{m=1}^{M_{\mathrm{MB}}} c_{m,\mathrm{MB}} k_{\mathrm{MB}}(\boldsymbol{\chi}_i, \boldsymbol{\chi}_m)}_{E_{\mathrm{MB}}} \quad . \tag{1}$$

Here, the first sum in E_{2B} goes over all pairs of atoms i, j, and the first sum in E_{MB} goes over each atom i. The second sum in each term goes over a set of $M_{\mathrm{2B/MB}}$ representative data points (the sparse set, see below), and contains the regression coefficients $c_{m,\mathrm{2B/MB}}$ and the respective kernel functions $k_{\mathrm{2B/MB}}$. The latter are used to measure the similarity between two geometric descriptors (representations), which are computed from $\mathbf{X_n}$. In the 2B case, these are simply interatomic distances r_{ij}. In the MB case, these are vectorial representations of the atomic environment $\boldsymbol{\chi}_i$, based on the Smooth Overlap of Atomic Positions (SOAP).[1,23] A more detailed description of the kernel functions and representations used herein is given below. The final yet undefined parameters in Eq. (1) are δ_{2B} and δ_{MB}, which are used to specify the expected relative weighting of the two energy contributions.

While a full MB description of the interatomic potential is in principle possible, the explicit inclusion of a 2B term has been found to lead to significantly more stable and data-efficient potentials.[13] The reason is that, due to its high flexibility, the high-dimensional representation used for the MB contribution extrapolates much more poorly than a simple 2B potential. The weighting specified by the δ parameters can therefore be used to switch between a less flexible but more robust potential with strong 2B character and a highly flexible MB potential.

Assuming a given choice of kernel and representation (and a training database), this leaves the determination of the regression coefficients $c_{m,\mathrm{2B/MB}}$. In GAPs these are obtained by minimizing the regularized least-squares loss function

$$\ell = \sum_{n=1}^{N} \frac{|y_n - \bar{y}(\mathbf{X_n})|^2}{\sigma_n^2} + R \quad . \tag{2}$$

Here, R is a Tikhonov regularization term (see ref. 35 for details), y_n are reference data points (in the present case, total energies and force components on all atoms of the training structures) and σ_n is an inverse weighting factor for a given data point. $\bar{y}(\mathbf{X_n})$ indicates the GAP prediction for the property y_n, given the atomic coordinates $\mathbf{X_n}$ based on the coefficients $c_{m,\mathrm{2B/MB}}$. Specifically, this means that energies are predicted according to Eq. (1) and force components by taking the corresponding derivative.

The role of the regularization term R is to penalize large regression coefficients, which indicate overfitting. As increasing the magnitude of σ_n increases the relative contribution of R to the loss function, these parameters are often called regularization strengths (particularly if a single parameter is used for all data points). Alternatively, they can be interpreted as the uncertainty associated with a given data point or the expected accuracy of the GAP. In other words: Larger values of σ_n lead to a smoother potential, smaller values to a more precise fit of the training set. Furthermore, using different values of σ_n for energies and forces allows adjusting the weight of these properties in the loss function.

Kernels and Representations: The central components in the GAP energy expression of Eq. (1) are the kernel functions $k_{\mathrm{2B/MB}}$ and the corresponding geometric representations. Kernel functions are simply a similarity measure between representations usually ranging from 0 (not similar at all) to 1 (identical). In this sense, an intuitive explanation of a

GAP model is that it predicts the energy of a configuration according to its similarity to other configurations in the training set. Since this similarity is defined by the choice of representations and kernels, these are critical to the performance of the model.

For the two-body contribution, the representation of a pair of atoms is simply its interatomic distance r_{ij} and a squared exponential (Gaussian) kernel is used as a similarity measure,

$$k_{\mathrm{2B}}(r_{ij}, r_m) = \exp\left(-\frac{\|r_{ij} - r_m\|^2}{2\sigma_{\mathrm{2B}}^2} \right) \quad . \tag{3}$$

Inspecting Eq. (1), this means that E_{2B} is a pair-potential, which consists of M_{2B} Gaussians of width σ_{2B} centered at the sparse points r_m (see below). Note that, in order to ensure size-extensivity and favorable computational scaling, the two-body potential is constrained to be short-ranged. To this end, a cutoff parameter $r_{\mathrm{cut,2B}}$ is defined.

For the MB contribution to the potential, the SOAP representation and kernel are used. The main idea of SOAP is to generate a rotationally and permutationally invariant fingerprint of the local atomic environment within a sphere of radius $r_{\mathrm{cut,SOAP}}$ around a given central atom i. To this end, the environment is represented as a smooth density function ρ, which is obtained by smearing out the atomic positions of all atoms in the environment with Gaussian functions of width σ_{SOAP}. This density is then expanded with a set of basis functions centered on i, consisting of spherical harmonics and orthogonal radial functions. Finally, the corresponding expansion coefficients are transformed into the rotationally invariant power spectrum and collected in a normalized vector $\boldsymbol{\chi}_i$, which is the SOAP representation.

As a similarity measure, the SOAP representation is typically used with low-order polynomial kernels, so that

$$k_{\mathrm{MB}}(\boldsymbol{\chi}_i, \boldsymbol{\chi}_m) = (\boldsymbol{\chi}_i \cdot \boldsymbol{\chi}_m)^{\zeta} \quad . \tag{4}$$

Herein, we use $\zeta = 2$ throughout. To fully define the SOAP representation, the number of radial and angular basis functions (n_{max} and l_{max}) needs to be specified.[1,23]

Sparsification: An essential aspect of GAP models is that they use a sparse variant of Gaussian process regression (GPR). This is important because the training cost of full GPR models scales cubically with the number of training data points N (and the prediction cost linearly). This quickly becomes prohibitive for large training sets, in particular when also training on forces (where each force component on each atom inside a training structure provides one data point). Sparse GPR models still use the full training set in the loss function, Eq. (2), but only use a sparse set of $M < N$ data points in the energy expression Eq. (1). In this manner, the training costs are substantially reduced and the energy prediction cost becomes formally independent of the training set size. Of course, this means that the sparse points need to be suitably selected.

For the two-body potential this is achieved by placing the sparse points on a regular grid between zero and the cutoff length $r_{\mathrm{cut,2B}}$. For the high dimensional MB potential such a grid would be extremely inefficient, however. If the training set is reasonably small (i.e. on the order of 1000 unique atomic environments per element), all atomic environments can be used as sparse points instead. For larger training sets, the most diverse environments of each species are selected using CUR decomposition.[36] Note that even if all environments are used, a GAP is always a sparse GPR model, as the full GPR model would use a regression coefficient for every single force component in the training set. This becomes prohibitive even for fairly small training sets, so that training a GPR model on forces in practice always requires sparsification.

Kernel Distance: In addition to being a crucial ingredient of the GAPs themselves, the SOAP kernel can also be used for selecting new training structures for the iterative training scheme described below. To obtain a data-efficient approach, it is important to ensure that the structures that are iteratively added to the training set are maximally different from training configurations already present in the set. As discussed above, SOAP measures the similarity of atomic environments and not of complete configurations of atoms, however. It is therefore common to use the averaged or matched similarities of the environments in two configurations for such a selection task.[11,37] While this is very useful for comparing and mapping structures,[38] such global comparisons can overshadow the presence of a single unusual atomic environment, in an otherwise similar configuration. This is particularly prominent in surface applications, where inside the employed supercells a dominant fraction of bulk-like atoms is always present in the inner layers of the slab. We therefore rather define the similarity of configurations A and B (where B could also be a group of different configurations) by the *minimal* similarity $k_{\mathrm{MB}}(\boldsymbol{\chi}_a, \boldsymbol{\chi}_b)$ between two atoms $a \in A$ and $b \in B$, where only identical species are compared. For convenience, we further convert this similarity provided by the SOAP kernel into a kernel distance using

$$\kappa(A,B) = \sqrt{2 - 2\min_{\substack{a\in A \\ b\in B}}(k_{\mathrm{MB}}(\boldsymbol{\chi}_a, \boldsymbol{\chi}_b))} \quad , \tag{5}$$

where a larger distance $\kappa(A,B)$ indicates more dissimilar structures.

B. Density-Functional Theory Calculations

Computational Settings: To achieve a predictive-quality GAP, all training data for both metallic oxides are computed with first-principles semi-local DFT using the revised Perdew-Burke-Erzerhof (RPBE)[39] functional to treat electronic exchange and correlation. The periodic boundary condition calculations are performed using a plane-wave basis set together with SG15 optimized norm-conserving Vanderbilt pseudopotentials[40] as implemented in the QuantumEspresso software package[41]. The kinetic cutoff energy for the expansion of the wave function and the charge density is set to 80 Ry and 320 Ry, respectively, and Brillouin zone integrations are performed with a uniform reciprocal distance of $0.02\,\mathrm{\AA}^{-1}$. This generates $(11 \times 11 \times 16)$ k-point grids for both rutile IrO_2

and RuO_2 bulk unit cells, and corresponding grids for the various surface supercell calculations. Optimized lattice parameters for both oxides are obtained by minimizing the stress tensor and all internal degrees of freedom iteratively until the external pressure falls below 0.5 kbar. Geometry optimization for the surface calculations employed Broyden-Fletcher-Goldfarb-Shanno (BFGS) minimization[42–44] until residual changes in total energy and all force components fell below 1.4×10^{-2} meV and 0.3 meV/Å, respectively. At these computational settings, convergence tests detailed in the Supporting Information (SI) demonstrate a high degree of convergence of the key quantities entering the GAP potential training, i.e. surface free energies to within 5 meV/atom and forces to within 50 meV/Å.

Supercell Setups: All five symmetry-inequivalent low-index surfaces (*hkl*) of rutile IrO_2 and RuO_2 are modeled via a supercell approach.[24,33] Each slab model exposes a (1×1) surface unit-cell and contains at least seven trilayers of MO_2 units (see Table S1 for a detailed list). A minimum vacuum region of 15 Å thickness prevents interactions between periodic slabs. Truncation at different planes in the (*hkl*) crystal orientation generally gives rise to one metal-rich, one stoichiometric, and one oxygen-rich termination for all considered facets. One exception is (111), where two different stoichiometric terminations arise. Likewise, for the (001) facet layered truncation leads only to a stoichiometric termination. Here, we therefore also consider one termination with an oxygen vacancy and one termination with an excess oxygen at the very top layer to build a metal-rich and oxygen-rich termination for this orientation, respectively. Under strongly oxidizing conditions, the rutile surfaces are furthermore known to stabilize peroxo-type surface moieties[24,33]. One such peroxo-termination for each facet is thus also considered, with all structures further detailed in the SI.

Ab Initio Thermodynamics: In order to determine the relative stability of different surface structures in thermodynamic equilibrium with a surrounding oxygen-containing gas phase, we adopt the *ab initio* thermodynamics approach[21,22] and calculate the surface free energy $\gamma_{\text{surf}}^{(hkl),\sigma}$ of a given crystallographic orientation (*hkl*) and termination σ as

$$\gamma_{\text{surf}}^{(hkl),\sigma} = \frac{1}{A^{(hkl)}}\left[G_{\text{surf}}^{(hkl),\sigma} - \sum_i n_i^{(hkl),\sigma}\mu_i\right] \quad . \tag{6}$$

Here, $G_{\text{surf}}^{(hkl),\sigma}$ is the Gibbs free energy of the surface system with surface area $A^{(hkl)}$, and μ_i is the chemical potential of various species i (i =Ir (or Ru) and O) present in the system. $n_i^{(hkl),\sigma}$ is the number of atoms of species i within the periodic supercell of the slab model.

Assuming the surface to be in thermodynamic equilibrium with the respective bulk MO_2 (M=Ir and Ru) phase, we can connect the chemical potentials of metal (μ_{M}) and oxygen (μ_{O}) to the Gibbs free energy of MO_2 bulk, $G_{\text{MO}_2,\text{bulk}} = \mu_{\text{M}} + 2\mu_{\text{O}}$. The chemical potential of oxygen is instead set by the equilibrium with the surrounding gas phase. It is calculated as $\mu_{\text{O}} = \frac{1}{2}E_{\text{O}_2} + \Delta\mu_{\text{O}}$, with E_{O_2} the total energy of an isolated O_2 molecule including zero point energy (ZPE) contributions[45] and the relative chemical potential $\Delta\mu_{\text{O}}$ allowing to connect to finite temperature and pressure (T,p).[21,22]. In the difference in Eq. (6) the condensed-phase Gibbs free energies are approximated by the DFT-computed total energies.[21] The final working equation to determine the surface free energies thus reads

$$\gamma_{\text{surf}}^{(hkl),\sigma}(\Delta\mu_{\text{O}}) = \frac{1}{2A^{(hkl)}}\Big[E_{\text{surf}}^{(hkl),\sigma} - n_{\text{M}}^{(hkl),\sigma}E_{\text{MO}_2,\text{bulk}} - \left(n_{\text{O}}^{(hkl),\sigma} - 2n_{\text{M}}^{(hkl),\sigma}\right)\left(\frac{1}{2}E_{\text{O}_2} + \Delta\mu_{\text{O}}\right)\Big] \quad . \tag{7}$$

C. Molecular Dynamics Simulations

Simulation Details: All GAP based molecular dynamics (MD) simulations are performed with the LAMMPS code[46] and using the velocity Verlet algorithm as time integrator[47]. The periodic boundary condition simulation cells contain (1×1) symmetric slabs with at least 7 trilayers (see Table S1 for all unit-cell lattice vectors and slab thicknesses), separated by at least 15 Å vacuum.

Simulated Annealing: For the combined global geometry optimization and iterative identification of new structural motifs for GAP training, we employ a SA protocol. Exploiting the small volumetric thermal expansion coefficients for both IrO_2 and RuO_2,[48] the SA is carried out at a 1 fs time step within a canonical ensemble, and only relies on an efficient Berendsen thermostat[49]. In the SA, the temperature is first raised from 200 to 1000 K for 500 ps. After that, the system is quenched back to 200 K within another 500 ps, i.e. we apply a constant heating and cooling rate of 1.6 K/ps. The initial GAP V_0 generated from the bootstrapping set, see below, still offers only a poor description of the potential energy surface, which is why for the SA in the very first refinement step we chose to only heat up to 500 K with a decreased heating and cooling rate of 0.8 K/ps.

The resulting finite temperature structure after each SA is finally fully optimized through conjugate gradient minimization with the same convergence threshold as used for the DFT calculations. For the surface structures contained in the initial training set, these optimized structures are obtained by minimization starting from the bulk-truncated geometries.

III. RESULTS AND DISCUSSION

A. Data-Efficient Simultaneous GAP Training and Surface Exploration Protocol

Bootstrapping: Our iterative GAP training protocol starts with a bootstrapping step, in which we assemble an initial data set to establish a preliminary potential. This first GAP V_0 should fulfill certain minimum criteria regarding the anticipated chemistry of the targeted system and application. One guideline is thus to select training structures that optimally convey this chemistry and (largely) cure obvious teething

problems such as non-physical atomic pair potentials or a (concomitant) instability of key reference structures. In view of data efficiency another guideline is to select training structures that provide maximum information (e.g. in form of symmetry-allowed forces on atoms) at minimum DFT computational cost (e.g. for small supercell structures).

To the least, the GAP V_0 should cover the bulk reference states of the species in the system, i.e. here crystalline rutile MO_2 and the gas-phase O_2 dimer. Next to the mandatory atomic energies (in case of oxygen provided as 1/2 of the O_2 energy), our initial training set therefore contains O_2 dimer data at varying O-O bond lengths that extend over the attractive, equilibrium and repulsive part of the DFT O-O binding energy curve. Analogously, it contains rutile MO_2 bulk unitcells at compressed, optimized and decompressed DFT lattice parameters, as well as with displaced internal coordinates.

With a view on the intended surface structure determination, a final category of structures is spanned by different (1×1) terminations of all five rutile low-index facets, each time in a bulk-truncated geometry and in the DFT optimized geometry. Specifically, we include the 21 structures that result from systematically considering metal-rich, stoichiometric and O-rich terminations, as well as terminations with an additional peroxo (-OO) group for all facets. The exact geometries of all structures in the thus resulting initial training set for both RuO_2 and IrO_2 are provided in an online repository.[50]

Hyperparameter Selection: As outlined in the Methods section, training a GAP requires selecting a series of hyperparameters. Most prominently, these are the δ-weights controlling the relative contributions of 2B and MB terms in Eq. (1) and the regularization parameters σ_n in Eq. (2). Herein, we use separate parameters σ_E and σ_F for energies and forces, respectively. Additionally, GAP requires the definition of the number of sparse points M_{2B}, M_{MB}. There are also a number of hyperparameters related to the choice of representations and kernels. In particular, both 2B potential and SOAP use a cutoff radius ($r_{cut,2B}, r_{cut,SOAP}$) for atomic interactions and both use a Gaussian broadening to control the smoothness of the representation ($\sigma_{2B}, \sigma_{SOAP}$). Finally, SOAP uses a set of radial and angular basis functions to expand the atomic environment, the number of which is controlled by the parameters n_{max} and l_{max}.

The selection of these parameters is challenging in iterative training schemes. While it is possible to optimize the parameters on the bootstrapping set, it is unclear whether this choice is transferable to the larger training sets subsequently generated. Fortunately, reasonable heuristics and physical insight can be applied to mitigate this issue. For example, the weighting of 2B and MB contributions is estimated from the residual error of a pure two-body potential fit on the bootstrapping set. Here, it is important to note that these weights δ_{2B}, δ_{MB} are priors, which are multiplied with the regression coefficients in Eq. (1). This means that the actual contributions of the MB and 2B terms can deviate from these priors, if this allows minimizing the loss function (within the flexibility afforded by the regularization). Consequently, it is not necessary to redetermine the δ values every time the training set is increased.

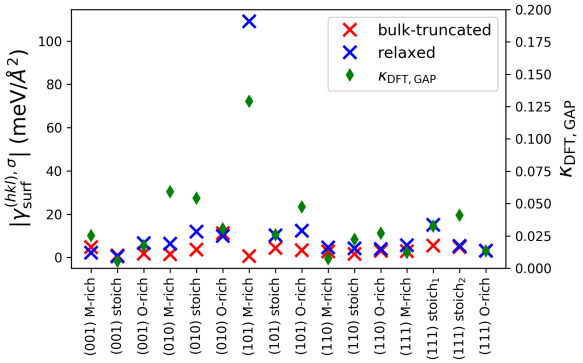

FIG. 1: Absolute difference of IrO_2 surface free energies $|\gamma_{surf}^{(hkl),\sigma}|$ computed by DFT and with the initial GAP V_0 for 16 different facets and (1×1) terminations contained in the bootstrapping training set. Shown is data for the bulk-truncated geometries (red crosses) and optimized geometries (blue crosses). In the latter case, the optimization is performed on the corresponding potential energy surface and the DFT and GAP structures compared are thus not necessarily the same. The shown kernel distance $\kappa_{DFT,GAP}$, cf. Eq. (5), provides a measure for this structural dissimilarity (green rhombuses). Analogous results for RuO_2 are shown in Fig. S8.

Similarly, the regularization parameters σ_E and σ_F are chosen to balance between over- and underfitting (see Fig. S6).

Meanwhile, the cutoff parameters $r_{cut,2B}$ and $r_{cut,SOAP}$ are related to the characteristic length scale of interatomic interactions in the material. These interactions result from a complex interplay of short-ranged chemical bonds, mid-ranged polarization and van-der-Waals effects, and long-range Coulomb interactions. It is therefore, not *a priori* possible to decide on an appropriate cutoff length. Fortunately, the locality of interactions in a given material can be estimated by analyzing the induced forces on a reference atom when atoms at increasing distances are displaced in DFT calculations.[13] A corresponding locality test for IrO_2 detailed in the SI motivates using cutoffs of $r_{cut,2B} = r_{cut,SOAP} = r_{cut} = 5$ Å in this study.

Given the cutoff, the remaining SOAP parameters (σ_{SOAP}, n_{max} and l_{max}) determine how the atomic environment within the cutoff radius is described. As a general rule of thumb, we choose the number of radial functions (n_{max}) to be twice the number of angular functions (l_{max}), as it has been shown that using larger radial than angular band limits generally leads to better accuracy for a given computational cost.[35] Herein, we find essentially converged performance on the bootstrapping set with n_{max}=8 and l_{max}=4 (see SI). The full set of hyperparameters used is compiled in Table I.

Assessment of Initial GAP V_0: As intended, the initial GAP V_0 trained with the bootstrapping set displays stable reference structures. The optimum O_2 dimer distance exactly matches the DFT value of 1.22 Å, and the optimum bulk MO_2 lattice

TABLE I: GAP hyperparameters employed in this work.

	r_{cut} [Å]	σ_{2B} [Å]	δ_{2B} [eV]	M_{2B}	σ_{SOAP} [Å]	n_{max}	l_{max}	δ_{MB} [eV]	M_{SOAP}	σ_{E} [eV]	σ_{F} [eV/Å]
IrO_2	5.0	1.0	0.362	25	0.6	8	4	0.100	2000	0.001	0.01
RuO_2	5.0	1.0	0.326	25	0.6	8	4	0.086	2000	0.001	0.01

parameters are within 0.5% of the corresponding DFT parameters. The O_2 binding energy and MO_2 bulk cohesive energies are reproduced within 16 meV/atom and 25 meV/atom, respectively.

Gratifyingly, this local stability also extends already to most of the (1×1) low-index surface structures contained in the bootstrapping set. Figure 1 compiles the absolute differences of surface free energies $|\gamma_{\mathrm{surf}}^{(\mathrm{hkl}),\sigma}|$ computed with DFT and the preliminary GAP V_0 for these surfaces. Shown is not only data for the (necessarily identical) bulk-truncated geometries, but also after optimizing the structures on the respective potential energy surface (PES). This means that starting from the bulk-truncated surface geometry, the GAP structure is optimized on the GAP PES, while the DFT structure is optimized on the DFT PES, here and later always fully relaxing the entire slab.[51] Figure 1 also compares the structural similarity of the two resulting minimum structures for each of the 16 IrO_2 surfaces as quantified by their kernel distance κ. With the notable exception of the (101) metal-rich termination, κ is smaller than 0.075 throughout, indicating a high similarity of the corresponding PES basins. We thus achieve already at this stage a highly satisfactory description of these PES parts of highest relevance for structure determination, as also evidenced by the consistently low error in the GAP surface free energies. Even the structurally and energetically much dissimilar GAP minimum structure for the (101) metal-rich termination does actually not reveal a major shortcoming of the initial GAP. Instead, it is in fact already a first success of the global structure determination to which we will return in more detail below.

Nevertheless and not surprisingly, the initial GAP is not perfect though. This is prominently reflected by a complete instability of the five peroxo terminated surfaces contained in the bootstrapping set. Upon GAP relaxation of the corresponding bulk-truncated geometries, the peroxo group always detaches to form an O_2 dimer. To analyze this problem and generally obtain insight into generated GAPs, we found an analysis of atom pair potentials (or atom binding energy curves) as shown in Fig. 2 to be a useful tool. This analysis is based on the number of local environments in the current training set that actually convey information of specific two-body distances between the atomic species. Contrasting this number as done in Fig. 2 with the predicted binding energy curves between two atomic species (here M-M, M-O, and O-O) readily discloses a possible lack of relevant information. Precisely in distance ranges for which current training structures do not provide data, these binding curves tend to exhibit non-physical behavior, e.g. numerous minima or a lacking repulsive wall at short distances. Assessing the two-body distances contained in potential new training structures

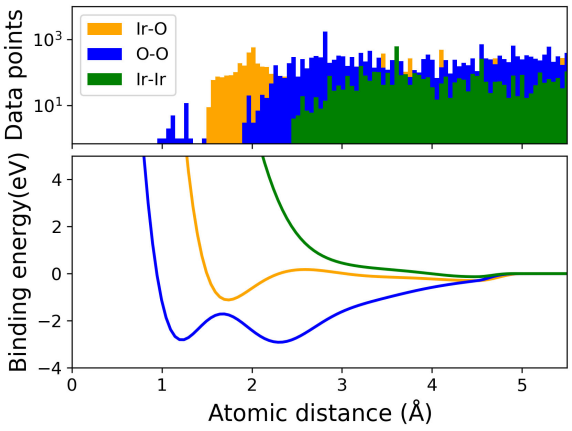

FIG. 2: Atom pair potential analysis for the initial GAP V_0. (Lower panel) GAP predicted binding energy as a function of distance between two Ir atoms, two O atoms and an Ir-O atom pair. (Upper panel) Number of local environments in the bootstrapping training set that provide corresponding two-body distances in their representation. Analog results for RuO_2 are shown in Fig. S9.

then shows whether they actually provide data on hitherto undersampled distance ranges. This provides a manual way to identify most meaningful new training structures, before the computationally demanding DFT calculations are actually initiated. In the present case, this type of analysis led us for instance to include the five peroxo terminations into the bootstrapping set in the first place, as they convey important information on shorter O-O distances. As apparent from Fig. 2, there is still a lack of relevant structural information at O-O distances around and above 1.5 Å though, which is precisely the range relevant for the surface peroxo groups. The O-O pair potential correspondingly shows a nonphysical form in this range, rationalizing why the peroxo groups decay into the more stable O_2 dimer within this initial GAP V_0. In contrast, the relevant range of Ir-O and Ir-Ir distances is sampled quite well by the structures in the bootstrapping set. Correspondingly, the Ir-O and Ir-Ir pair potentials predicted by the GAP V_0 potential also look reasonable. The Ir-O potential shows one clearly defined minimum around distances corresponding to equilibrium distances in bulk IrO_2. As the bootstrapping training set does not include Ir metal structures, the Ir-Ir pair potential instead is purely repulsive. This reflects the obvious

fact that the training structures generally tailor the GAP for the intended application, and least in its present form this initial GAP V_0 would not be transferable to e.g. address oxide reduction to the parent metal.

Iterative Refinement: While the atom pair potential analysis provides leads towards a manual addition of further training structures, we rather seek to establish a generic protocol that depends less on the chemical insight of the researcher. In a second stage of our training protocol we thus refine the initial GAP V_0 in an iterative process. To ensure a high data efficiency, this process is specifically tailored for the intended use for surface structure determination. This use case requires a sufficiently precise representation of the PES basins that act as funnels into the distinct local minima, while the remaining PES only needs to be known to the extent that it shall not contain barriers between basins that are insurmountable by typical global optimization and PES exploration techniques. To some extent, we thus trade versatility with data efficiency, and concentrate on exclusively identifying new metastable surface structures (PES minima) as additional training structures for the GAP potential. Obviously though, this concept is readily adapted to other use cases, notably e.g. by selectively including transition states into the training when aiming for kinetics.

This specific, basin-focused ansatz intrinsically blurs the lines between the iterative GAP training and the actual global geometry optimization, since identified "novel" training structures are themselves already the sought-after, new and dissimilar surface structures beyond the conventional terminations that were already included in the bootstrapping set. Here, we illustrate this concept by specifically exploring the chemical space of all low-index surface structures with (1×1) surface unit-cell periodicity. As detailed below, we reach a high data efficiency for this sub-space, identifying an intriguing, unknown class of surface structures termed complexions after having computed a minimum number of additional DFT structures. In future work, the final GAP trained this way could serve as starting point for the exploration of larger surface unit-cell reconstructions, then iteratively adding corresponding structures to the training set. An additional challenge at this stage will arise when such structures extend over surface unit-cells that are no longer tractable with direct DFT calculations and thus appropriate smaller models containing the same structural motifs need to be found for the training. One important aspect to this end could be the here pursued multi-task learning, i.e. training the GAP simultaneously for all five low-index facets. This creates a variety of structural motives already within the small (1×1) surface unit-cells that otherwise would potentially have to be learned in larger surface unit-cells when training the GAP only on a single facet.

For the present exploration of the chemical space of low-index (1×1) structures, we implement the iterative refinement process by executing the steps summarized in Fig. 3 at every refinement step s. Parallel SA runs based on the GAP V_{s-1}, which resulted from step $s-1$, are spawned for the 16 different surface types shown in Fig. 1. As the geometric details of the initial surface structure from which a SA is started are lost in the heating phase, we use these 16 different SAs primarily to sample the structural space of different chemical compositions and always start from the respective bulk-truncated terminations for simplicity. Note that our interest is here more in O-poor environments where the new complexions form, see below. This is why we do not further consider the highly O-rich peroxo terminations included in the bootstrapping set, but seek to obtain training data for short O-O distances otherwise.

After cool-down and optimization, we then arrive at 16 new GAP basin candidates $\mathrm{BC}_{\mathrm{GAP}}^{(hkl),\sigma}(s)$ in each refinement step s. Each candidate is compared to all previously identified basins $\{\mathrm{B}^{(hkl),\sigma}\}$ of the same Miller index (hkl) and termination σ using the kernel distance κ, cf. Eq. (5). Figure 4 shows the evolution of κ during six selected SA runs in the first refinement step $s=1$, where $\{\mathrm{B}^{(hkl),\sigma}\}$ consists for each (hkl,σ) only of the corresponding bulk-truncated and DFT-optimized surface structure contained in the initial bootstrapping set. In two of the shown SA runs (as well as in the other 10 not-shown ones) κ decreases back to essentially zero after cool-down and the subsequent geometry optimization, indicating that the candidate structure has collapsed back into the known basin from the bootstrapping set. In contrast, in four runs, finite values $\kappa > 0.075$ remain during cool-down and optimization. Visual inspection, cf. Fig. 4, reveals that in all four cases a new PES basin with a distinct structure has been found. Based on this experience in the first refinement step, we employ $\kappa_{\mathrm{crit}} = 0.075$ as a system-specific parameter for all later steps $s > 1$ and classify a GAP basin candidate as hitherto not known, if it exhibits a $\kappa > \kappa_{\mathrm{crit}}$ with respect to all previously assembled basins $\{\mathrm{B}^{(hkl),\sigma}\}$.

Every new GAP basin candidate is subsequently subjected to a DFT optimization to obtain DFT basin candidate $\mathrm{BC}_{\mathrm{DFT}}^{(hkl),\sigma}(s)$. If this does not lead to any significant structural changes with respect to $\mathrm{BC}_{\mathrm{GAP}}^{(hkl),\sigma}(s)$, here and henceforth indicated again by a similarity measure $\kappa < \kappa_{\mathrm{crit}}$, then there is no need to consider both similar structures in the GAP training and only the new DFT basin structure $\mathrm{BC}_{\mathrm{DFT}}^{(hkl),\sigma}(s)$ is added to the pool of known basins $\{\mathrm{B}\}$. If there is a significant structural difference and the DFT basin structure was not known, then both the GAP basin candidate $\mathrm{BC}_{\mathrm{GAP}}^{(hkl),\sigma}(s)$ and the DFT basin candidate $\mathrm{BC}_{\mathrm{DFT}}^{(hkl),\sigma}(s)$ are added to the pool. If instead there is a significant structural difference between $\mathrm{BC}_{\mathrm{GAP}}^{(hkl),\sigma}(s)$ and $\mathrm{BC}_{\mathrm{DFT}}^{(hkl),\sigma}(s)$, but $\mathrm{BC}_{\mathrm{DFT}}^{(hkl),\sigma}(s)$ was already known, then the current GAP potential V_s provides apparently only an insufficient representation of this known basin. Since the DFT basin is already contained in the pool of known basins, only the new GAP basin candidate $\mathrm{BC}_{\mathrm{GAP}}^{(hkl),\sigma}(s)$ is added in this case.

As shown in Fig. 3, this iterative process is repeated until no further new basin candidate is added to the pool in refinement step s. At this point, we declare the training protocol as converged and conclude that all relevant energetically low-lying PES minima in the sampled sub-space of (1×1) surface unit-cells have been found. Note that this situation arises only when no unknown basins are found *and* the last GAP refinement $V_{s-1} \to V_s$ has not led to any significant structural relaxation of previously found GAP basins. In the present application to the rutile oxides, this convergence is quickly reached in $s = 12$ iterations. The final pool of known basins

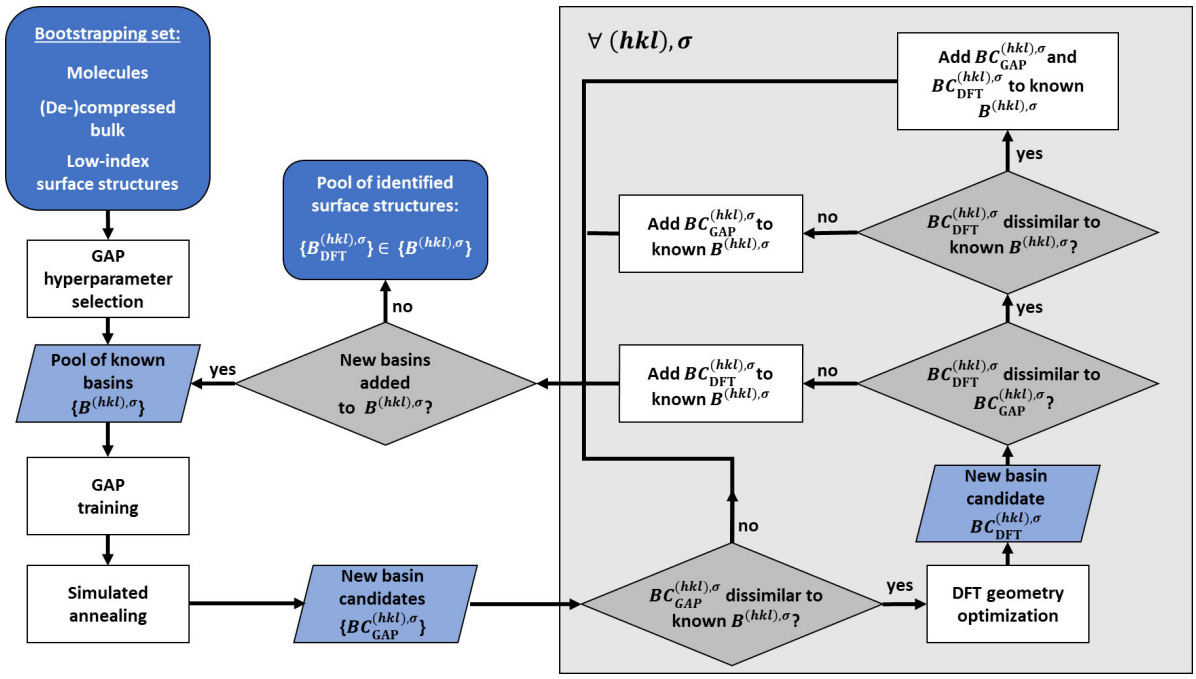

FIG. 3: Flowchart of the iterative GAP training protocol.

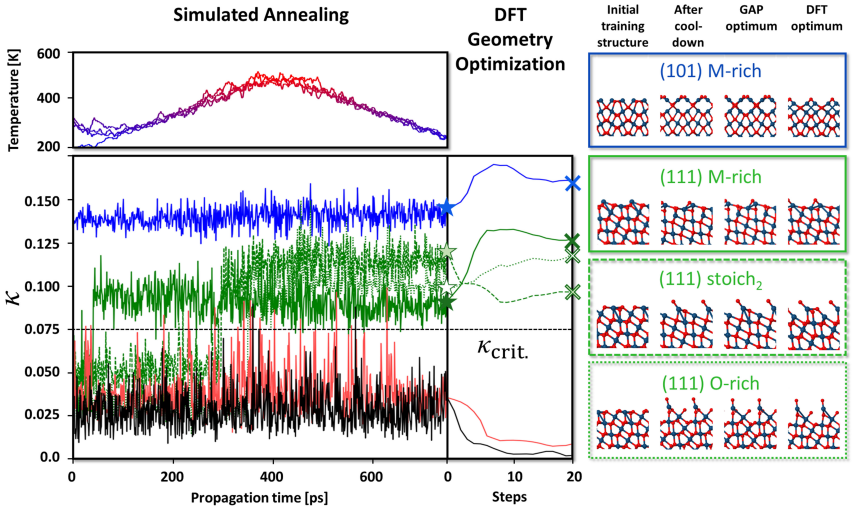

FIG. 4: (Left panel) Evolution of the kernel distance κ during 6 of the 16 SA runs of the first GAP refinement step $s = 1$ for IrO_2. κ generally measures the similarity of the SA structure to all previously found basins $\{B^{(hkl),\sigma}\}$ of same Miller index (hkl) and termination σ. In two cases ((010) O-rich, solid red line, (001) O-rich, solid black line), the SA does not lead to a new structure as reflected by the small κ value. In four cases, the SA identifies a new structure as reflected by a $\kappa > \kappa_{\mathrm{crit}} = 0.075$. (Right panel) Side views illustrating the identified new structures (Ir atoms drawn as larger blue spheres, O atoms as smaller red spheres). Shown for all four cases are the initial training structure, the structure obtained after cool-down and the structures obtained after the final GAP and DFT geometry optimization (see text). The κ values of these optimized geometries are additionally highlighted in the left panel as correspondingly colored stars (GAP PES minimum) and crosses (DFT PES minimum).

contains an additional 80 structures for IrO_2 and 63 structures for RuO_2 beyond the 32 surface structures already contained in the bootstrapping set. Of these, 53 (IrO_2) viz. 43 (RuO_2) correspond to DFT optimized geometries, with the remaining ones corresponding to GAP optimized geometries. All structures are again provided in an online repository.[50]

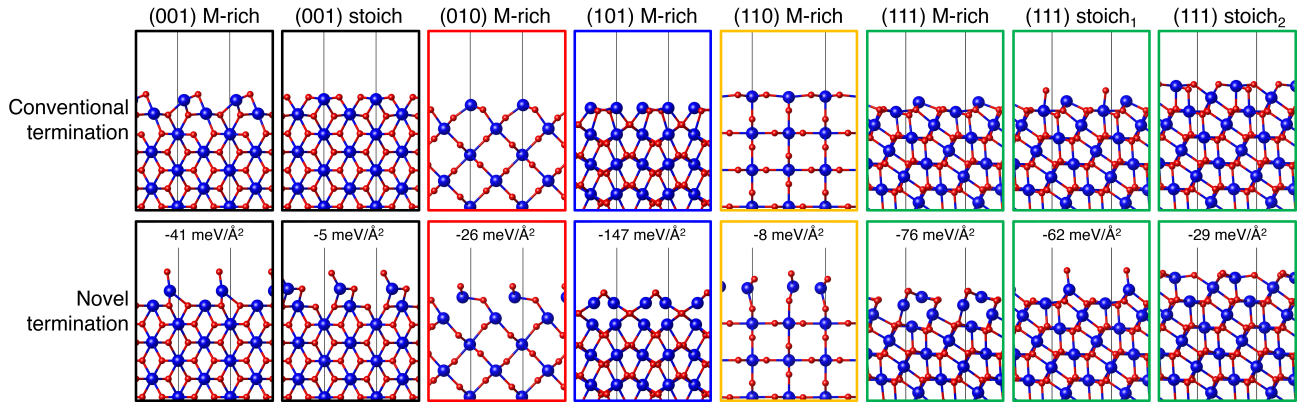

FIG. 5: Unconventional and energetically more stable (1×1) IrO_2 surface structures identified during the GAP training and surface exploration protocol. Upper row: Side view of the conventional $(hkl),\sigma$ termination resulting from truncating the bulk oxide-layering sequence and subsequent DFT geometry optimization. Lower row: Side view of the identified most stable structure, with the relative difference in surface free energy stated explicitly (see text for the (101) metal-rich termination). Ir atoms are drawn as larger blue spheres, O atoms as smaller red spheres. The color coding of the figure frames is consistent with that of the κ trajectories in Fig. 4. Analog results for RuO_2 are shown in Fig. S10.

Adding a GAP optimized geometry to the training set requires only a DFT single-point calculation. Compared to this, the DFT geometry optimization of a (1×1) surface structure required to add a DFT optimized geometry to the training set is computationally much more demanding. In this respect, the fact that for the exploration of the sub-space of all low-index (1×1) surface structures only 53 (IrO_2) viz. 43 (RuO_2) such optimizations are needed attests to the high data efficiency of our approach. While this does in fact not constitute any significant computational burden on modern supercomputing architectures, we nevertheless chose to further increase the computational efficiency of our approach by thresholding the costs for these DFT geometry optimizations. For this, any optimization is stopped, if relaxation is not achieved within the first 20 geometry steps. In that case, we simply employ the last geometry as a sufficient proxy for $\mathrm{BC}_{\mathrm{DFT}}^{(hkl),\sigma}(s)$ for the purpose of differentiating known and unknown basins. Further increases in efficiency could be reached by performing the SAs only for subsets of all surface orientations and terminations, e.g. selected on the basis of farthest point sampling of structural dissimilarity of all acquired basins at the time. Yet, all of this will only start to play a role when extending the global geometry optimization to larger surface unit-cells and will be the topic of future work in our group.

B. Novel Structures and Surface Phase Diagram

As mentioned above, the iterative refinement blends GAP training with the actual surface structure exploration, i.e. the basins accumulated in the final GAP training pool constitute at the same time the result of the SA-based global geometry optimization. It is worthwhile to emphasize the elegant efficiency of this approach: The extensive energy and force evaluations underlying the SA PES exploration are performed at the undemanding GAP level, while novel identified basins are immediately validated by computationally less demanding DFT geometry optimization as part of the training protocol. Every DFT basin contained in the final pool of GAP training structures is therefore already intrinsically validated at the first-principles level. Of course, not all of these metastable PES minima are physically really relevant. Many are likely energetically rather unfavorable and were only added to the training pool to pinpoint specific structural motives for the GAP.

Thermodynamically relevant is instead at best only the lowest-energy structure within each $(hkl),\sigma$ class, i.e. defined facet orientation and surface stoichiometry. In this respect, the resulting pool of structures is highly intriguing and underscores impressively the necessity of global geometry optimization for reliable surface structure determination. Even though the sub-space of structures with (1×1) surface unit-cells was initially only chosen for the methodological development of the training and exploration protocol, energetically lower-lying terminations are in fact identified for eight (IrO_2) and seven (RuO_2) of the 16 $(hkl),\sigma$ classes. In other words, even within the restricted structural possibilities of these small unit-cells, more stable alternatives to the conventionally considered simple truncations of the bulk oxide-layering sequence are for both oxides found in about half of the cases.

As detailed for IrO_2 in Fig. 5, these unconventional structures extend over metal-rich and stoichiometric surface compositions, and are in many cases energetically significantly more stable than their conventionally considered bulk-layered counterparts. Partly, the new structures are somewhat obvious and may thus potentially also have been tested as part of a human-devised set of trial candidate structures. This concerns notably open structures like those of the (001) metal-rich or (111) stoichiometric class, where terminal O atoms do not occupy the (relaxed) sites corresponding to the next

layer in the bulk-layering sequence, but instead to the second next one. However, especially for the (101) metal-rich and (111) metal-rich class, the novel structures with their concomitant strong energetic lowerings are quite counter-intuitive and had never been reported in literature before our preceding work[10]. Once understood, they are conceptually straightforward, too, though. They correspond to a reordering of the layering sequence, in which a terminal metal layer swaps its position with an oxygen layer and thereby achieves a higher O-coordination for its metal atoms.

For the (101) metal-rich termination, the concomitant stabilization is in fact so strong that the conventional termination is not even a local minimum on the DFT-PES anymore. It relaxes barrierlessly into the re-ordered structure, which is why we state the relative energy lowering in Fig. 5 with respect to the artificial bulk-truncated and unrelaxed conventional termination. For IrO_2, this conventional termination is spuriously (meta-)stabilized when only relaxing a finite number of outermost slab layers (and freezing innermost slab layers) as is typically done in DFT geometry optimization. As this was also done in the creation of the bootstrapping training set, this conventional (101) metal-rich termination is part of the IrO_2 set. As noted above, the entire slab is instead flexible in the GAP SA runs and subsequent DFT optimizations, and even the preliminary GAP V_0 then immediately led to this new structure – as reflected by the high kernel distance κ for this (101) metal-rich class in Fig. 1. In contrast, for RuO_2 the conventional termination is never meta-stable, even if only a few outermost layers are relaxed during the DFT geometry optimization, cf. Fig. S8.

Whether or not the identified, novel lower-energy structures play a role thermodynamically depends on the environment to which the oxide is exposed. Here, we specifically consider an oxygen atmosphere. Figure 6 correspondingly shows the surface phase diagram for IrO_2 and RuO_2 in the explored subspace of (1×1) surface structures as a function of the oxygen chemical potential of this surrounding gas phase. Within the *ab initio* thermodynamics approach[21,22] such a surface phase diagram is constructed by computing the surface free energy, $\gamma_{\text{surf}}^{(hkl),\sigma}(\Delta\mu_O)$ of Eq. (7), for each DFT-optimized basin and plotting for each $\Delta\mu_O$ only the lowest energy one for each of the five facets. In the specific case of the here explored (1×1) structures, the lines in the resulting surface phase diagram are easily read. A positive slope indicates the stability of a metal-rich termination in the corresponding range of oxygen chemical potentials, a horizontal line the stability of a stoichiometric termination, and a negative slope the stability of an O-rich termination. Any kink in the continuous line representing one facet orientation therefore reflects a change to a more stable termination with different stoichiometry.

As apparent from Fig. 6 quite some changes are induced by the novel structures as compared to the surface phase diagram when only considering the conventional bulk oxide-layered terminations.[10,33] Notably, this extends to O-poor conditions, where the novel metal-rich (101) structure results as by far most stable for both oxides. For IrO_2, this intriguing result (and first-principles prediction) has been validated by experimental work on crystals grown under corresponding O-poor conditions.[10] Detailed surface science characterization confirmed the dominance of the (101) facet and the specific geometry of this novel structure. Accompanying calculations showed that no further stability gains can be reached by a reordering of deeper layers. This places this novel structure close to so-called complexions as discussed for complex ceramic materials.[52] These complexions possess a thermodynamically determined equilibrium thickness on the order of nanometers, but are neither thin versions of a known 3D bulk phase nor a reconstructed surface layer. In this preceding work, a recomputation of this complexed (101) metal-rich termination for RuO_2 suggested that this novel structure should also be stabilized for this oxide. As seen in Fig. 6, we can now confirm this on the basis of the proper surface exploration per-

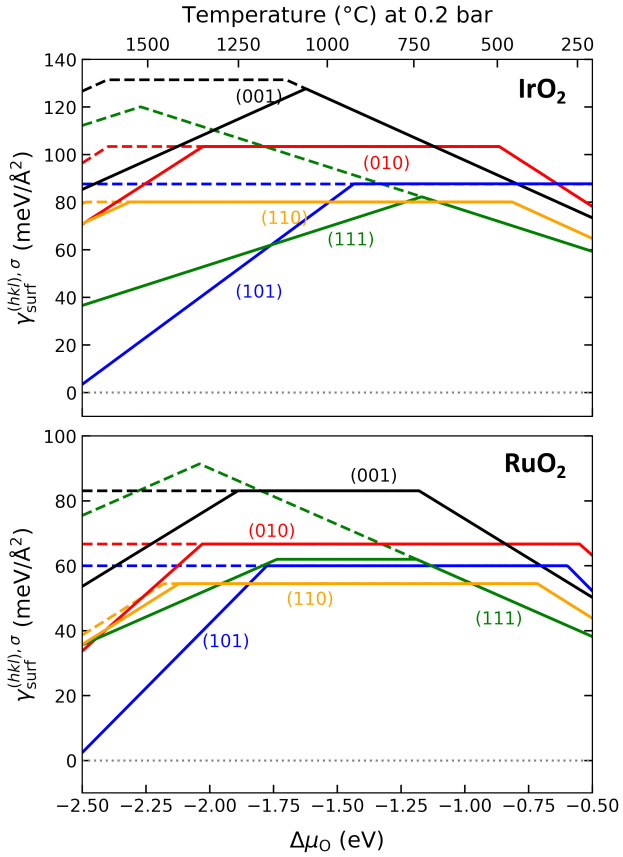

FIG. 6: DFT surface free energies $\gamma_{\text{surf}}^{(hkl),\sigma}$ of the five symmetry-inequivalent low-index facets of IrO_2 (top) and RuO_2 (bottom) in a pure oxygen atmosphere. In the top x axis, the dependence on the oxygen chemical potential $\Delta\mu_O$ is translated into a temperature scale at 0.2 bar pressure (the oxygen partial pressure in air). Shown is for each facet only the surface free energy of the most stable termination at each chemical potential. Each kink in the corresponding line indicates therefore the change to a different termination with different stoichiometry. The dashed lines indicate the surface free energies when only considering the conventional (relaxed) bulk oxide-layered terminations (see text).

formed for this material. At the same time, it is also for RuO_2 that literature already tells that the surface phase diagrams on the basis of the sub-space of (1×1) surface unit-cells can not yet be complete: The deactivation of this catalyst for CO oxidation had been assigned to the formation of a $c(2 \times 2)$ reconstruction of the (010) facet.[34] Extending the data-efficient GAP training and exploration protocol to such larger surface unit-cells forms correspondingly the natural next topic of our work.

IV. CONCLUSIONS AND OUTLOOK

We have presented a protocol for surface structure determination through a surrogate ML potential that achieves high efficiency with regard to the required first-principles calculations by mixing the potential training and surface exploration. In an iterative process, the employed GAP identifies novel structures through extensive SA-based sampling of the potential energy surface, and is refined by adding sufficiently dissimilar structures to its training pool. In its construction, this protocol is aimed for general usage. Here, we have illustrated it with the application to surface structure determination of low-index facets of rutile IrO_2 and RuO_2 within the sub-space of structures with (1×1) surface unit-cells. Intriguingly, already in this restricted space a number of non-intuitive low-energy structures are identified that would potentially have escaped the more traditional approach of testing a set of candidate structures devised by the researcher.

The obvious next step in developing an automatized workflow for surface structure determination in less restricted structural spaces would be to consider larger surface unit-cells, e.g. to address some known surface reconstruction. For tractable unit-cell sizes, the present protocol should in principle be readily applicable. For one, one would only face concomitantly larger computational costs for each required DFT training structure. More problematic is the larger range of different possible surface stoichiometries, as the actual surface composition is generally not known, even if the surface unit-cell is. For the here considered sub-space of (1×1) structures, this compositional range comprised metal-rich, stoichiometric and oxygen-rich compositions. Many more relative compositions would have to be considered for general $(m \times n)$ surface unit-cells in the present approach rooted on separate, canonical PES sampling. Ultimately, grand-canonical schemes could become appealing, but would have to be appropriately integrated into the GAP training. A final grand challenge arises in the context of completely unbiased surface structure determination extending over surface unit-cells of unknown size and shape. To the least, schemes will need to be developed that extract those local environments and geometric motives deemed important for the ML potential training into surface unit-cells that can still be accessed by first-principles calculations.

ACKNOWLEDGEMENTS

This research was supported by the Kopernikus/P2X programme (Cluster FC-A1) of the German Federal Ministry of Education and Research, the German Federal Environmental Foundation DBU, and the German Academic Exchange Service DAAD.

V. DATA AVAILABILITY STATEMENT

The data that support the findings of this study are openly available at https://doi.org/10.6084/m9.figshare.16610488.[50]

[1] A. P. Bartók, M. C. Payne, R. Kondor, and G. Csányi, Phys. Rev. Lett. **104**, 136403 (2010).
[2] J. Behler, J. Chem. Phys. **134**, 074106 (2011).
[3] M. Rupp, A. Tkatchenko, K.-R. Müller, and O. A. Von Lilienfeld, Phys. Rev. Lett. **108**, 058301 (2012).
[4] J. C. Snyder, M. Rupp, K. Hansen, K.-R. Müller, and K. Burke, Phys. Rev. Lett. **108**, 253002 (2012).
[5] K. Hansen, G. Montavon, F. Biegler, S. Fazli, M. Rupp, M. Scheffler, O. A. Von Lilienfeld, A. Tkatchenko, and K.-R. Müller, J. Chem. Theory Comput. **9**, 3404 (2013).
[6] F. Brockherde, L. Vogt, L. Li, M. E. Tuckerman, K. Burke, and K.-R. Müller, Nat. Commun. **8**, 1 (2017).
[7] O. A. Von Lilienfeld, Angew. Chem. Int. Ed. **57**, 4164 (2018).
[8] J. Schmidt, C. L. Benavides-Riveros, and M. A. L. Marques, J. Phys. Chem. Lett. **10**, 6425 (2019).
[9] M. Bogojeski, L. Vogt-Maranto, M. E. Tuckerman, K.-R. Müller, and K. Burke, Nat. Commun. **11**, 1 (2020).
[10] J. Timmermann, F. Kraushofer, N. Resch, P. Li, Y. Wang, Z. Mao, M. Riva, Y. Lee, C. Staacke, M. Schmid, C. Scheurer, G. S. Parkinson, U. Diebold, and K. Reuter, Phys. Rev. Lett. **125**, 206101 (2020).
[11] S. Stocker, G. Csányi, K. Reuter, and J. T. Margraf, Nat. Commun. **11**, 1 (2020).
[12] R. Jinnouchi, K. Miwa, F. Karsai, G. Kresse, and R. Asahi, J. Phys. Chem. Lett. **11**, 6946 (2020).
[13] V. L. Deringer and G. Csányi, Phys. Rev. B **95**, 094203 (2017).
[14] A. P. Bartók, J. Kermode, N. Bernstein, and G. Csányi, Phys. Rev. X **8**, 041048 (2018).
[15] D. Dragoni, T. D. Daff, G. Csányi, and N. Marzari, Phys. Rev. Mater. **2**, 013808 (2018).
[16] P. Rowe, V. L. Deringer, P. Gasparotto, G. Csányi, and A. Michaelides, J. Chem. Phys. **153**, 034702 (2020).
[17] C. Verdi, F. Karsai, P. Liu, R. Jinnouchi, and G. Kresse, Npj Comput. Mater. **7**, 1 (2021).
[18] E. L. Kolsbjerg, A. A. Peterson, and B. Hammer, Phys. Rev. B **97**, 195424 (2018).
[19] S. Kaappa, E. G. del Río, and K. W. Jacobsen, Phys. Rev. B **103**, 174114 (2021).
[20] M. K. Bisbo and B. Hammer, Phys. Rev. Lett. **124**, 086102 (2020).
[21] K. Reuter and M. Scheffler, Phys. Rev. B **65**, 035406 (2001).
[22] K. Reuter, Catal. Lett. **146**, 541 (2016).
[23] V. L. Deringer, M. A. Caro, and G. Csányi, Adv. Mater. **31**, 1902765 (2019).
[24] D. Opalka, C. Scheurer, and K. Reuter, ACS Catal. **9**, 4944 (2019).
[25] T. Reier, D. Teschner, T. Lunkenbein, A. Bergmann, S. Selve, R. Kraehnert, R. Schlögl, and P. Strasser, J. Electrochem. Soc. **161**, F876 (2014).
[26] P. Steegstra, M. Busch, I. Panas, and E. Ahlberg, J. Phys. Chem. C **117**, 20975 (2013).
[27] D. F. Abbott, D. Lebedev, K. Waltar, M. Povia, M. Nachtegaal, E. Fabbri, C. Copéret, and T. J. Schmidt, Chem. Mater. **28**, 6591 (2016).
[28] S. Cherevko, S. Geiger, O. Kasian, A. Mingers, and K. J. J. Mayrhofer, J. Electroanal. Chem. **774**, 102 (2016).
[29] E. Willinger, C. Massué, R. Schlögl, and M. G. Willinger, J. Am. Chem. Soc. **139**, 12093 (2017).

[30]P. Lettenmeier, J. Majchel, L. Wang, V. A. Saveleva, S. Zafeiratos, E. R. Savinova, J.-J. Gallet, F. Bournel, A. S. Gago, and K. A. Friedrich, Chem. Sci. **9**, 3570 (2018).
[31]P. Lettenmeier, L. Wang, U. Golla-Schindler, P. Gazdzicki, N. A. Cañas, M. Handl, R. Hiesgen, S. S. Hosseiny, A. S. Gago, and K. A. Friedrich, Angew. Chem. Int. Ed. **128**, 752 (2016).
[32]Q. Sun, K. Reuter, and M. Scheffler, Phys. Rev. B **67**, 205424 (2003).
[33]T. Wang, J. Jelic, D. Rosenthal, and K. Reuter, ChemCatChem **5**, 3398 (2013).
[34]J. Aßmann, D. Crihan, M. Knapp, E. Lundgren, E. Löffler, M. Muhler, V. Narkhede, H. Over, M. Schmid, A. P. Seitsonen, and P. Varga, Angew. Chem. Int. Ed. **44**, 917 (2005).
[35]V. L. Deringer, A. P. Bartók, N. Bernstein, D. M. Wilkins, M. Ceriotti, and G. Csányi, Chem. Rev. **121**, 10073 (2021).
[36]A. P. Bartók and G. Csányi, Int. J. Quantum Chem. **115**, 1051 (2015).
[37]J. S. De Almeida and R. Ahuja, Phys. Rev. B **73**, 165102 (2006).
[38]B. Cheng, R.-R. Griffiths, S. Wengert, C. Kunkel, T. Stenczel, B. Zhu, V. L. Deringer, N. Bernstein, J. T. Margraf, K. Reuter, and G. Csányi, Acc. Chem. Res. **53**, 1981 (2020).
[39]B. Hammer, L. B. Hansen, and J. K. Nørskov, Phys. Rev. B **59**, 7413 (1999).
[40]D. R. Hamann, Phys. Rev. B **88**, 085117 (2013).
[41]P. Giannozzi, S. Baroni, N. Bonini, M. Calandra, R. Car, C. Cavazzoni, D. Ceresoli, G. L. Chiarotti, M. Cococcioni, I. Dabo, A. D. Corso, S. de Gironcoli, S. F., G. Fratesi, R. Gebauer, U. Gerstmann, C. Gougoussis, A. Kokalj, M. Lazzeri, L. Martin-Samos, N. Marzari, F. Mauri, R. Mazzarello, S. Paolini, A. Pasquarello, L. Paulatto, C. Sbraccia, S. Scandolo, G. Sclauzero, A. P. Seitsonen, A. Smogunov, P. Umari, and R. M. Wentzcovitch, J. Phys. Condens. Matter **21**, 395502 (2009).
[42]C. G. Broyden, IMA J. Appl. Math. **6**, 222 (1970).
[43]D. Goldfarb, Math. Comput. **24**, 23 (1970).
[44]D. F. Shanno, Math. Comput. **24**, 647 (1970).
[45]K. K. Irikura, J. Phys. Chem. Ref. Data **36**, 389 (2007).
[46]S. Plimpton, J. Comput. Phys. **117**, 1 (1995).
[47]W. C. Swope, H. C. Andersen, P. H. Berens, and K. R. Wilson, J. Chem. Phys. **76**, 637 (1982).
[48]D. Music and B. Stelzer, Physics **1**, 290 (2019).
[49]H. J. C. Berendsen, J. P. M. van Postma, W. F. van Gunsteren, A. DiNola, and J. R. Haak, J. Chem. Phys. **81**, 3684 (1984).
[50]J. Timmermann and Y. Lee, IrO_2/RuO_2 Training Set and Complexions, 2021, DOI: 10.6084/m9.figshare.16610488.
[51]Since the GAP bulk lattice constant is not necessarily identical to the DFT one, the more common approach to constrain a certain fraction of innermost layers to bulk-like positions upon surface relaxation could impose artificial strain or require a delicate renormalization of atomic positions whenever a new training structure identified by the protocol is subjected to DFT computation.
[52]J. Luo, Energy Storage Mater. **21**, 50 (2019).

B Coefficients of full GPR

We here consider an unknown k-dimensional function $y(\mathbf{x})$ and N input-observation pairs collected in a training set $D_{k\text{-d}} = \{\mathbf{x}_n : y_n\}_{n=1}^{N}$. To solve for the coefficients of a *full* GPR model with a uniform weight σ_u we substitute $\tilde{y}(\mathbf{x}_n)$ and reformulate eq. (4.4) in matrix notation,

$$l = (\mathbf{y} - \mathbf{K}\mathbf{c})^\top (\mathbf{y} - \mathbf{K}\mathbf{c}) + \Sigma_\text{u} \mathbf{c}^\top \mathbf{K}\mathbf{c} \tag{B.1}$$

where $\mathbf{y} = (y_1, ...y_N)^\top$ contains all observations y_n, the matrix elements of $\mathbf{K}$ are defined as $\mathbf{K}_{n,n'} = k(\mathbf{x}_n, \mathbf{x}_{n'})$ and $\Sigma_\text{u} = \sigma_\text{u} \mathbb{1}$ is a diagonal matrix. For the more general loss function with individual weights i.e. eq. (4.3) the elements of the diagonal matrix Σ are defined as $\Sigma_{n,n'} = \delta_{n,n'} \sigma_{n,n'}$.

To minimize the loss function it is differentiated w.r.t. to all coefficients

$$\boldsymbol{\nabla} l = 0 \tag{B.2}$$

which subsequently yields an analytic expression for the optimal set of coefficients $\mathbf{c}$

$$\mathbf{c} = (\mathbf{K} + \Sigma)^{-1} \mathbf{y} \quad , \tag{B.3}$$

and finally for the prediction function

$$\tilde{y}(\mathbf{x}) = \mathbf{c}^\top \mathbf{k}_\mathbf{x} \tag{B.4}$$

where the kernel vector $\mathbf{k}_\mathbf{x} = (k(\mathbf{x}, \mathbf{x}_0), ..., k(\mathbf{x}, \mathbf{x}_N))^\top$ contains the similarity measure of the input $\mathbf{x}$ and all training points $\mathbf{x}_n$ in $D_{k\text{-d}}$.

For a *sparse* GPR model the formalism is slightly more complicated and explained in full detail in [1]. Effectively, sparsification reduces vector and matrix dimension in eq. (B.3) and eq. (B.4). Yet keeping in mind that the full set of observation ($\mathbf{y}$) is still used to train the *sparse* GAP.

C Sparsification

A mayor drawback of a *full* GPR potential is its poor scalability w.r.t. to the size of the training set as the computational costs of both, training and prediction/evaluation, scales with the data size ($\mathcal{O}(N^3)$ and $\mathcal{O}(N)$, respectively). This scaling makes especially MD simulations requiring an excessive amount of evaluations based on *full* GPR potentials already impractical for larger molecules/proteins let alone a set of surface structures. Moreover, a *non-sparse* GPR potential precisely mapping basis function and observation of a given system is limited to exactly that specific system and can not be applied to any other system of different size or composition. These two factors prevent the application of full GPR potentials in most chemical simulations, i.a. in this thesis.[1]

To circumvent both, the GAP framework constitutes a *sparse* GPR model in which the potential is based on a limited number of M basis functions (sparse points) with $M \ll N$. Note here that even with *sparsification* in the GAP model all N training points are used in the loss function eq. (4.4) to determine the coefficients.

Obviously, we have to make sure that this set of basis function provides a sufficiently accurate description of the input space spanned by the N training points. For low-dimensional input like in the tutorial example of section 4.1 or in case of the two-body representation discussed in section 4.2, a uniform grid within a certain range/cutoff is sufficient. For a high-dimensional input e.g. the SOAP representation discussed in section 4.2 though, a uniform grid is massively inefficient as the data points are usually distributed very irregularly. Within the GAP model the leverage-score CUR algorithm[6] is applied, which can be seen as a restricted principle components analysis ensuring that the selected points (basis functions) are indeed real training points (a feature not strictly required by the *sparse* GPR model). Furthermore, in the GAP implementation the number of basis functions for the SOAP representation is strictly limited by the number atoms N_{at}, respectively atomic environments (separately counted for each element) $M \leq N_{\text{at}}$. This has not to be mingled with the number of actual training points that usually include atomic energies *and* forces i.e. $N = N_{\text{at}} + N_{\text{f}}$. As a consequence, a SOAP-based GAP model always represents a *sparsified* GPR potential, even if the maximum possible number of basis functions ($M_{\text{max}} = N_{\text{at}}$) is applied.

[1] Despite these two drawbacks, full GPR models have been successfully applied in global optimization applying a computational less demanding random structure search[2, 3] and hybrid ML/DFT MD simulation[4, 5]. One outstanding advantage of this approach is the fact that a full GPR provides not only the prediction but also the related uncertainty i.e. the expected error. This allows for a direct estimation on how trustworthy a prediction is and whether or not a re-evaluation of the respective input (e.g. configuration) via the underlying *ab initio* method is necessary.

References

[1] V. L. Deringer, A. P. Bartók, N. Bernstein, D. M. Wilkins, M. Ceriotti, and G. Csányi, Chem. Rev. **121**, 10073 (2021) (cit. on p. 83).

[2] M. K. Bisbo and B. Hammer, Phys. Rev. Lett. **124**, 086102 (2020) (cit. on p. 85).

[3] S. Kaappa, E. G. del Rıo, and K. W. Jacobsen, Phys. Rev. B **103**, 174114 (2021) (cit. on p. 85).

[4] J. Vandermause, S. B. Torrisi, S. Batzner, Y. Xie, L. Sun, A. M. Kolpak, and B. Kozinsky, Npj Comput. Mater. **6**, 20 (2020) (cit. on p. 85).

[5] Y. Xie, J. Vandermause, L. Sun, A. Cepellotti, and B. Kozinsky, Npj Comput. Mater. **7**, 40 (2021) (cit. on p. 85).

[6] M. W. Mahoney and P. Drineas, Proc. Natl. Acad. Sci. **106**, 697 (2009) (cit. on p. 85).